UNIVERSITY OF CALIFORNIA
RIVERSIDE

Bio-Assembly of Bactericidal Inorganic Nanostructures Using M13 Bacteriophage Filaments, Rods and Spheroids

A Dissertation submitted in partial satisfaction
of the requirements for the degree of

Doctor of Philosophy

in

Materials Science and Engineering

by

Tam-Triet Ngo-Duc

March 2019

Dissertation Committee:

Dr. Elaine D. Haberer, Chairperson
Dr. Dimitrios Morikis
Dr. Ruoxue Yan

The Dissertation of Tam-Triet Ngo-Duc is approved:

_____

_____

_____

Committee Chairperson

University of California, Riverside

Acknowledgements

Over these past years in graduate school, the person I wish to thank first and foremost is my advisor, Dr. Elaine D. Haberer. I am very thank to her for the opportunity to work in her lab. Through her, I learned to systematically go through my experiments, critically think through my data, pick up the important nuggets of information, and develop further experiments based on my data. She taught me organizational, presentation, writing skills. It was in the lab that I learned how to apply the knowledge in materials science I gained and turn it into something more than sum of its parts. It was with all of her help and support that I've come so far. As a result, my skills as a scientist, a presenter and a researcher have all been thanks to her guidance. Words cannot express my gratitude for all she has done for me.

I would like to thank Joshua Plank for being a great friend and colleague for these past few years. Your help in the lab was invaluable and the research discussions we've had were most enlightening. Those sleepless nights in the lab, trying to figure out how to make an experiment work (especially with those spheroids), were some of the most fun times I had in the lab. I believe I still owe him a cup of hot chocolate. I would also like to thank Joseph Cheeney, who was my classmate, labmate and is most of all, my friend. While we didn't get a chance to directly work together in lab, he was most supporting and helpful.

To my labmates and friends in Haberer group, Dr. Mohammed Shahriar Zaman, Dr. Chung-Hee Moon, thank you for teaching me the ins and outs of the lab and for

helping me whenever I needed the advice. To Zaira Alibay and Stephen Hsieh, I would like to give my thanks for the countless discussions that delved deep into research. I would like to give special thanks to Zaira Alibay for helping me above and beyond with the bactericidal project. I will forever be thankful for the time you spent very early in the morning and late at night with the experiments.

I would like to give thanks to Dr. Dimitrios Morikis and Reed E. S. Harrison for the help in protein modeling. I would also like to give thanks to Gongde Chen and Dr. Haizhou Liu for kindly giving help with the ICP-MS.

I also thank the centers and facilities at UCR. Dr. Krassimir N. Bohzilov, Mathias Rommelfanger, and Michael Pidgeon were of the most help with the TEM at the Central Facility for Advanced Microscopy Microanalysis. Dr. Dan Borchardt and Prisciliano Saavedra at the Analytical Chemistry Instrumentation Facility provided training and support for the circular dichroism spectrophotometer and Horiba Labram/AIST-NT AFM.

The time I spent at UCR would not have been the same if it wasn't for all my friends and colleagues. I wish to extend my thanks to my mom and dad for all the love and support they gave me over the years. This journey has been most worthwhile and I will miss everyone here.

ABSTRACT OF THE DISSERTATION

Bio-Assembly of Bactericidal Inorganic Nanostructures Using M13 Bacteriophage Filaments, Rods and Spheroids

by

Tam-Triet Ngo-Duc

Doctor of Philosophy, Graduate Program in Materials Science and Engineering
University of California, Riverside, March 2019
Dr. Elaine D. Haberer, Chairperson

In recent years, the bacteriophage has been used as a versatile template to create inorganic nanomaterials and as a potential bactericidal agent to fight multidrug resistant bacteria. The M13 bacteriophage is a viable platform for bactericidal materials with an innate ability to target bacteria. The phage itself is a micron long, filamentous biological molecule. Extensive research has shown that this phage can be genetically modified to bind and biomineralize various inorganic nanostructures. Furthermore, unlike other viruses, the M13 bacteriophage has been shown to drastically change shape and aspect

ratio upon contact with chloroform, morphing from its filamentous form to either rods 100s of nanometers long or sub 100 nm spheroids. These different geometries could provide an excellent platform to deliver bactericidal materials due to their compactness.

In this study, we investigated the M13 bacteriophage as a template for bactericidal ZnO and gold nanoparticles and as a *E. coli* targeting platform. A filamentous genetically modified M13 bacteriophage, with the DRQVDATA peptide insert, was shown to have synthesize amorphous ZnO nanoparticles. Due to the low particle count and the phage agglomerates, the ZnO was found to be unsuitable for bactericidal purposes. No further investigation into the phage geometry was performed. A different avenue was explored with gold templated phage. To create a suitable gold platform, a gold-binding phage morphology was tailored to maximize contact of gold nanoparticles to the *E. coli* membrane. The binding and biomineralization properties of the transformed was examined and it was found that the templates retained its binding and mineralization properties. Furthermore, the gold mineralized on the spheroids differed from the gold grown on the filaments, where spike-like structures extended outward while isotropic particles grew on the latter.

These gold/phage platforms were then studied for their targeting and photothermal bactericidal properties. It was found that the Au/template was able to target the *E. coli* and via the photothermal effect, kill off more than 63% of the bacteria under 532 nm irradiation. These Au/templates were shown to be effective photothermal bactericide and could be further expanded to target other bacteria and to be used in near infrared wavelengths.

Table of Contents

List of Tables

Chapter 3

Chapter 4

List of Figures

Chapter 1

Chapter 2

Chapter 3

Chapter 4

Chapter 5

Chapter 1. Introduction

1.1 Motivation

Multidrug resistant bacteria have become a major health concern in recent years. Since the discovery of penicillin, antibiotics have been used in a plethora of areas including human therapy, farming, and aquaculture. This has led to pathogens becoming more and more resistant to currently available antibiotics and chemotherapeutic agents through genetic mutations[1–3]. This has been in part due to the overuse and misuse of antibiotics[1–4]. A well-known case is with the methicillin-resistant *Staphylococcus aureus* (MRSA). This bacteria has not only become resistant to the antibiotic methicillin but has also developed a resistance to a variety of antibiotics and disinfectants. As a result, new treatment methods are required to deal with this increasingly dangerous health issue. There have been developments in alternative treatments against multidrug resistant bacteria, including bactericidal nanoparticles, photothermal and phage therapy[1–3,5,6]. Photothermal therapy uses plasmonic nanoparticles which absorb light and heat a localized area to destroy the pathogens. These materials generally require the addition of antibodies to target specific pathogens. Phage therapy uses bacteriophage to treat bacterial infections. These bacteriophages are very specific, targeting only its host and have been shown to be effective at destroying the bacteria via lysing.

Over the past ten years, biotemplating using genetically modified viruses as scaffolds has been used to create nanostructures of various shapes and compositions. By

taking advantage of the innate ability of the virus to target bacteria and the ability to synthesize materials on the virus, it is possible to use the virus as a bactericidal agent. In this dissertation, the M13 bacteriophage was used as a template to synthesize and bind both gold, a photothermal bactericidal material, and bactericidal ZnO. Furthermore, the phage was morphologically modified to enhance the interaction area of the bactericidal material to the surface of the pathogen. Bactericidal experiments were then conducted using gold/transformed phage.

1.2 M13 Virus

The M13 bacteriophage is a filamentous virus of the genus *Inovirus*, belonging to the Ff class. These viruses specifically infect *Escherichia coli* and replicate in a non-lytic manner. The M13 bacteriophage interacts with the *E. coli* by targeting the F-pilus as the class name indicates. The M13 bacteriophage itself is about a micron long with a diameter of around 6 nm. It has a mass of 16.3 MDa, of which 87% is derived from proteins. A single stranded DNA is situated at its core, which is enclosed by both major and minor coat proteins. This capsid is primarily composed of 2700 copies of the pVIII major coat protein, arranged cylindrically in a right-handed α-helix with five-fold rotational symmetry and a two-fold screw axis.[7]. This protein is composed of 50 amino acids in an α-helix. Three to five copies of the pIII and pVI minor coat proteins are located at the proximal or infectious end of the phage. At the other end, the phage is capped with five pVII and pIX minor coat proteins. Ff bacteriophage libraries have been

used to discover numerous fusion peptides that selectively bind and template materials of technological consequence.[8–13]

The pIII is composed of three different domains: the N1, N2 and CT. Both the N1 and N2 take part in the infection process of the M13 bacteriophage. The infection process is initiated when the N2 domain of the pIII comes into contact and binds with the tip of the F-pilus [14,15]. Following this, the F-pilus retracts, bringing the phage to the *E. coli* membrane to infect it. Binding to the F-pilus also makes the pIII protein undergo a conformational change in order for the N1 domain to interact with the ToIA binding site and trigger the infection process [16].

The M13 bacteriophage has a property that is uncommon in viruses: the ability to radically modify its geometry. The structure of most viruses is largely constrained, allowing only modest dimensional or volumetric changes. For example, in response to changes in pH or salt concentration, a mere 10% increase in diameter of the cowpea chlorotic mottle virus can be attained and the capsid remains icosahedral.[17] As such, if a substantially different size or shape template is required for a specific application, a virus with corresponding architecture must be selected and appropriately modified with fusion peptides. Notably, a few plant viruses have exhibited more substantial shape conversion. When exposed to heat, the tobacco mosaic virus (TMV), is reduced from a 300 nm rod to a 170 nm sphere[18,19], and the potato virus X (PVX) shrinks from a 515 nm rod to a 48 nm sphere.[20] TMV transformation has been exploited for biomedical applications such as bio-compatible nanoparticles[21] and magnetic resonance imaging (MRI) contrast reagents.[22]

A more extreme case of viral shape transformation is displayed by the Ff class of bacteriophage, including f1, fd, and M13. Contact with a water/chloroform interface can cause Ff viruses to contract from 3- to 20-fold producing rod-shaped intermediate forms (i-forms) 100s of nanometers in length and hollow spheroids (s-forms) 10s of nanometers in diameter, depending on conditions. Although the precise mechanism is unknown[23,24], chloroform is thought to alter the hydrophobic protein-protein interactions of the major coat proteins. As such, pVIII proteins slide relative to one another causing long range conformational changes to the virus.[25–27] This chloroform-triggered transformation was initially studied in the early 1980s in the M13 by Griffith and colleagues and was thought to mimic the *E. coli* host infection process.[23,24]. To the best of the author's knowledge, the availability of the pIII post transformation has only been demonstrated with the i-forms and not the s-forms[28].

1.3 Virus Biomineralization

The fast pace of nanotechnology development has boosted demand for versatile manufacturing techniques capable of arranging molecular and nanoscale objects with nanometer precision. For millennia, nature has been assembling complex, highly-organized nanostructures. Among these are viral capsids. These robust, monodisperse, bio-based nanoparticles are exceptional scaffolds for nanomaterial assembly. Biomineralization using viruses has been heavily studied over the past years. Viruses exist in a multitude of shapes and sizes from icosahedrons to high-aspect-ratio filaments and from tens to hundreds of nanometers in dimension, thus providing an array of

template geometries.[29,30] Moreover, binding sites for specific materials, often referred to as fusion peptides, can be integrated into viral structural proteins. The locations, quantities, and functionalities of fusion peptides are encoded within the viral genetic material, making templates highly programmable.[29] Equally as important for nanomanufacturing, the mass production of viruses is not only possible, but environmentally-friendly and cost effective.[30] Viral templates have formed a variety of materials and nanoarchitectures[13,31–40], spanning metal-semiconductor core-shell structures to perovskite nanowires and have found application in battery electrodes[41,42], supercapacitors[43], sensors[44,45], biomedical tools[46,47], photocatalytic materials[31], and photovoltaics.[48]

The M13 bacteriophage specifically has been shown to be an excellent scaffold for a plethora of materials. The addition of peptides to the pVIII via genetic modification has allowed for materials to be bound and to be synthesized on those proteins. For example, gold-binding motifs displayed on the M13 and fd bacteriophage have been used to assemble or manufacture a variety of gold morphologies including nanoparticles, nanochains, and nanocubes for devices such as chemiresistive and surface-enhanced Raman scattering (SERS) sensors, as well as biofuel cells.[44,49–54] Huang et al. showed that the pVIII modified to express a hydroxyl rich peptide, VSGSSDPS, allowed for the formation of gold nanowires composed of either gold nanoparticles or a continuous with the phage as a scaffold[53]. These hydroxyl group are well known to have an affinity for gold lattice. This biomineralization is not limited to metals but extends to semiconductors as well as ceramics. $Cu_{1.8}S$ and PZT have been synthesized via electrostatic interactions

with glutamic acid rich peptide insert in the pVIII protein of the M13 bacteriophage[55,56]. The M13 bacteriophage has also been known to be used as a scaffold for Fe_3O_4, TiO_2, ZnS amongst other materials[12,57,58], hence showing its versatility as a platform. However, no studies up to this point have demonstrated the ability to bind or grow materials on a transformed phage.

1.4 Bactericidal Nanomaterials and Photothermal Treatment

As previously stated, multidrug bacteria have become a major healthcare issue. With more and more bacteria becoming resistant to current antibiotic treatment, the need for an alternative solution is increasingly in demand. Nanomaterials may provide such a solution. Research has currently showed different types of nanoparticles have antibacterial properties. Metals such zinc, copper and silver are well known to be bactericidal in their bulk form while materials such as iron oxide act as a bactericide only as nanoparticles[4]. The bactericidal mechanism is dependent on the composition of the nanoparticles. The bactericidal mechanism of silver, for example, causes cell death by disrupting functions of the cell membrane, reacting with the DNA and releasing silver ions, which interacts with thiol groups in enzymes, inactivating them.[1,59,60] Iron oxide nanoparticles have antibacterial properties by being the source of reactive oxygen species.[1,61] These radicals damage the bacteria's proteins and DNA.

Zinc oxide is a wide band gap semiconductor (3.37 eV) with the wurtzite crystal structure being the most prominent. The material has been studied for a variety of applications ranging from dye sensitized solar cells[62] to piezoelectric generators.[63] Zinc

oxide has also been studied as a bactericidal agent and research have yielded some promising results. Previous studies have shown that ZnO nanoparticles ranging from 8 to 60 nm are effective against a variety of bacteria, including *E. coli, S. aureus, and Bacillus subtilis.*[4] Compared to micron size ZnO particles, ZnO nanoparticles are significantly more effective. In Jiang et al, these micron size particles (1448 nm) have been observed to kill 100%, 75% and 50% of *B. subtilis*, *E. coli* and *P. fluorescens*. 20 nm ZnO nanoparticles killed 100% of all the aforementioned species. Padmavathy et al showed 12 nm ZnO nanoparticles killing 90% of *E. coli*[64] The bactericidal mechanism has been proposed to be two folds: zinc oxide disrupts the cell membrane causing cytoplasmic leakage and zinc oxide nanoparticle release zinc ions, which in turn generates reactive oxygen species (ROS) such as hydrogen peroxide and hydroxyl radicals. These radicals are toxic to bacteria by damaging the lipids, DNA and proteins, interfering with mitochondria functions and inhibiting cellular metabolism. This in turn leads to cell growth inhibition and death. Surface defects plays a major role in the formation of these ROS: Prasanna et al demonstrated that surface defects, more specifically singly ionized oxygen vacancy promotes the formation of superoxide, which reacts to form other ROS, including peroxides and hydroxyl radicals[65]. This was further confirmed by Perelshtein et al.[66]

Photothermal therapy on the other hand uses plasmonic nanoparticles to destroy the pathogens. As the name implies, these nanoparticles absorb light and the energy is transferred into heat via plasmon resonance. Gold nanoparticles are a good material for photothermal therapy. These nanoparticles have been shown to absorb strongly in both

the visible and NIR spectrum depending on the size and geometry.[67] This is thanks to surface plasmon resonance where coherent oscillations of the electrons in the gold conduction band when they resonate with the exposed frequency of light. This frequency is dependent on several factors: size, geometry and the dielectric constant of the medium around the nanoparticles. These factors allow us to tune the gold nanoparticles to a desired light wavelength to which the photothermal treatment will perform with. Size-wise, the larger the gold nanoparticle becomes, the more redshifted the absorption spectrum. Agglomeration of these gold nanoparticles also redshift the absorption spectrum due to coupling between the nanoparticles[68]. Geometry not only causes a major redshift but also can also splits the adsorption into two different peaks. This is most noticeable with gold nanorods.[69] The electrons oscillating along the length of the rods (longitudinal oscillations) show a strong absorption band in the NIR spectrum while the transverse oscillations create a weaker absorption band in the visible spectrum. The absorption wavelength of these gold nanorods can be tuned by changing the aspect ratio of the gold nanorods[70]. Gold nanoshells display a major redshift in the infrared with the tunability being dependent on the overall size of the shell and the thickness of the gold[71,72].

The photothermal effect comes from the electron gas heating up from the photoexcitation of the gold nanoparticles. The heated electron gas then transfers heat to the gold nanoparticle lattice in a very short timeframe of 1 ps. The nanoparticle lattice cools by exchanging this energy into the surrounding of the nanoparticle via phonon-phonon interactions. This process occurs over a period of 100 ps[70]. This energy

conversion heats up the nanoparticle surrounding in a very localized manner, increasing the surrounding temperatures in the tens of degrees at low laser excitation powers (100 nJ). The combination of absorption wavelength tuning and the photothermal effect allows gold to be an effective photothermal bactericide.

One of the most important requirements for the gold nanoparticles to be an effective bactericide is that the nanoparticles must be able to target the bacteria. Currently, active targeting of pathogens is done via the conjugation of antibodies to the nanoparticles. Photothermal bactericides using gold nanoparticles have been shown to be effective to varying degrees using both visible and NIR wavelengths[73–76]. Norman et al. demonstrated the bactericidal properties of gold nanorods against *Pseudomonas aeruginosa*[74]. These gold nanorods were able to target the pathogen by functionalizing the nanorods with an IgG anti-PA3 primary antibody. After exposing the sample to 50 mW 785 nm laser irradiation, the cell viability decreased to 25%. Without laser, 80% of cells remained viable[74]. Millenbaugh et al. had functionalized gold nanoparticles target *S. aureus* and the bacteria were exposed to 532 nm laser at fluence ranging from 1 to 5 J/cm^2 [77]. This resulted in 58% of viable *S. aureus*. In order to achieve over 90% kill rates, most studies have required the addition of antibiotics and silver.[78–83] The use of antibodies as a means to target bacteria does have some major drawbacks. Antibodies are prone to degradation, modification via oxidation and reduction and denaturation. Since the synthesis of antibodies via simple microbial hosts has yet to achieved, they have to be synthesized by using mammalian cell lines. This process is both convoluted and expensive[84].

1.5 Scope of Work

The work done in this dissertation evaluates the M13 bacteriophage as a template to synthesize bactericidal materials ZnO and gold, the binding and synthesis properties of the transformed gold-binding phage and the targeting and photothermal bactericidal properties of the Au/templates.

In chapter 2, we investigated the mineralization properties of a ZnO-binding phage. Using a previously selected ZnO binding-peptide insert via combinatorial phage display, the modified phage was used to biomineralize ZnO nanoparticles on the pVIII protein. It was found that the phage was only able to synthesize randomly dispersed amorphous ZnO nanoparticles.

In chapter 3, we looked into the transformation and optimization of a gold-binding spheroidal form of a modified gold binding bacteriophage. Here, we developed the spheroidal transformation process of the gold-binding phage using agarose gel electrophoresis and transmission electron microscopy to characterize the spheroids. To further refine and optimize the transformation, design of experiments were set up to attain repeatable spheroids of similar size. The spheroids were further characterized using circular dichroism and UV-Vis spectroscopy. We were able to create spheroids that were 59 ± 16 nm in diameter.

In the following chapter, we showed the gold binding and mineralization properties of the gold-binding M13 bacteriophage. We discovered that the pVIII coat protein retained its gold binding properties. In terms of mineralization, the spheroids

provided a template to form gold nanostructures. Major differences in gold morphology were seen between the spheroids and the filaments. Further study showed that the spheroids had a higher affinity to gold, which may attributed to the higher packing of pVIII major coat protein on the spheroids.

In Chapter 5, we demonstrated the targeting and bactericidal properties of Au/templates on *E. coli*. Here, we showed that the pIII of spheroids and i-forms retained their F-pilus binding properties. Furthermore, the gold nanoparticles decorating both i-forms and s-forms did not interfere with the pIII. We demonstrated that the F-pilus was able to retract and bring the Au/templates to the surface of the *E. coli*. Finally, we showed that the Au/templates worked as bactericide and the killing rate was comparable to those found in the literature.

In this dissertation, the M13 bacteriophage was demonstrated to be able to synthesize amorphous ZnO nanoparticles, spheroidal form of the phage was able to form gold nanostructures and these structures could be used as a photothermal bactericidal agent (Figure 1-1). Future work could be done to target different bacteria and to incorporate NIR photothermal lysis of pathogens.

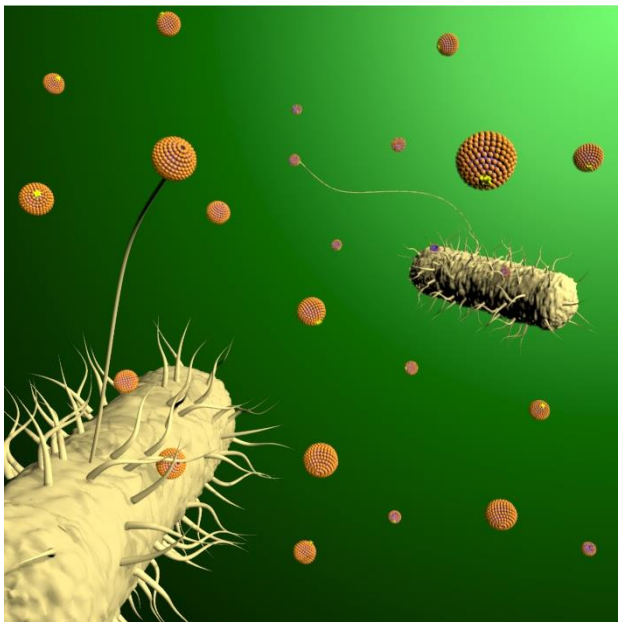

Figure 1- 1. Gold/s-forms M13 bacteriophage targeting *E. coli* for photothermal bactericide.

Chapter 2. ZnO Mineralization on a ZnO-Binding Modified M13 Bacteriophage

2.1 Introduction

ZnO is well studied wide semiconductor with a band gap of 3.37 eV. The most common form of ZnO is the wurtzite crystal structure with the other major structure is zinc blende. Due their electronic, optical and piezoelectricity properties, ZnO nanoparticles have widespread applications ranging from photocatalysis to UV emitters[85]. In medicine, ZnO nanoparticles has been studied as a bactericidal material against both Gram positive and Gram negative bacteria with and without visible or UV radiation. The difference between these two types of bacteria lies in the membrane. The Gram positive membrane is composed of one cytoplasmic membrane with multilayer of peptidoglycan while the Gram negative bacteria is made up of two different membranes: an outer plasma membrane and a second membrane composed of lipopolysaccharide and protein with a layer of peptidoglycan between the membranes. ZnO has been shown to be effective against both Gram-positive and negative bacteria due to the ROS generation. As the M13 bacteriophage targets *E.* coli as its host, it was intended to use ZnO to act as the bactericidal material. Considering that *E. coli* is gram negative, several bactericidal

mechanisms of ZnO were proposed[86–89]. In Hirota et al., it was found that ZnO performed as a bactericidal in dark where superoxide and peroxide were generated[90]. It was found here that the ROS responsible for the bactericidal effect was from superoxide generated[91]. Padmavathy et al. demonstrated ZnO photoactivated under visible and UV to have generated superoxides, hydroxyl and peroxides[92,93]. It was argued here that, due to the negatively charged membrane, superoxides and hydroxyl were not able to penetrate through the membrane and required direct contact of superoxides and hydroxyl for the bactericidal effect to take place. On the other hand, the peroxide would proceed to diffuse into the bacteria and eventually lead to cell death[92]. The other possible killing mechanism is via the release of zinc ions from the ZnO nanoparticles. These, however, were found to be minor compared to the ROS for *E. coli*[94]. Surface defects will also affect the likeliness for an ROS due to the oxygen vacancies[65,66].

Using the M13 bacteriophage as a template as a targeting agent provides two advantages here: directed target to its host and the ability to bring ZnO to the surface of the *E. coli* and as results increase exposure of superoxides and hydroxyls to the membrane. For this to occur, biomineralization of ZnO on phage is necessary. Now, the biomineralization of ZnO has been implemented using a variety of different biotemplates, ranging from butterfly wings to peptides. With the M13 bacteriophage, the pIII phage library has been used to find many ZnO-binding peptides [95–99]. To the best of this author's knowledge, only few papers have studied ZnO synthesis on the M13 bacteriophage[100]. Work by previous lab members constructed a ZnO-binding peptide through the biopanning of combinatorial phage display.[101] Four different motifs were

found: RQ, DE, AGILV and STY. From these four motifs, the following ZnO binding peptide was created: DRQVDATA. Studies by Rothenstein and Gerstel showed that the amino acids found in this peptide were determined to have affinity with ZnO. H and C are associated with Zn^{2+} ion coordination in natural Zn-binding proteins[102,103]. These are further stabilized by acidic (E, D) or hydroxyl-containing residues (S, T). Many peptides found by combinatorial phage and surface display are high in basic residues (H, R, K) and hydrophobic residues (A, G, V, L). The Q amino acid has an amide group which binds to oxygen through a hydrogen bond allowing for binding the oxygen rich plane of the ZnO. Based on these, R, D, T and Q residue were the ones believe to support formation of ZnO nanoparticles. Here, we report the direct synthesis of ZnO on the modified M13 bacteriophage using the DRQVDATA phage.

2.2 Experimental Details

2.1.1 Biomineralization and Characterization Process

A solution of $Zn(NO_3)_2$ at 10 mM was vortexed with 10^9 pfu/µL of the phage. The solution was allowed to rest and incubate at room temperature for 4 days. Three different samples were incubated in these conditions: no phage, wild type and the DRQVDATA phage. Once mineralized, pictures were taken of the samples for visual observations. For in-depth analysis, transmission electron microscope was performed and the size of nanoparticles measured in ImageJ. Energy dispersive spectroscopy was also performed to analyze the elemental composition of the material generated from the phage. Electron diffraction was used to determine the crystallinity of the ZnO.

2.3 Results and discussion

A modified phage with the pVIII peptide insert DRQVDATA was used to template ZnO on the surface of the coat protein. It was found that after an incubation of 4 days in $Zn(NO_3)_2$, large wispy white materials formed in the microcentrifuge tube containing the modified phage as seen in Figure 2-1 (a). The controls, the wild type (Fig. 2-1 (b)) and no-phage samples (not shown), showed no materials formed after the incubation period.

Large bundles of phage were decorated by a thin layer of inorganic material as seen in Figure 2-2 (a). . Across the phage template, polydisperse nanoparticles were randomly distributed along the length of the bundle. Figure 2-2 (b) shows that when the same synthesis method was performed on the wild type, no bundle were formed and the phage was covered by a thin layer of inorganic materials. No nanoparticles were observed on the filaments. It is possible that the thin layer observed in both samples are Zn ions bound to the phage.

The nanoparticles found on the phage were broad in distribution with an average size of 41.1 ± 15.3 nm. These nanoparticles were analyzed using energy dispersive x-ray spectroscopy (EDS). As seen in Figure 2-3, elemental analysis clearly showed that zinc and oxygen are present on the phage. The Cu and P peaks are from the copper grid and phage respectively, while the carbon is from both the grid and the phage. However, electron diffraction only showed diffused rings, indicating that the particles were amorphous.

While the modified phage did not synthesized crystalline ZnO, the pVIII fusion peptide did seem to biomineralize amorphous ZnO to the filamentous phage. It has been shown in the literature that the amino acid histidine and cysteine are associated with Zn^{2+} ion coordination in natural Zn-binding proteins, which are further stabilized by acidic or hydroxyl containing residues[95,102–105]. Many ZnO peptides identified by combinatorial phage and surface display are high in basic residues and hydrophobic residues. Furthermore, the amide group and residual amine in glutamine bind oxygen through a hydrogen bond. The arginine, aspartic acid, threorine and glutamine residue within DRQVDATA may support the formation of amorphous ZnO nanoparticles. The wild type phage on the other hand does contain acidic residue glutamic acid and aspartic acid at the N-terminus of the pVIII protein (AEGD). These may have caused the Zn^{2+} ions to bind along the length of the phage but the absence of the other amino acids prevented the formation of ZnO.

While the amorphous nature of the nanoparticles may be useful for the bactericidal properties of the ZnO/phage nanostructure due to the surface defects[65,66], the low nanoparticle count and the high phage agglomeration makes this ZnO phage unsuitable to be used a bactericide. Agglomerates may inhibit template binding with the *E. coli*.

2.4 Conclusion

In this chapter, we showed that the modified DRQVDATA M13 bacteriophage is able to synthesize ZnO nanoparticles along the length of the phage. These nanoparticles were randomly dispersed along the length of the phage and were found to be amorphous. The peptide was composed of amino acids that are conducive for the growth of ZnO and this was corroborated in the literature. However, due to the low particle count and high phage agglomerations, the phage was found to be unsuitable to be used as a bactericide.

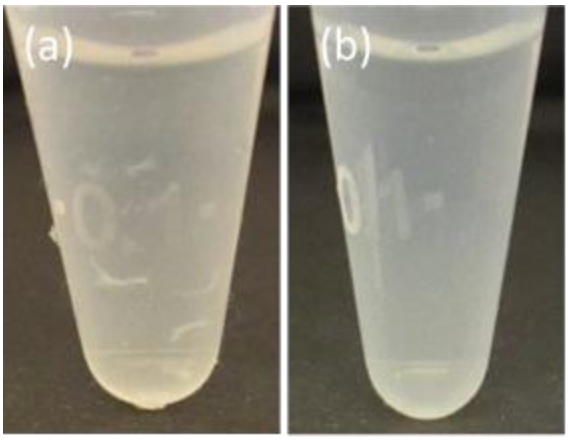

Figure 2- 1. Microcentrifuge tube with (a) DRQVDATA phage and (b) wild type phage post incubation in $Zn(NO_3)_2$

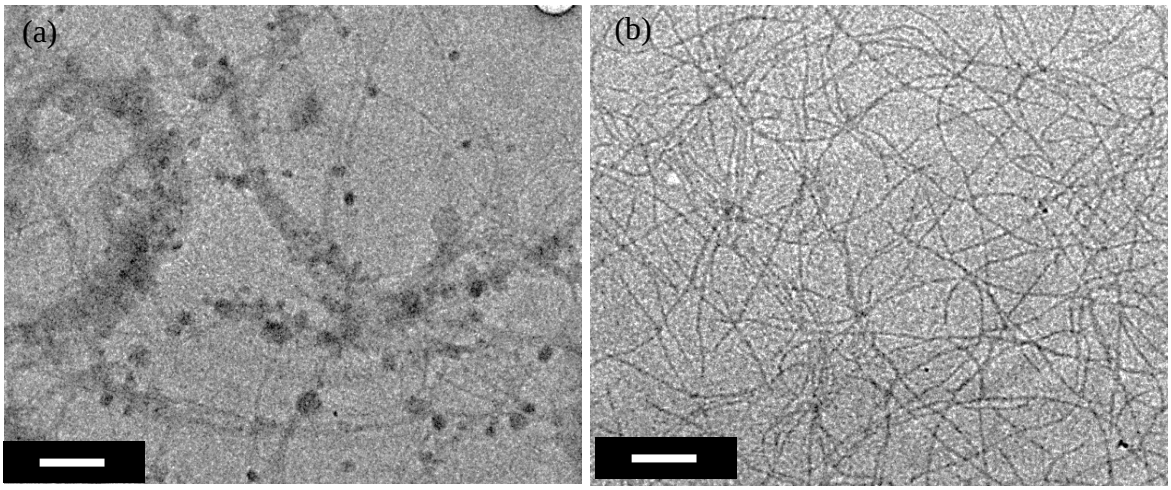

Figure 2- 2. TEM of the (a) wild type and (b) DRQVDATA phage post incubation in $Zn(NO_3)_2$. Scale bar: 200 nm.

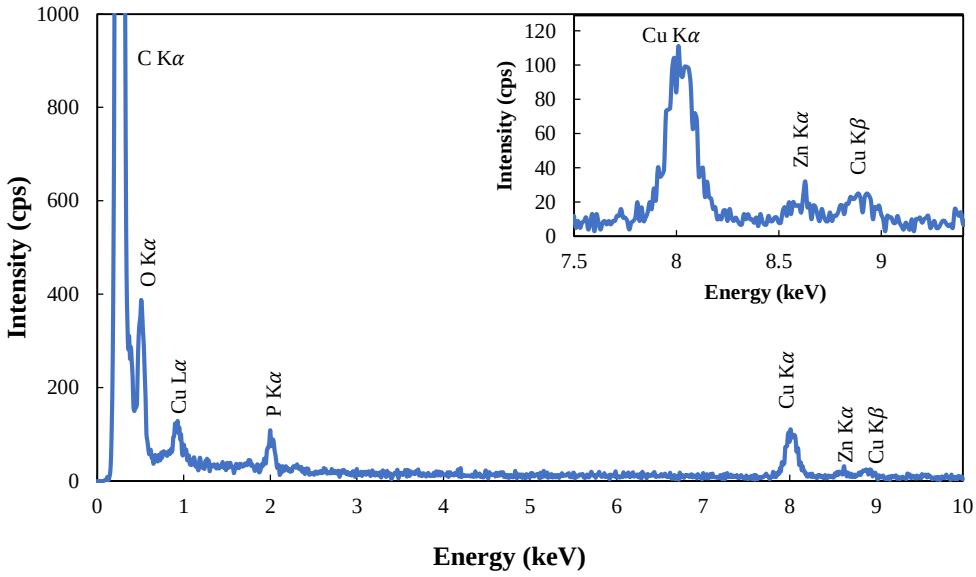

Figure 2- 3. EDS spectroscopy spectrum of the materials grown on the DRQVDATA phage

Chapter 3. Spheroid Transformation

3.1 Introduction

The M13 bacteriophage has the ability, uncommon in the many viruses, to change shape drastically. Upon chloroform mixing, the M13 bacteriophage contracts into either spheroids or i-forms, depending on the transformation conditions. This leads to large change in anisotropy and size where the filamentous phage contracts from a length of about a micron to 100s of nanometers (i-forms) or 10s of nanometers (s-forms)[23,106]. During this process, the pVIII major coat proteins telescopes along the length of the filament[25,107,108]. Modified M13 bacteriophage have been shown to transform into spheroids: chloroform treatment was used as a tool by Petrenko et al., in conjunction with enzyme-linked immunosorbent assay (ELISA), to study the global binding behavior of fusion peptides or "substitute antibodies" located on the fd phage body.[109] Still, more recently, monolayers of bioreceptors for piezoelectric resonator-based bacteria sensors were created from the major coat proteins of ruptured fd spheroids.[110] Although the filamentous form of the Ff class bacteriophage has been used regularly as a scaffold for nanomaterial assembly, its s-form is completely unexplored for this purpose.

In this study, we examined the chloroform-driven conversion of a M13 bacteriophage with pVIII gold-binding peptide fusions and extensively studied in optimization parameters of the transformation process. Our initial experiments were based on spheroid conversion parameters used in Griffith's work[23]. A design of

experiments (DOE) was then used to further develop the transformation procedure for the gold-binding phage, increasing understanding of the main factors which impacted spheroid creation. Spheroid size, % spheroids <100 nm in size, and % filament-to-spheroid conversion where analyzed as experimental outputs. The spheroid size determined the surface area available for gold binding. The percentage of spheroids smaller than 100 nm in size are the particles that have been converted into the spheroids and are not agglomerates or spheroid with severely weakened intermolecular π-π interaction. Finally, the % conversion would clearly show how many of the filaments were transformed into spheroids. This was done to ready the templates for gold binding and gold synthesis studies and to be of a size appropriate to deliver gold nanoparticles to the bacterial membrane described in the subsequent chapter.

3.2 Experimental Details

3.2.1 Transformation of the Spheroids

The transformation of a M13 bacteriophage modified to display a gold-binding peptide sequence, VSGSSPDS[53], at the N-terminus of each pVIII protein was studied. Phage were converted from filamentous to s-form using a chloroform treatment method adapted from previous reports.[23,110] The filamentous gold-binding phage were dispersed in tris-buffered saline (TBS, 50 mM Tris–HCl, 150 mM NaCl, pH 7.5) at a concentration of 10^8 pfu/µl. Equal volumes of phage solution and amylene-stabilized chloroform (99.8%, ACROS Organics) were combined at room temperature to a total volume of 200 µL. The mixture was initially vortexed at high power for 2 s and allowed to stand for 13

s. Subsequently, this process was repeated at low power 1 to 15 times. Following transformation, 90-100 μL of chloroform was removed and air was gently blown over the sample for 15 s to ensure removal of residual chloroform. For comparison, wild-type (unmodified) phage were converted using the same procedure, as well as two other gold-binding filament concentrations (5×10^8 pfu/μl and 1×10^9 pfu/μl).

3.2.3 Agarose Gel Electrophoresis

Phage transformation was characterized via 0.8% agarose gel electrophoresis (AGE). The gels were prepared in 1xTAE buffer (40 mM Tris, 20 mM acetic acid, 1 mM EDTA, pH 7.2) in a 7 x 7 cm tray. Each well was loaded with 45 μL of phage solution and 5 μL of DNA gel loading buffer (10x, 5 Prime). A DNA ladder (exACTGene 1kbPlus DNA ladder, Fisher BioReagents) with fragments ranging from 100 to 10,000 bp was used to monitor virus migration. The electrophoresis was run for 3 hours at different voltages.

The gel was subsequently treated with 0.2 M sodium hydroxide to denature the phage protein coat, stained with ethidium bromide, destained, and imaged under UV illumination. Phage parameters at different phage concentrations and buffers (TBS, PBS and water) were optimized for AGE. Spheroidal transformations at different vortex/rest times were studied. To determine the transformation effectiveness, DNA bands from the phage were analyzed using ImageJ where band peak was measured and compared to the DNA ladder and the filamentous phage band. Observations in the streak were also noted.

3.2.4 Circular Dichroism (CD) Measurements

In order to study the secondary structure of the major coat protein (pVIII) during the transformation process, spectra of filaments and spheroids were collected using a circular dichroism (CD) spectrometer (JASCO, J-815). Measurements were taken at different stages of transformation from 0 to 16 vortex cycles. These measurements were performed at room temperature in the wavelength range of 205 to 235 nm. The instrument settings were as follows: 50 nm/min scan speed, 1 nm bandwidth, 4 s response time, and 12 scan accumulations. To improve the signal-to-noise ratio, three samples were measured and averaged at each vortex condition.

3.2.5 Transmission Electron Microscopy (TEM) Sample Preparation and Characterization

A transmission electron microscope (TEM, Tecnai T12) was used to examine the size and shape of the gold-binding phage before and after transformation, as well as to study its gold binding and synthesis capabilities. For this analysis, a 5 µL sample volume was pipetted onto a formvar/carbon-coated copper grid (Ted Pella, Inc.), incubated for 5 min, rinsed twice with deionized water, and wicked dry with filter paper. Prior to drying, samples without gold were stained with uranyl acetate[111]. ImageJ software was used for TEM image processing and analysis. An ellipse was fitted to each spheroid, and major and minor axes lengths were measured and averaged. To separate spheroids from other possible structures such as i-forms and filaments, structures with an aspect ratio > 3 were excluded.

3.2.6 Ultraviolet-Visible (UV-Vis) Spectroscopy

Ultraviolet-visible (UV-Vis) absorption spectroscopy (ThermoFisher, Evolution 60) was used to evaluate the phage concentration before and after transformation. Using a quartz cuvette with a 10 mm optical path length, measurements were made from 220 nm to 380 nm. The concentration of the filamentous and spheroidal templates were quantified via a previously published protocol.[7] Due to significant geometric change associated with transformation, the absorbance spectra of the spheroids were corrected for Rayleigh scattering as described by Porterfield et al.[112] In brief, a two point approximation of wavelength-dependent scattering (λ^{-4}) was estimated at 340 nm and 360 nm where minimal absorbance was expected from viral proteins and nucleic acids.

3.3 Results and Discussion

3.3.1 Transformation Development

3.3.1.1 Agarose Gel Electrophoresis

Initial experiments to determine the transformation parameters of the gold-binding phage were done using whole virion agarose gel electrophoresis (AGE). Previous work performed in Olsen[110], showed that when the filaments and spheroids each migrated at different speed, with the spheroids being faster than the filaments. As a result, the spheroids migrated further down the lanes when compared with the filaments. The gold-binding filamentous phage were initially studied through AGE. The parameters that were looked into are as followed: phage mass, phage buffer and voltage. Phage mass dictated the amount of DNA in the lane and hence the visibility of the ethidium bromide DNA stain as it is a function of concentration. Too large of a concentration caused smearing in the lane. The choice of buffer affected the ion concentration and thus the charge screening and the mobility of the phage. The voltage affected the speed at which the phage moved through the gel but with too high of a voltage and smearing occurred in the lane. Different concentration of phage, matching a range of DNA mass ranging from 20 ng to 500 ng, were prepared in phosphate saline buffer (PBS) in accordance to the work by Olsen et al[110]. A voltage of 60V over a runtime of 60 minutes was used. Figure 3-1 shows that concentrations above 150 ng had a smeared band.

The next set of experiment compared buffers: water, TBS and PBS. Water was the original buffer used previously in preliminary experiments of phage transformation,

TBS was the buffer the phage was stored in and PBS was the buffer used in Olsen. DNA mass was set at 450 ng. Figure 3-2 showed with PBS (lane 3), the filamentous phage barely moved and heavy smearing occurred. Using TBS (lane 5), the phage moved faster but the band remained heavily smeared. Water (lane 7, as a buffer, yielded the best results with a clear define band with some smearing. While water alleviated the smearing and showed a band, it is possible that the mass remained too high and thus contributed heavily to the smearing. This may be a reason for the heavy smearing in TBS.

To reduce the smearing, the voltage was dropped to 50V, the time increased to 120 minutes to compensate for the lower voltage. Figure 3-3 shows AGE performed on DNA mass of 150 and 450 ng in water and TBS. All lanes showed that the lower voltage reduced smearing across the board. At 450 ng, Lane 2 showed the filament band remained strong with a faint smear trail. The lower phage concentration seen in lane 3 showed a faint band where the filaments was expected to be. The smearing here was almost nonexistent when compared to lane 2. The samples in TBS, on the other hand, still remained smeared, showing that the buffer was the bigger factor.

Based on this, the transformation process initially used the following parameters: 150 ng, 50V, and 120 minutes running time. The spheroids were transformed at 10^9 pfu/μL, power 10, 10/35 seconds vortex rest cycles, upright position. An additional lane was added at 1500 ng to ensure that a band could be detected. Figure 3-5 showed that for a mass of 150 ng, little to no band was detectable. At 1500 ng, a strong band with trail smear was observed. The lack of band from the 150 ng seemed to indicate that either the conversion was not at 100% or the spheroids were of various size, hence spreading the

total mass across the entire length of the lane. This was confirmed by the heavy streaking in the 1500 ng. However, 1500 ng was too high a mass for the gold binding experiments. The mass was reduced to 850 ng. Figure 3-5 showed that the experiment yielded a strong band and was indeed repeatable. With the mass, voltage and running time fixed, the optimization process for the transformation was then performed.

3.3.1.2 Transformation Optimization via AGE

There are several parameters that affect the transformation of the M13 bacteriophage. Griffith and Manning provides two major parameters: the number of cycles and the vortex/rest time.[23,106] There are however, several other parameters that have to be taken into account: power (or vortex speed), phage concentration, and orientation of the tube with respect to the vortexer. The following parameters were investigated: power, vortex time and rest time. Different vortex/rest time were chosen for a total cycle time of 45s. Vortex time ranged from 5 s to 20 s with the remainder of the 45 s as the rest time over total time of 3 min. To determine the highest spheroid conversion, the band brightness peak ratio between the 4th peak of the DNA ladder and the spheroid lane were compared between each sample. Figure 3-6 shows the phage transformed at various power, vortex and rest time. Lane 8 shows that at power 7, a majority of the phage remains untransformed. Across the different vortex time, lane 6 showed the highest peak ratio of 1.07. This seems to indicate that a shorter vortex time yields the higher yield.

To further optimize the transformation, two different rest times were investigated. As a control, 40 s was used as the rest time with 5 s vortex time over 5 cycles. The other time was chosen at 10 s rest time with 5s vortex time over 5 cycles. Based on the results, 1 min had the highest ratio of 1.21 ± 0.02. On the other hand, 3 minutes yielded an average of 1.07 ± 0.05.

Figure 3-7 shows that under these conditions, all the filaments are converted but the spheroids were agglomerated and had a large diameter various size, with an average size of 96 ± 46 nm. The major problem with using the AGE to create spheroids is twofold: it is impossible to determine the size of the spheroids based off the bands only and the concentration limit prevents further studies into the effect of lower concentrations and using different buffers.

3.3.1.3 Concentration and Microcentrifuge Orientation Study

Initial experiments at lower concentration in TBS buffer and lower power yielded improved results in terms of size and removal of agglomerates from the transformation performed during the AGE development process. At power 10 and concentration at 5 x 10^8 pfu/µL over 5 cycles, the phage transformed into spheroids that were 96 ± 95 nm with more than 50% transformed. Bringing the power down to 5 at 5 x 10^8 pfu/µL, Figure 3-9 (a) shows the results: spheroids that are 50 ± 19 nm in diameter. However only, 30% of the phage were transformed into spheroids. To improve conversion yield, the orientation of the tube was investigated where the transformation was done using a microcentrifuge tube in the upright position vs. the sideway position. The following

parameters were used for this experiment: a concentration of 5 x 10^8 pfu/μL was used at power 5, cycle number of 4 and vortex/rest time of 5 s/ 12s.

Figure 3-9 (b) shows that the position of the tube made a drastic difference in the conversion efficiency of the spheroids. In the upright position of the microcentrifuge yielded spheroids that were 50 ± 19 nm in diameter but only 30% were converted into spheroids. The sideways position of the tube on the other hand converted virtually all of the filaments into spheroids: only 1% of the filament remained. These spheroids were, however, larger in diameter with a greater standard deviation: 63 ± 38 nm. This extreme difference in conversion efficiency can be attributed to the increased surface area available for the filaments to come into contact with a water/chloroform interface. In the upright position of the microcentrifuge tube, both the volume of the water and chloroform are constrained in the narrow part of the tube, hence the interface is only limited to the diameter of the tube. While the vortexing process does create more water/interfaces, it appears that the volumes were unable to mix properly. Placing the tube sideway increased the contact area for the chloroform and water in two ways. The first way both the water and chloroform spread on the surface of the tube increasing the available area. The vortexing of the sideway tube also seemed to have created more interfaces for the filaments to interact with. This in turn to the already transformed phage to be exposed for longer period of times with the chloroform/water interface and pushes the transformation process for a longer period of time, causing the spheroids to become larger in diameter.

3.3.1.4 Design of Experiments: Power vs. Cycle

While the conversion efficiency was drastically improved, optimization of the transformation was required. To understand the possible interactions between each parameter and the effect of the parameters on the transformation procedure, several designs of experiments (DOEs) were done to study the transformation procedure. To evaluate the effect of each parameter, spheroidal size, % sub 100 nm spheroids and % converted spheroids were chosen as the outputs. The spheroidal size and % sub 100 nm were picked because these indicated spheroid stability and non-agglomerated spheroids, respectively. Any particle larger than 100 nm could be an agglomerate and smaller agglomerates can be hard to distinguish from an individual spheroid. In the first set of experiments, the two factors that were studied were vortex power and the number of cycles. Vortex power is an important factor since it controls how much of the chloroform mixes up with the water. The number of cycles on the other hand dictates the number of times the phage is exposed to the multitude of chloroform/water interfaces. Table 3-1 shows the lows and the highs. The concentration is kept at 5×10^8 pfu/µL while the vortex time is set at 5 s with 10 s of rest time. The high values for both the power and cycle numbers were based on previously mentioned experiments and this gives us a benchmark to determine the effect and interaction of the factors. The effects of the power and cycles are represented in Figure 3-10 and Table 3-2.

Table 3- 1. Power vs. Cycle number values for low and high

Factor	Low (-)	High (+)
Power	1	5
Cycle number	1	4

Table 3- 2. Design of experiments value for cycles vs. power

	LoHi	**HiHi**	**LoLo**	**HiLo**
Average (nm)	68	85	62	81
StDev (nm)	51	73	34	54
Median (nm)	58	66.5	56	62
% <100 nm	88	77	92	82
% converted	31	90	25	79

For the low cycle and low power, the spheroid yield was poor where only 25% of the filaments were converted. Size-wise, these spheroids were 62 ± 34 nm in diameter with a median at 56 nm. 92% of the converted phage were sub 100 nm showing that there were almost no agglomerates. With low cycle and high power, the spheroid yield slightly improved from 25% to 30% converted. A few agglomerations were observed as can been seen in Fig. 3-9 and this is further confirmed with 88% of the spheroids being sub 100 nm. The spheroid diameter increased slightly to 68 nm. The high cycle and low power

yielded 79% converted with spheroids that were 81 nm. The % sub 100 nm slightly decrease to 82%. The high cycle and power had the greatest yield at 90% conversion but with large spheroids of 85 ± 66 nm. The % sub 100 nm was found to be at 77%.

In terms of effect and interaction, Figure 3-11 shows both a plot of the averages and the Pareto chart for all factors and outputs. In all cases, cycles had the greatest effect. In terms of size, the higher the number of cycles, the greater the size. Similarly, the effect was positive on the standard deviation for the longer cycles and the higher yield of spheroids. On the other hand, the effect of power was negative on the formation of the sub 100 nm spheroids. This can be explained by the higher number of cycles leading to more chloroform/water interfaces and hence exposing more filaments and the already transformed phage to more chloroform, leading to the formation of more spheroids and for the already transformed spheroid to become larger. Compared to the number of cycles, the power factor was a secondary effect in all cases. Similarly, to the number of cycles, Figure 3-11 shows that power also had a positive effect on size and % converted, while being negative on the % sub 100 nm spheroids. Based on this, it can be speculated that the vigorous the shaking, the more likely a spheroid can interact with the chloroform/water interface due to greater number of interfaces and increase mobility of the phage particle in the solution. It is also possible that the heavy shaking make destabilize the spheroids more and thus make them larger in size. While the effect is positive, the smaller effect may be due to the phage mobility induced from the shaking, is weaker than the cycle number. In terms of interactions, the effect across the board were

negligible and hence the interaction between power and the number of cycles are not significant.

Based on these results, a power of 1 was selected for power. The lowest power provided relatively small spheroids and the greater percentage of spheroids being sub 100 nm when compared with the high power of 5. However, the conversion rate was smaller for the lower power but this could be changed with the addition of extra cycles. In terms of cycle number, the greater the better. Regardless of size, the higher number of cycles delivered the results needed for % conversion, with the highest yielding 90% spheroids.

3.3.1.5 Design of Experiments: Vortex Time and Concentration

Vortex time and concentration were the next factors to be investigated. The vortex time dictates the length of exposure to chloroform for each cycle. It was hypothesized that the longer the time, the more spheroids would be formed. This lengthened time may also affect the stability of the spheroids and formation of agglomerations. Concentration is also another important factor. In this case, a higher concentration could interfere in the transformation where less filaments are able to come into contact with the interface. Table 3-3 shows the lows and highs for both of the new factors. The output remains the same as described previously. The cycle number is kept at 3 cycles with the power set at 1. The effects of vortex time and concentration are represented in Figure 3-12 and table 3-3.

Table 3- 3. Vortex time vs. concentration number values for low and high

Factor	**Low (-)**	**High (+)**
Vortex time (s)	2	5
Concentration (pfu/µL)	$1x10^8$	$5x10^8$

Table 3- 4. Design of experiments value for cycles vs power

	LoHi	**HiHi**	**LoLo**	**HiLo**
Average (nm)	71	83	53	73
StDev (nm)	47	48	22	55
Median (nm)	56	70	49	54.5
% <100 nm	84	75.4	97	82
% Converted	27	90	52	65

The low vortex time and low concentration showed a 52% yield with 97% of the spheroids being less than 100 nm in diameter. These spheroids were 53 ± 22 nm with a median of 49 nm. When the vortex time is maintained to 2 with a high concentration, the % spheroid converted drastically drops to 27% with the percentage of sub 100 nm

spheroids dropping to 84%. In terms of size, the average diameter is 71 ± 47 nm with a median of 56 nm. In contrast, with a high vortex time at a lower concentration, the % converted goes up to 64%. However, the percentage of sub 100 spheroids drops to 82%. The spheroids are 73 ± 55 nm with a median of 55 nm. The high vortex time and concentration resulted in spheroids that were 83 ± 48 nm with a median of 70 nm and yielded 90% spheroids. Only 75% of the spheroids were sub 100 nm.

Figure 3-13 shows that vortex time and concentration have a positive effect on the diameter of the spheroids. Considering that the increase vortex time means further exposure to the chloroform, it is of no surprise that the size also increases. Interestingly, concentration had the greatest effect on size. The interaction of vortex time and concentration was shown to have the least effect. In terms of % sub 100 nm, all factors and interaction was shown to be negative. Concentration, once again, had the greatest effect. This directly relates to the size increase of the spheroids trapped at the interface. Furthermore, spheroids that are trapped may also come into contact with one another and form agglomerates. All of this leads a decrease in the number of sub 100 nm spheroids. Vortex time had a similar effect where the spheroids were exposed for a longer period of time and thus lead to >100 nm particles. Again, the interaction between the concentration and vortex time were negligible. Finally, Figure 3-13 showed that vortex time and the interaction had a positive effect on the % conversion while the concentration had a negative impact. While the vortex time had the greatest impact, concentration effect was also relatively significant. Considering that the vortex time increases of direct exposure of phage to chloroform, this lead to the increase of both the size and the % conversion

while further increasing the number of spheroids larger than 100 nm and the formation of additional agglomerates. Interestingly enough, the higher concentration lead to a lower conversion rate and worsen the spheroid stability along with increasing the size. This may have caused the interference with the migration of the spheroids away from the interface. The number of other phage particles may have blocked the spheroids from moving away. This indirectly increases the exposure time and thus increases the size of the spheroids. This is further backed by the low yield at higher concentrations and the increase of particle bigger than 100 nm.

Based on these results, the low concentration was chosen as the optimal concentration for all subsequent transformation. While the vortex time did improve the conversion rate, the conversion efficiency was only improved by 14%. The % of sub 100 nm spheroids took too much of a hit. Hence, the low vortex time was chosen. With the two design of experiments, the parameters chosen were a concentration of 10^8 pfu/μL, a power of 1 and a vortex time of 2 s.

3.3.1.5 Optimizing number of cycles

Based on the parameters from above along with the gold-binding phage, we further optimize the number of cycles, a series of experiments was conducted ranging from 1 cycle to 16 cycles. In an early experiment, a serendipitous mistake demonstrated that a strong burst at power 10 in the first cycle followed by power 1 for all subsequent cycles yielded spheroids with smaller standard deviations (data not shown). Cycle-by-cycle TEM images, shown in Fig. 3-14, revealed that the structurally affected pVIII

proteins detected were not uniformly distributed throughout the chloroform-treated M13 bacteriophage, but rather, heavily concentrated within specific phage. That is, whereas some viruses were completely transformed into spheroids within the initial vortex cycles, other viruses were seemingly entirely unchanged and remained filaments. With increased cycle number, more spheroids were produced until, at high cycle numbers, spheroids became the dominant geometry. In addition, a small, gradual increase in spheroid size was measured with successive vortex cycles (Fig. 3-15).

Although filaments and spheroids were the most prevalent structures found within the chloroform-treated samples, a few large irregularly-shaped assemblies, on the order of a few hundred nanometers, were also observed, particularly at higher cycle numbers. Such structures may be derived from aggregates of s-forms and/or i-forms created either during chloroform treatment or TEM sample preparation. Although not evident in all reports of chloroform-treated M13 phage[24,110], the presence of agglomerates and i-forms was previously described by Olsen et al.[110].

3.3.2 Circular Dichroism and UV-Vis Spectroscopy Analysis

A cycle-by-cycle investigation of the transformation process for the gold-binding phage using circular dichroism (CD) measurements revealed a progressive decrease in molar ellipticity. CD spectra from the gold-binding phage are shown in Figure 3-16. When assembled within the M13 filamentous form, the pVIII protein has an alpha-helix secondary structure.[7,113,114] Upon transformation via interaction with chloroform, the pVIII protein undergoes a structural change which is similar to that experienced during

host infection.[23,27] As illustrated in Figure 3-17, the pVIII is believed to shift from a single, somewhat curved alpha-helix to an L-shaped structure composed of two distinct alpha-helices connected by a loop region.[115–117] This conformational change has been associated with a reduction of helicity from 90% to about 60%[26], as well as weakened chromophore coupling between tryptophan and phenylalanine residues on neighboring proteins.[118]

Because the major coat protein accounts for more than 85% of the mass of the viral capsid[7,119] and 99% of the protein mass[120], these structural changes dictate the CD spectrum and can be readily observed.[121] The signature ellipticity of an alpha-helix structure within the deep UV region, includes negative bands at 222 nm and 208 nm.[106,117,122,123] As shown in Fig. 3-16, both 222 nm and 208 nm band intensities of the gold-binding phage decreased when vortexed with chloroform. Specifically, the ellipticity of the 222 nm band steadily decreased from cycle 0 to 6. Beyond cycle 6, the rate of decrease of molar ellipticity per cycle slowed substantially such that very little additional reduction was observed. The initial decrease in 222 nm band ellipticity with cycle number was attributed to the combined effect of diminished helicity and reduced π-stacking interaction between adjacent pVIII molecules. At higher cycle numbers, it is believed that the majority of the pVIII molecules were converted to the L-shaped structure therefore the reduction in the negative 222 nm band plateaued.

Based on CD and TEM data, phage transformed using 5 vortex cycles were selected for further investigation. These gold-binding phage displayed sufficiently reduced 222 nm band ellipticity, as well as 100% filament-to-spheroid conversion. In

addition, absorbance spectra indicated that the template concentration was essentially retained (99.8%, Fig. 3-18) post transformation. The spheroidal absorbance peak was corrected for Rayleigh scattering.

Figure 3-19 shows the morphology of the filamentous and the spheroidal gold-binding phage before (0 vortex cycles) and after chloroform treatment (5 vortex cycles), respectively. Prior to chloroform treatment, the gold-binding phage were filaments 912 ± 14 nm long. This is slightly larger than the unmodified, M13 wild-type phage which is approximately 880 nm long.[120] The length of filamentous phage is determined by the enclosed genome and can range from 50 to 2000 nm or more depending on the scope of the genetic modification.[124–126] As is apparent in Figure 3-17 and reinforced by Figure 3-20, the significantly contracted gold-binding spheroids had a rounded, slightly deflated characteristic shape.

The average size (59 ± 16 nm) and size distribution of the spheroids is shown in Figure 3-21.The s-form size was consistent across samples (Figure 3-22). For comparison, wild-type M13 phage were transformed using the same procedure and the corresponding spheroid size distribution is shown in Figure 3-23. The spheroidal wild-type phage were slightly smaller than the s-forms produced from gold-binding phage (53 ± 9 nm), in addition a significant number of wild-type filaments (~44%) were still present. Discrepancies in spheroid size and conversion efficiency may be associated with differences in interaction among modified (gold-binding) and unmodified (wild-type) pVIII coat proteins within the viral capsid. Further studies are necessary to better understand the role of peptide fusions on template transformation. Initial phage

concentration had a small impact on spheroid size (Figure 3-24) and conversion efficiency. Increased template concentrations of 5 x 10^8 pfu/µl and 1 x 10^9 pfu/µl produced spheroids 61 ± 18 nm in size with ~98% efficiency and spheroids 65 ± 20 nm in size with ~96% efficiency, respectively.

3.4 Conclusion

In conclusion, we have studied the chloroform-triggered transformation of a gold-binding M13 bacteriophage. Through a design of experiments, it was found that the main factors affecting the transformations were cycle number, vortex time and phage concentration. Analyzing both TEM micrographs and circular dichroism, it was determined that a vortex time of 2 s, a phage concentration of 10^8 pfu/µL and a cycle number of 5 were parameters to be used to make gold-binding bactericidal templates. Spheroids generated with these conditions were 59 ± 16 nm in diameter with 100% of the filaments converted. Curiously, using the same procedure, somewhat larger and comparatively more spheroids were produced from the gold-binding phage than the wild-type phage. A change in pVIII protein-protein interactions within the viral coat caused by the peptide insert could be the source of size and conversion efficiency differences. More studies are necessary to better understand this phenomenon and possibly allow for spheroid size tunability. With the spheroid transformed, the gold binding and synthesis properties of the phage still remains to be determined.

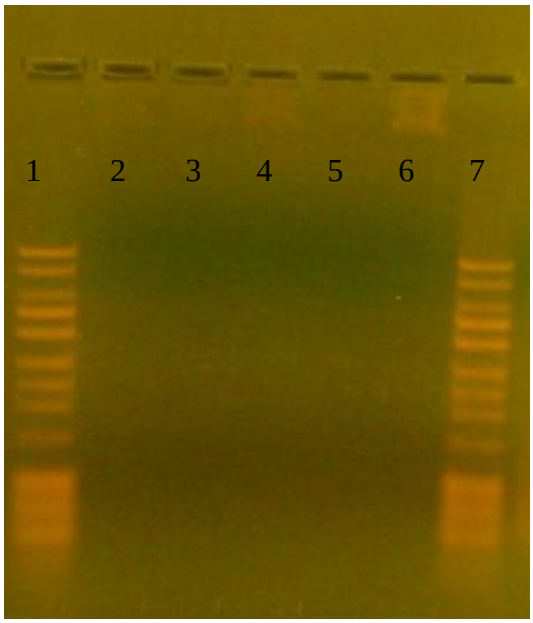

Figure 3- 1. AGE at different phage DNA concentrations. Lane 1: DNA ladder; Lane 2: 150 ng; Lane 3: 85 ng; Lane 4: 300 ng; Lane 5: 20 ng; Lane 6: 450 ng; Lane 7: DNA ladder

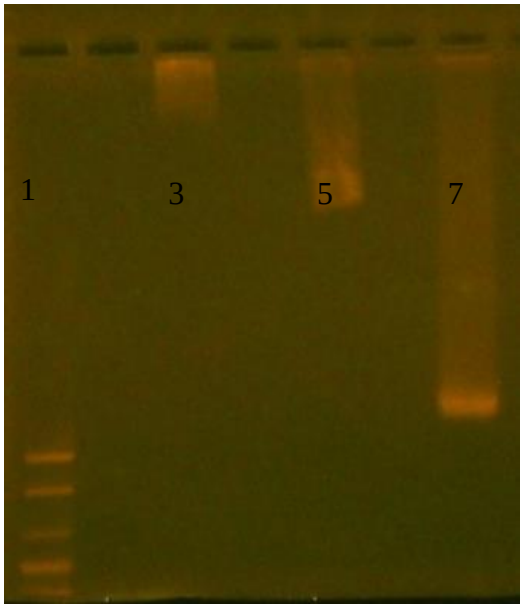

Figure 3- 2. AGE of filamentous phage in different buffer. Lane 1: DNA ladder; Lane 3: PBS; Lane 5: TBS; Lane 7: Water

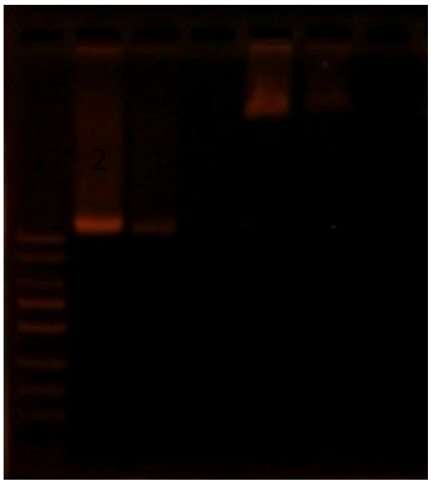

Figure 3- 3. AGE of filamentous phage in different buffer and at different phage concentration. Lane 1: DNA ladder; Lane 2: 450 ng in water; Lane 3: 150 ng in water; Lane 5: 450 ng in TBS; Lane 6: 150 ng in water

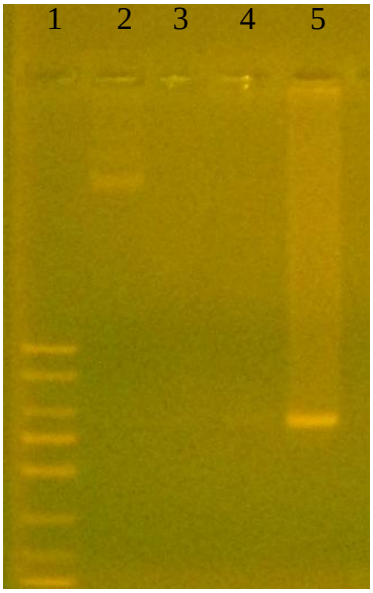

Figure 3- 4. AGE of spheroids and filaments at 50V under different concentrations. Lane 1: DNA ladder; Lane 2: filamentous phage at 150 ng; Lane 3 and 4: spheroids at 150 ng; Lane 5: spheroids at 1500 ng

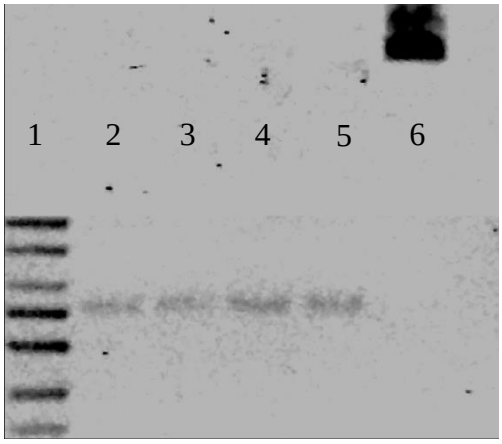

Figure 3- 5. AGE of spheroids at the same concentration of 850 ng. Lane 1: DNA ladder; Lane 2-5: spheroids at 850 ng; Lane 6: filaments at 850 ng

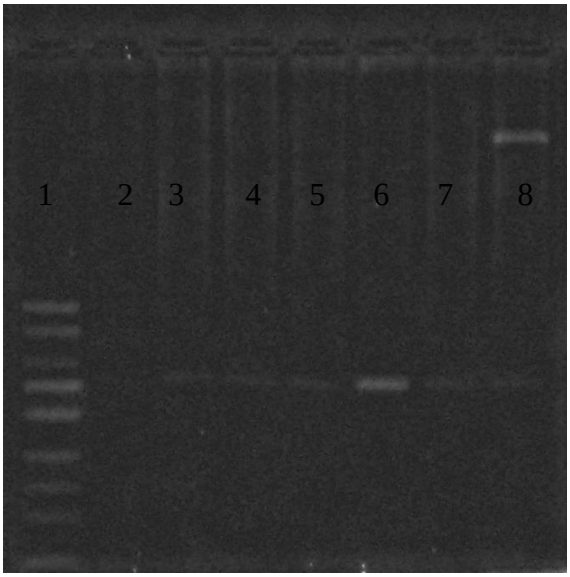

Figure 3- 6. AGE of spheroids at the different vortex rest times over a total time of 3 minutes at power 10. Lane 1: DNA ladder; Lane 2-3: spheroids at 10 s/35 s; Lane 4-5: spheroids at 20 s/25 s; Lane 5-6: spheroids at 5 s/40 s; Lane 8: spheroids at 5 s/40 s at power 7.

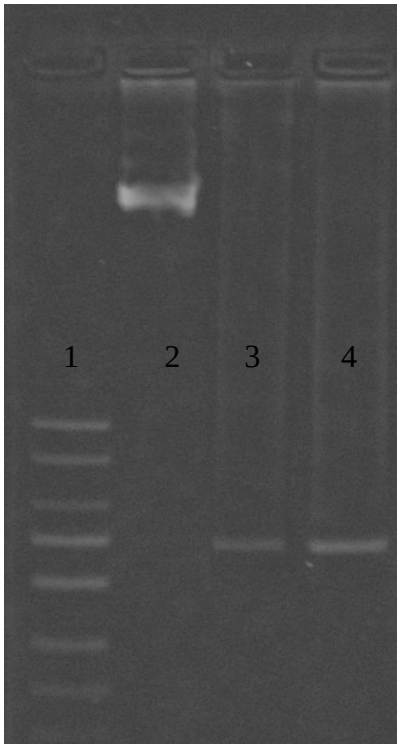

Figure 3- 7. AGE of spheroids at the different vortex times over a total time of 3 minutes at power 10. Lane 1: DNA ladder; Lane 2: filamentous phage; Lane 3: spheroids transformed at 5 s/40 s over 3 minutes; Lane 4: spheroids transformed at 5 s/12 s over 1 minute.

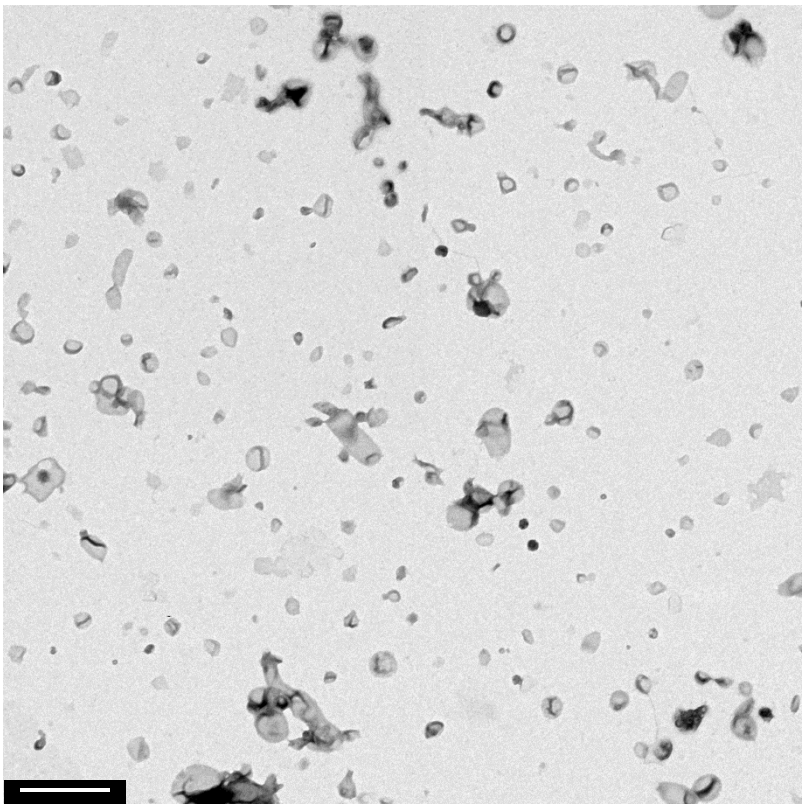

Figure 3- 8. TEM of spheroids transformed at 5 s/12 s vortex rest time over 1 minute. Scale bar: 500 nm.

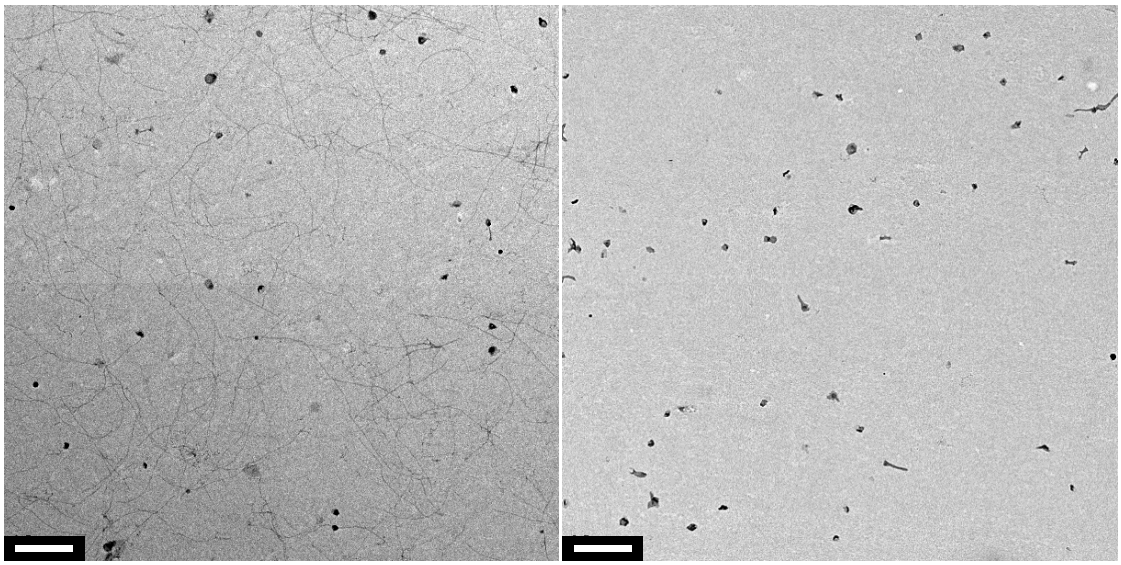

Figure 3- 9. TEM of spheroids transformed at 5 s/12 s vortex rest time over 1 minute in the (a) upright position and (b) sideways. Scale bar: 500 nm.

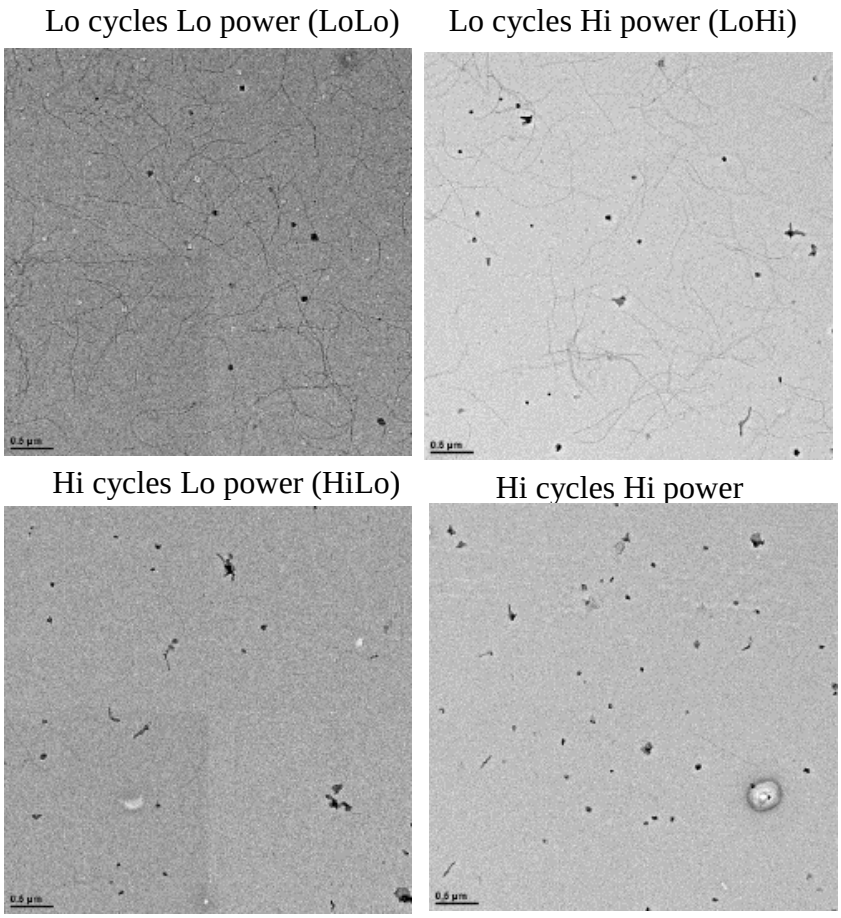

Figure 3- 10. TEM images of the DOE outcome of the cycles vs. power.

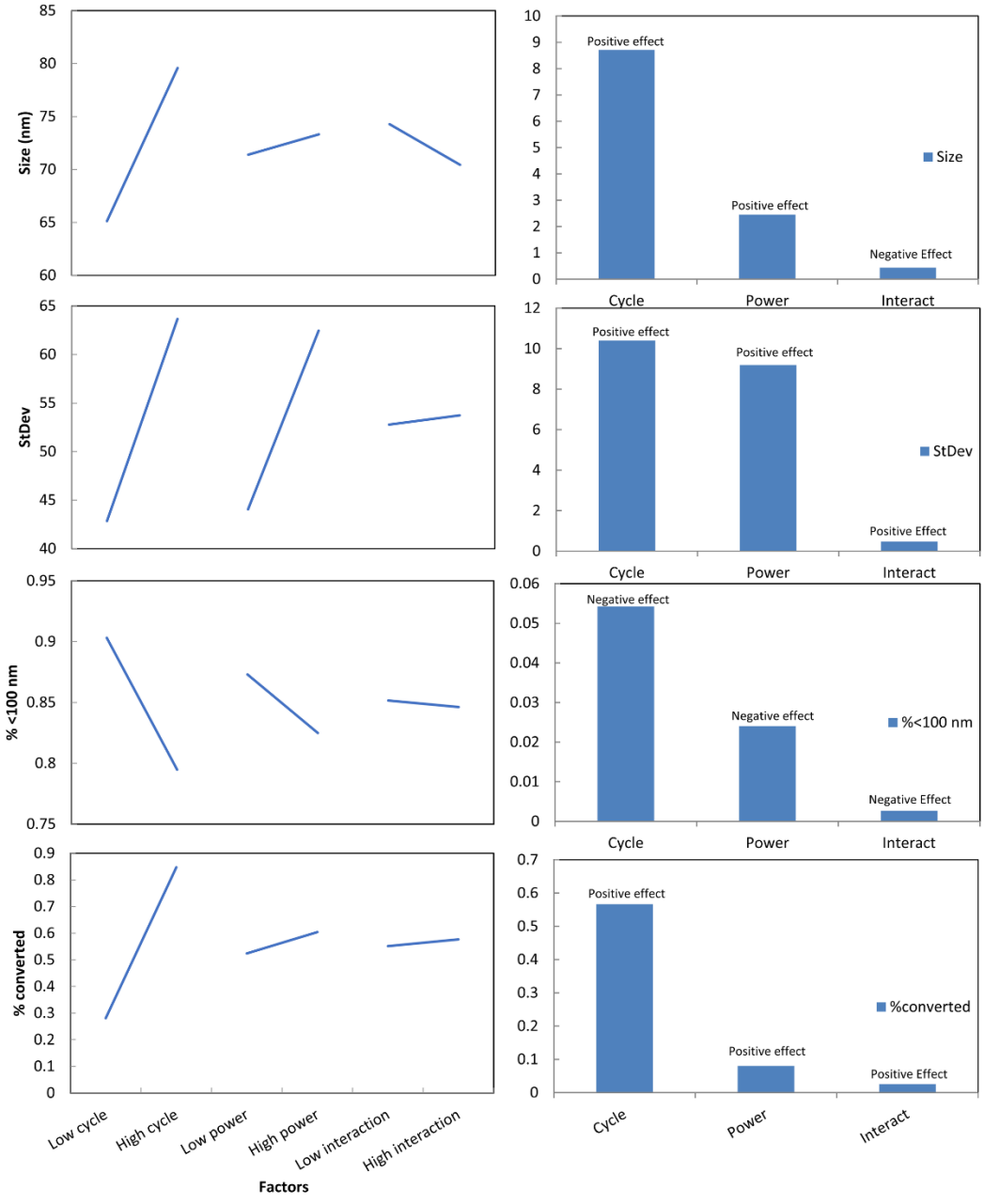

Figure 3- 11. Plot of averages and Pareto of cycles vs power.

Lo V. Time Lo concentration

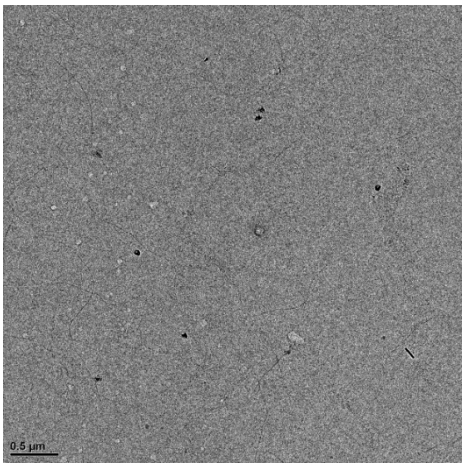

Lo V. time Hi concentration (LoHi)

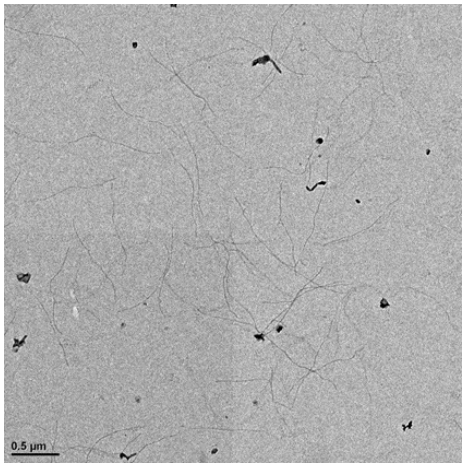

Hi V. Time Lo concentration (HiLo)

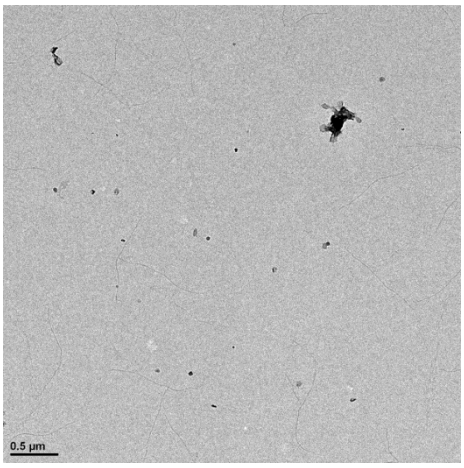

Hi V. Time Hi concentration (HiHi)

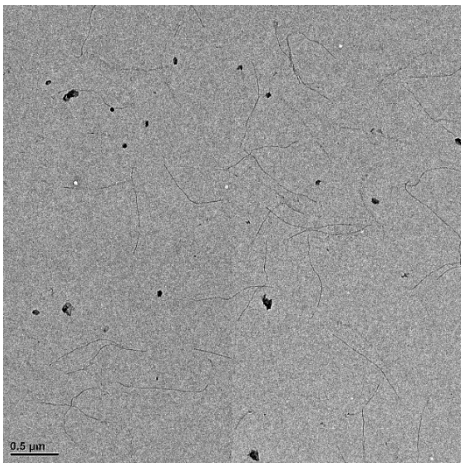

Figure 3- 12. TEM images of the DOE outcomes of the vortex vs. concentration

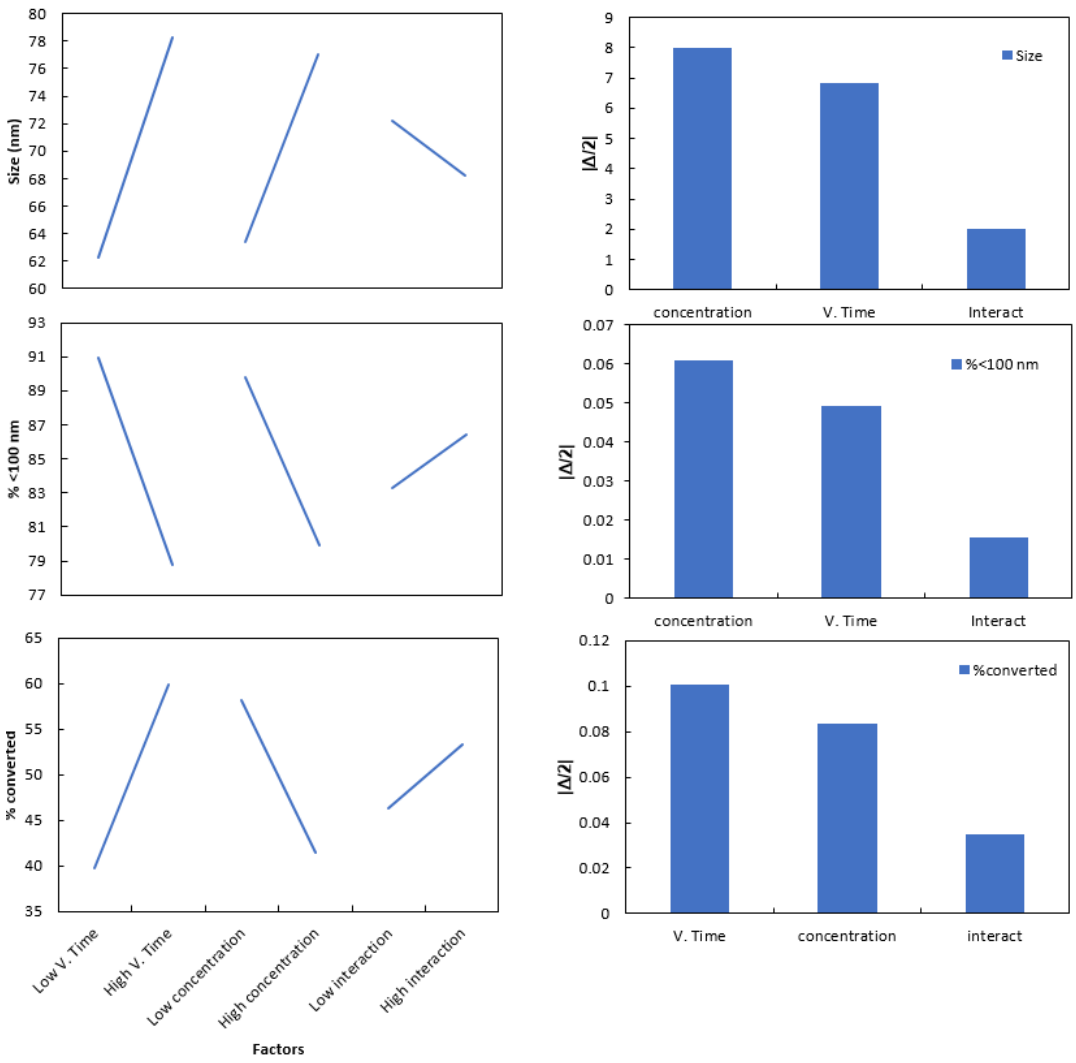

Figure 3- 13. Plot of averages and Pareto of vortex time vs concentration

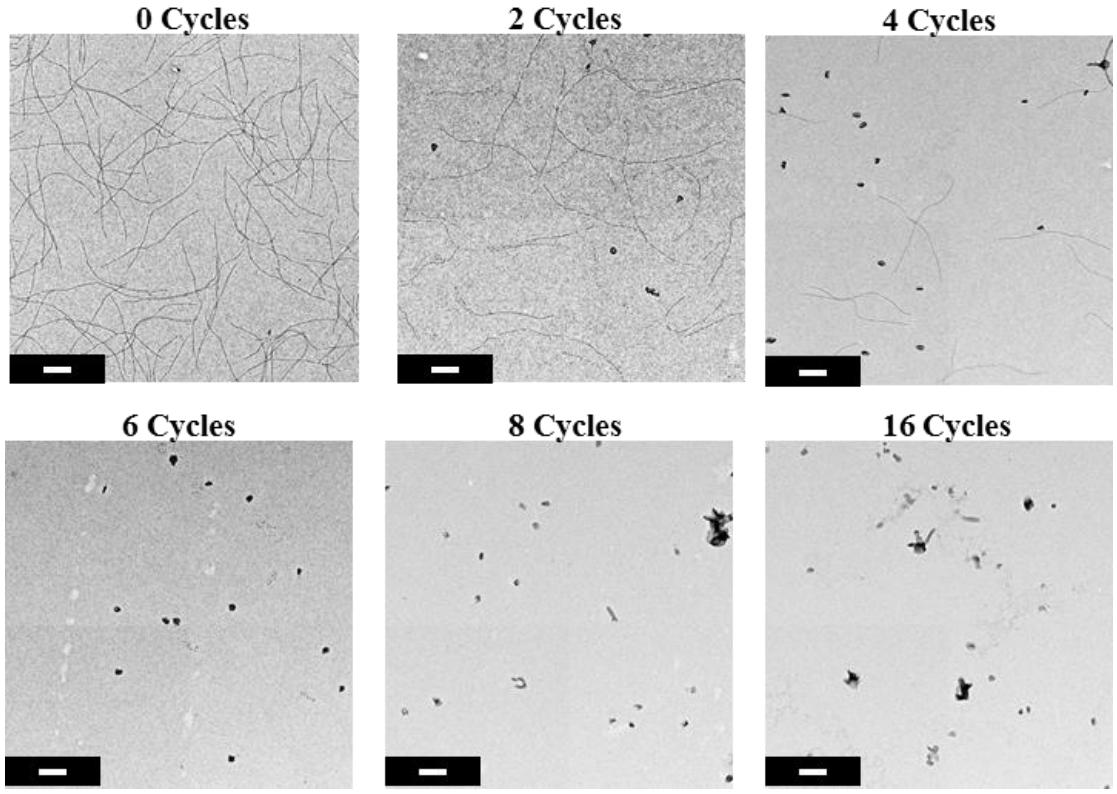

Figure 3- 14. Transmission electron microscopy (TEM) images of the gold-binding phage transformation progression with increasing cycle number. Scale bar: 200 nm.

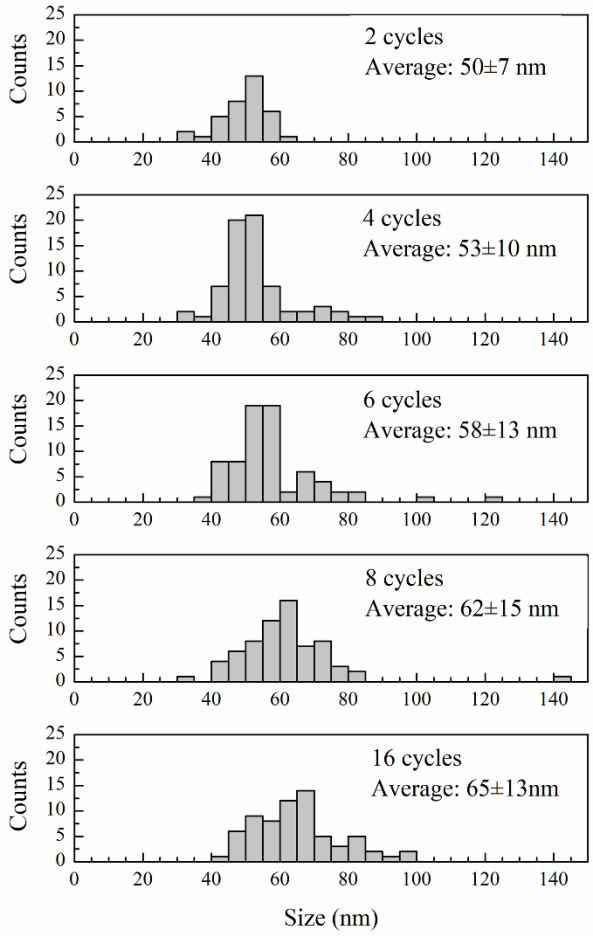

Figure 3- 15. Histograms of gold-binding M13 spheroid size distributions with increasing chloroform treatment cycle number.

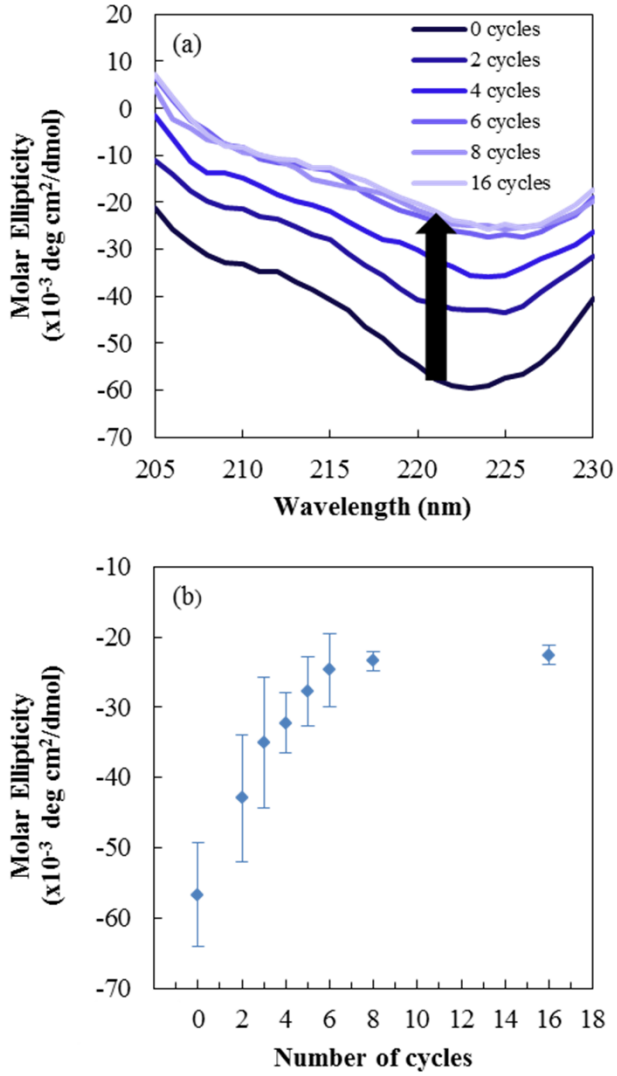

Figure 3- 16. (a) Circular dichroism (CD) spectra and (b) 222 nm molar ellipticity values for gold-binding M13 bacteriophage measured as a function of cycle number. The black arrow in (a) indicates increasing cycle number.

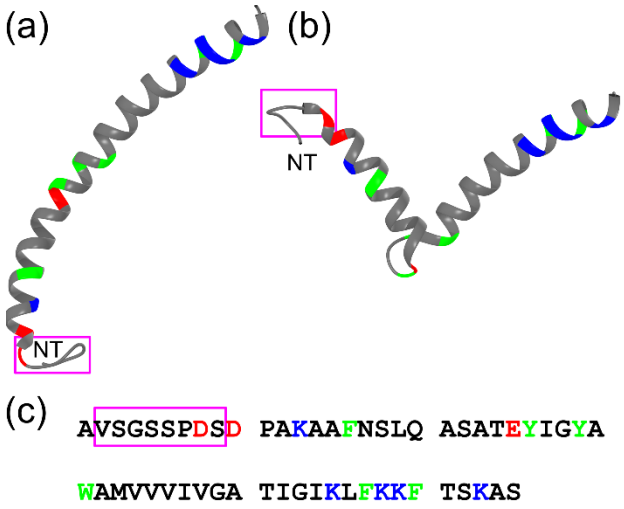

Figure 3- 17. Homology models of M13 with a gold-binding peptide (VSGSSPDS) at the N-termini, NT, (a) pre- and (b) post-chloroform treatment. Both structures share a common sequence, as illustrated in (c). Residues are colored green, red, and blue to identify aromatic, negative, and positive residues, respectively. The gold-binding peptide is boxed in magenta.

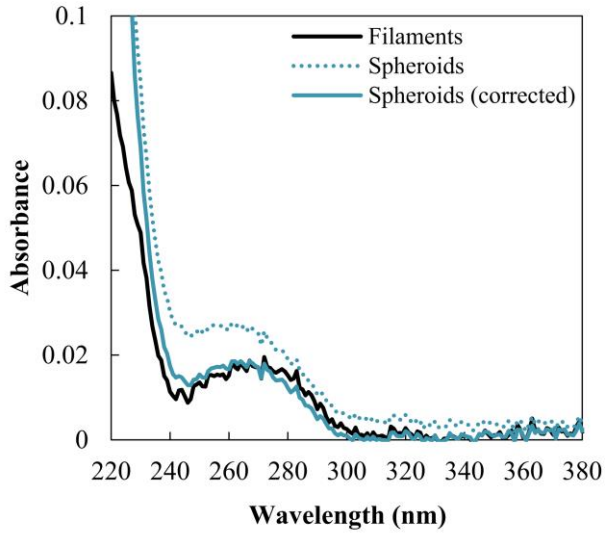

Figure 3- 18. UV-Vis absorbance spectra of gold-binding filaments, spheroids, and Rayleigh scattering-corrected spheroids. On average, the spheroid concentration was 99.8% of the initial filament concentration, indicating that very little viral template was lost during the conversion process.

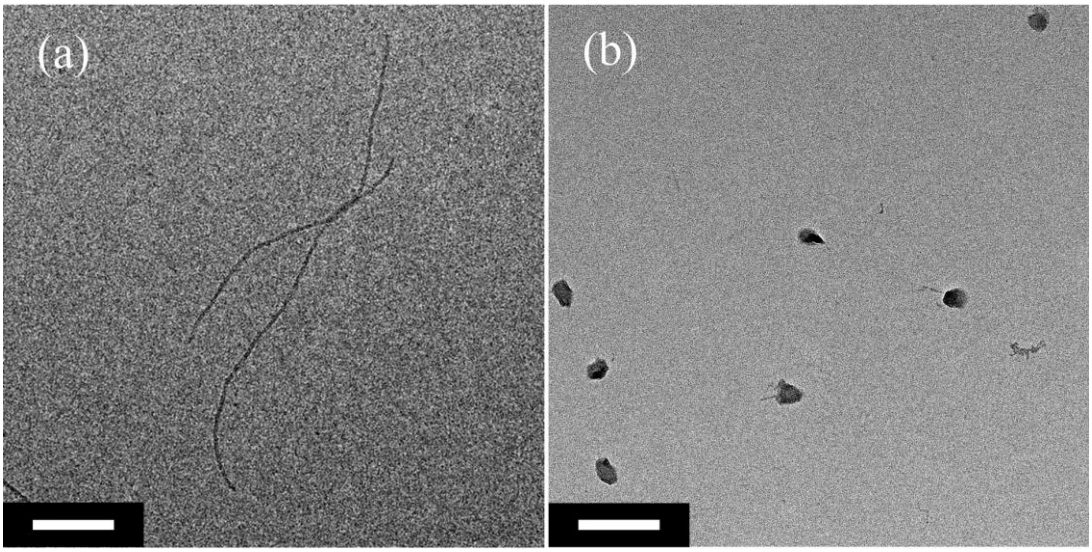

Figure 3- 19. Transmission electron microscopy (TEM) images of gold-binding M13 bacteriophage (a) pre- and (b) post-chloroform treatment (5 cycles). Samples were stained with 0.5% uranyl acetate; scale bar: 200 nm.

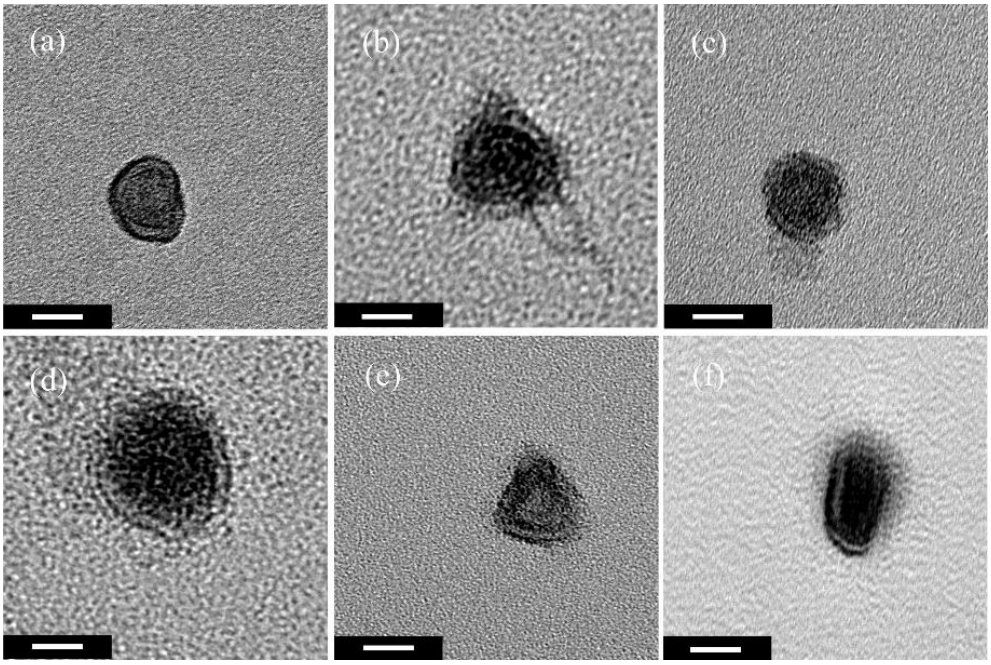

Figure 3- 20. (a-f) High magnification TEM images of gold-binding spheroids after 5 cycles, showing the characteristic shape of chloroform-treated Ff bacteriophage. Samples were stained with 2% uranyl acetate. Scale bar: 20 nm.

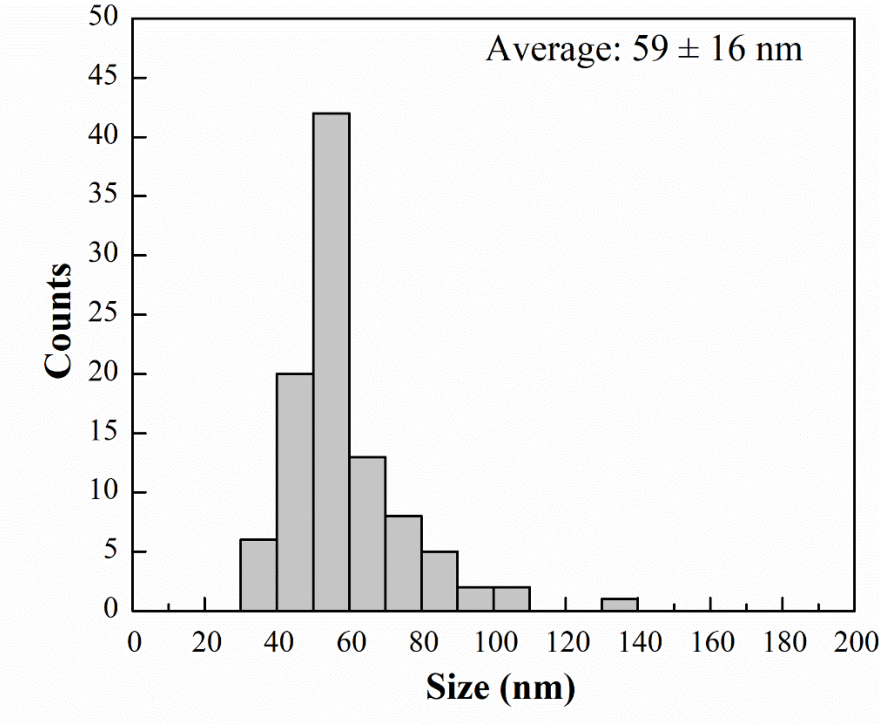

Figure 3- 21. A histogram of the spheroid size distribution following 5 chloroform treatment cycles (N = 100).

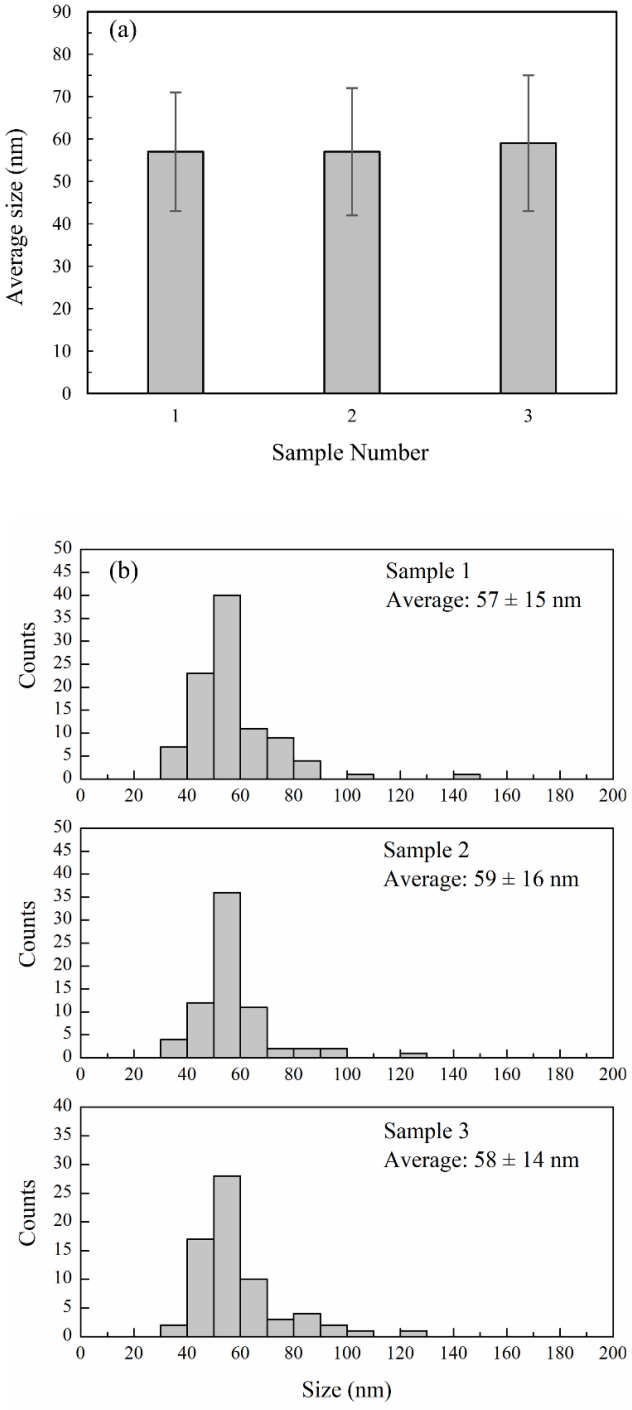

Figure 3- 22. (a) Average sizes and (b) size distributions from three samples of gold-binding spheroids created using a 5 cycle chloroform treatment process.

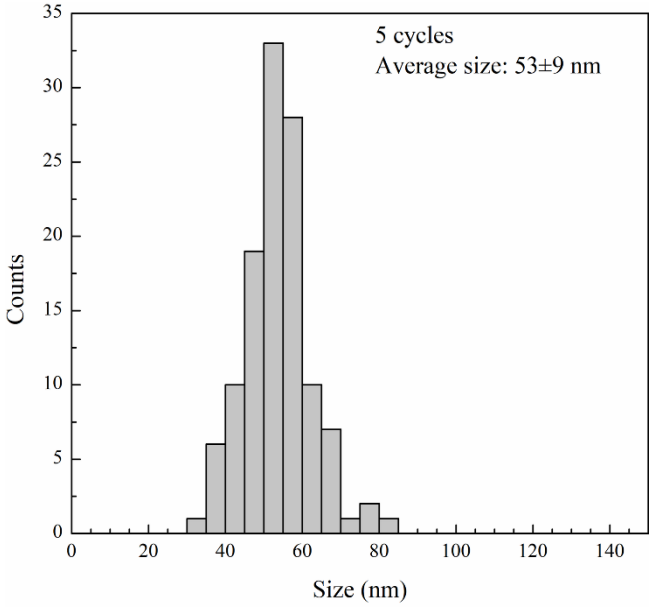

Figure 3- 23. Size distribution of wild-type M13 spheroids following a 5 cycle chloroform treatment process (N = 118).

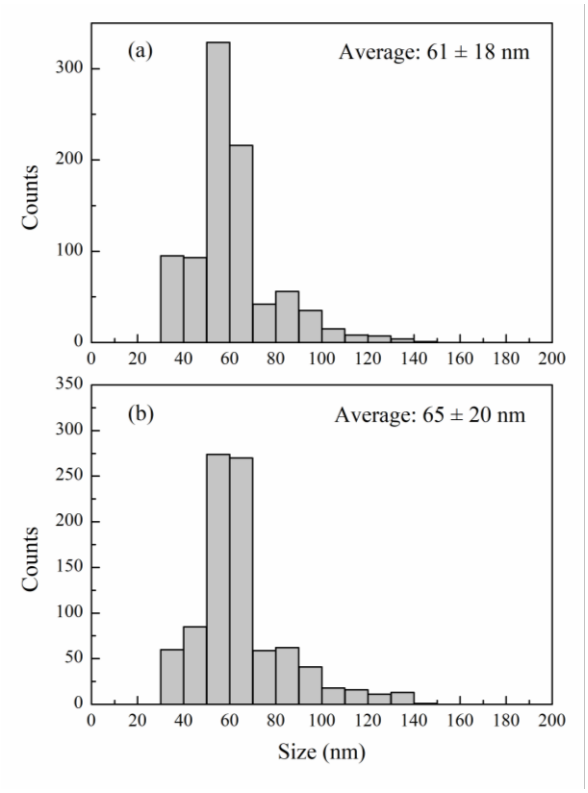

Figure 3- 24. Histograms of spheroid sizes for transformations completed with initial phage concentrations of (a) 5 x 10^8 pfu/µL and (b) 1 x 10^9 pfu/µL (N > 900).

Chapter 4. Gold Binding and Synthesis on Spheroids

4.1 Introduction

There have been no reports of gold binding and synthesis applied to spheroidal forms of M13 bacteriophage. The pVIII proteins will mostly likely have rearranged themselves during the transformation and this may have affected the availability of the gold-binding peptides. This was seen in Petrenko et al where the binding of the insert peptides showed mixed results[127].

In this study, we examine the impact of this shape change on its material assembly capabilities. The gold affinity of the virus was preserved after transformation from filament to spheroid, such that the assembly of gold colloid and synthesis of gold nanostructures were supported. Interestingly, increased gold ion uptake was observed for spheroids as compared to filaments, despite reduced surface area. Moreover, increased nanoparticle density and a distinct spike-like gold morphology were observed for s-forms. This M13 bacteriophage template transformation scheme is believed to be broadly applicable and can be extended to a range of Ff class bacteriophage and nanostructured materials.

4.2 Experimental Details

4.2.1 M13 Transformation

The transformation was performed exactly the same as was described in 3.2.1. The main exception for this transformation was for the sulfo-NHS gold binding. In this case, the phage was prepared at 5.67 x 10^9 pfu/µL over 5 cycles at 10 s/35 s vortex/rest cycles.

4.2.2 Sulfo-NHS Gold Binding

The 2 nm gold nanoparticles Mono-*Sulfo*-NHS-NANOGOLD® reagent (nanoprobes) was dissolved in 200 µL of water. As soon this was completed, wild type phage in PBS was added to the sulfo-NHS gold to a final concentration of 5.67 x 10^9 pfu/µL. The sample is then incubated for an hour at room temperature. The Au/filaments were then transformed as described above. TEM samples were prepared as described below. The number of gold nanoparticles and the interspatial distance between them were counted and measured, respectively, in ImageJ using the watershed tool and the plug-in *nearest neighbor distance calculations*.

4.2.3 Gold Binding on the M13 Phage

The gold-binding functionality of the s-forms was studied with 5 nm colloidal gold solution (5 x 10^{13} particles/mL, BBI Solutions). Equal parts 5 nm diameter gold colloid and 10^8 pfu/µL spheroid solution were combined, briefly vortexed, and allowed to incubate for 10 min prior to transmission electron microscopy (TEM) preparation.

4.2.4 Gold Synthesis on the M13 Phage

Both filamentous and chloroform-treated gold-binding phage were used as templates for gold synthesis. Chloroauric acid ($HAuCl_4$, Sigma Aldrich) was added to 100 µl of 5 x 10^7 pfu/µL phage solution for a final concentration of 250 µM and incubated at room temperature in the dark for an hour. Subsequently, under constant stirring, 50 µL of sodium borohydride ($NaBH_4$, Sigma Aldrich) was added every 30 s to achieve final $NaBH_4$ concentrations of 4.2 µM, 9.4 µM, 31.3 µM and 62.5 µM. Samples were immediately prepared for TEM and ultraviolet-visible (UV-Vis) absorption spectroscopy measurements. For comparison, chloroform-treated, wild-type phage were also used as templates for gold synthesis.

4.2.5 Transmission Electron Microscopy (TEM) Sample Preparation and Characterization

A transmission electron microscope (TEM, Tecnai T12) was used to examine the size and shape of the gold-binding phage before and after transformation, as well as to study its gold binding and synthesis capabilities. For this analysis, a 5 µL sample volume was pipetted onto a formvar/carbon-coated copper grid (Ted Pella, Inc.), incubated for 5 min, rinsed twice with deionized water, and wicked dry with filter paper. Prior to drying, samples without gold were stained with uranyl acetate[111]. ImageJ software was used for TEM image processing and analysis. An ellipse was fitted to each spheroid, and major and minor axes lengths were measured and averaged. A tracing tool was used to accurately select the irregular shape of each templated gold colloid cluster and

synthesized gold nanostructure, an ellipse was fitted to the selected structure, and the major and minor axes length were measured and averaged.

4.2.6 Measurement and Analysis of Gold Ion Adsorption on the M13 Phage

The adsorption of gold ions onto the untransformed and transformed phage was investigated using inductively coupled plasma-mass spectroscopy (ICP-MS, Agilent 7700x). The templates were prepared to a concentration of 10^8 pfu/μL in TBS and $HAuCl_4$ was added to each phage solution at final concentrations ranging from 0 to 500 μM. The solutions were incubated at room temperature in the dark for an hour to ensure sorption equilibrium. A centrifugal filter (Amicon Ultra-0.5, 3 kDa) was used to remove phage and recover the filtrate. Control solutions without phage were also prepared in the same manner. Both filtrate and control solutions were analyzed using ICP-MS. To determine the uptake of the viral templates, the gold ion concentration of the filtrate solution was subtracted from that of the control solution for each $HAuCl_4$ concentration. The maximum adsorption capacity, q_{max}, and the Langmuir constant, a, were determined by fitting the slope-intercept form of the Langmuir isotherm

$$q_e = \frac{q_{max} a C_e}{1 + a C_e}$$

where q_e is the gold concentration adsorbed on the phage at equilibrium and C_e is the concentration of gold at equilibrium.[128–130]

4.2.6 Ultraviolet-Visible (UV-Vis) Spectroscopy

Ultraviolet-visible (UV-Vis) absorption spectroscopy (ThermoFisher, Evolution 60) was used to evaluate the phage concentration before and after transformation, as well as the optical properties of the gold nanomaterial synthesized on filamentous and spheroidal templates. Using a quartz cuvette with a 10 mm optical path length, measurements were made from 220 nm to 380 nm and 400 to 900 nm to determine the phage concentration and optical properties, respectively. The concentration of the filamentous and spheroidal templates were quantified via a previously published protocol.[7] Due to significant geometric change associated with transformation, the absorbance spectra of the spheroids were corrected for Rayleigh scattering as described by Porterfield et al.[112] In brief, a two point approximation of wavelength-dependent scattering (λ^{-4}) was estimated at 340 nm and 360 nm where minimal absorbance was expected from viral proteins and nucleic acids.

4.3 Results and Discussion

4.3.1 Sulfo-NHS Gold Nanoparticles Binding

The wild type phage was used as template to bind sulfo-NHS 2 nm gold nanoparticles as seen in Figure 4-1. Unlike the affinity based templating, this methodology used the two primary amine group on each pVIII protein to bind the gold nanoparticles. With the phage having around 2,700 copies of the pVIII, this meant that for every phage, there were potentially 5400 copies of the pVIII protein. The results indicated that the 2 nm gold nanoparticles remained bound after the transformation process. Using ImageJ (Figure 4-1 (b) and (c)), an average of 226 gold nanoparticles

were counted per spheroids with an average distance between neighboring particles at 1.5 ± 0.8 nm. As it can be seen, no pattern were discernable on the spheroids. Overall, this showed that the primary amine groups were available for binding. However, the low count of nanoparticles per spheroids may be attributed to several factors: the number of nanoparticles is undercounted due to the two dimensional image, the loss of protein during the transformation process or though unlikely due to the nature of the covalent bond, the gold nanoparticles ripped themselves off the template.

4.3.2 Gold Nanoparticle Binding to VSGSSPDS Phage

The peptide, VSGSSPDS, has demonstrated affinity for gold when incorporated as a pVIII insert within the filamentous M13 bacteriophage.[53] Yet, because the affinity of displayed peptides can be dependent on peptide-protein interactions along the phage body[109], the binding capabilities of the VSGSSPDS pVIII peptide fusion were examined following chloroform treatment. As such, s-forms were incubated with 5 nm colloidal gold solution. As shown in the low magnification TEM image in Figure. 4-2 (a), following incubation, both small groups and larger clusters of colloid were observed. While the smaller groups of nanoparticles were attributed to reduced electrostatic repulsion caused by the introduction of buffer salts with the template, histograms of gold colloid assembly size (Figure 4-3) with and without spheroids confirmed the larger clusters (>60 nm) were strictly associated with the presence of the template.

Higher magnification TEM images of a spheroidal viral template and a large colloidal nanoparticle cluster are shown in Fig. 4-2 (b) and (c), respectively. The relative size and

geometry of the template and cluster further supported the decoration of spheroids with gold nanoparticles. Additionally, samples stained with uranyl acetate (Figure 4-4) definitively demonstrated co-location of s-forms and nanoparticle clusters. Repeatability of the formation of gold clusters through binding was demonstrated across samples (Figure 4-5).

The colloidal nanoparticles were closely-packed and randomly arranged on the surface of the viral template. Because the positions of the gold-binding peptides on the M13 spheroid surface were likely densely packed without long range organization, we believe that a one-to-one peptide-to-nanoparticle binding ratio was prevented and relative disorder promoted. A 24 nm redshift in peak optical absorbance, as shown in Figure 4-6, corroborated the close proximity of the bound nanoparticles on the viral templates. Despite the estimated 15-fold one-dimensional contraction and the nearly 1.8-fold surface area reduction associated with spheroid formation, the gold-binding peptide clearly retained an affinity for gold after chloroform treatment.

4.3.3 Gold Mineralization on VSGSSPDS Phage

To further probe gold-binding characteristics and explore the effects of the viral protein coat conformational change on mineralization, gold synthesis was completed with both spheroidal and filamentous M13 templates. Gold-binding templates were incubated in 250 μM $HAuCl_4$ with a pH near 6.7 for 1 hour. Despite the partial loss of helicity and reduced intermolecular π-π interaction associated with transformation, the s-forms remained stable at these slightly acidic conditions. $NaBH_4$ was then added step-wise 4

times, ultimately achieving a concentration of 62.5 μM. Representative synthesis products are shown for each step-wise addition in Fig. 4-7. At the lowest $NaBH_4$ concentration, 4.2 μM, only gold ions (no nanoparticles) were observed bound to the spheroidal viral template. With subsequent $NaBH_4$ additions, 9.4 to 31.3 μM, the progressive reduction of gold ions produced several discrete nanoparticles which then grew in size. Spheroid-templated gold synthesis products stained with uranyl acetate confirmed particle clusters were associated with viral proteins (Figure 4-8). At the highest $NaBH_4$ concentration, 62.5 μM, fused nanostructures with an average size of 86 ± 27 nm were produced on the template. While nanoparticles formed at lower $NaBH_4$ concentrations were relatively isotropic, as gold reduction advanced with step-wise $NaBH_4$ additions, highly anisotropic spike-like features also developed resulting in a range of morphologies (Figure 4-9) and wide size distribution (Figure 4-10). To better elucidate the effect of the gold-binding spheroid on the formation of the spike-like structures, gold synthesis was performed without a viral template (Fig. 4-11) and in the presence of wild-type spheroids (Fig. 4-12) using a $NaBH_4$ concentration of 62.5 μM. Neither condition resulted in protruding, highly anisotropic features. Without a viral template, the average size of the synthesis products was only 10.2 ± 3.9 nm, while little to no nanoparticle growth was observed on the wild-type spheroids.

As shown in Figure 4-7, like the spheroids, at the lowest $NaBH_4$ concentration, the filaments only showed evidence of gold ion binding and no nanoparticle growth. The step-wise reduction of gold ions yielded distinct gold nanoparticles which enlarged with each $NaBH_4$ addition eventually fusing with neighboring nanoparticles in some locations

to form either (1) low aspect ratio ensembles with an average size of 38.2 ± 13.1 nm or (2) high aspect ratio chains with an average length and width of 71.1 ± 26.9 nm and 23.6 ± 6.1 nm, respectively. In contrast to the spheroid-templated nanostructures, prior to coalescence, the filament-templated nanoparticles remained fairly isotropic in structure with an average size of 5.8 ± 1.2 nm at 9.4 μM $NaBH_4$. Although the same gold synthesis conditions were used for both the M13 gold-binding spheroids and filaments, very different morphologies were produced.

The UV-Vis absorbance spectra of the highest $NaBH_4$ concentration synthesis products were measured and are shown in Figure 4-13. Localized surface plasmon resonance (LSPR) was observed for both viral-templated materials. Among other parameters, LSPR absorption characteristics are controlled by nanoparticle size, shape, environment, and particle-particle optical coupling. The optical absorbance of the spheroid-templated gold produced a broad, feature ranging from 500 nm to 900 nm with a maximum absorbance near 700 nm. This optical signature was consistent with the broad size distribution of the templated nanocrystalline, spiky gold nanostructures 86 ± 27 nm in size.[71,131–133] In contrast, filament-templated gold displayed an asymmetric, but well-defined absorbance peak centered at 556 nm with a long wavelength tail extending beyond 900 nm. Such optical behavior was attributed to the combination of gold nanoparticle ensembles and chains synthesized on the filament and was in agreement with previous reports.[134–138] The dissimilar spectra of the two templates was a direct consequence of the disparate morphologies of the spheroid- and filament-templated synthesis products.

Gold ion uptake, one potential source of the observed morphology difference between gold templated on spheroidal and filamentous templates, was investigated using ICP-MS. The equilibrium adsorption concentration plotted against gold ion concentration for both template geometries is shown in Figure 4-14, along with corresponding Langmuir isotherm curve. Langmuir fit parameters, q_{max} and a, are found in Table 4-1. Maximum gold ion adsorption capacities of 2.7 x 10^{-5} mol/mg and 4.3 x 10^{-5} mol/mg were calculated for filaments and spheroids, respectively.

Table 4- 1. **.** Equilibrium Coefficients of Langmuir Adsorption Isotherm

Template	**q_{max} (mol mg^{-1})**	**a (L mol^{-1})**	**R^2**
Filament	2.7 x 10^{-5}	8782	0.994
Spheroid	4.3 x 10^{-5}	8509	0.996

The gold ion uptake for the spheroids was 1.6 times more than for the filaments, indicating a higher apparent affinity for gold. Assuming an equivalent number of gold-binding peptides were displayed on both M13 geometries, the peptide surface density was estimated to be 1.8 times larger for spheroids than filaments. This significant difference in gold-binding peptide areal density was likely responsible for the increased avidity and the ion adsorption capacity of the s-form. In addition, it may have had an important effect on nanostructure shape and size. The impact of increased localized peptide density caused by small peptide aggregates or clusters has been reported for PbSe[139] and Cu[140] nanoparticles synthesized on peptide nanotubes. In the former, peptide aggregation converted nanoparticle shape from cubes to rods. In the latter, peptide aggregation

controlled Cu nanoparticle diameter and polydispersity. Furthermore, long range peptide packing density has also demonstrated influence over morphology. Peptide-templated gold nanoparticles synthesized at the air-water interface of a Langmuir trough showed morphologies ranging from triangle plates to star-like structure depending on peptide packing density.[141] In the present studies, increased gold ion uptake due to greater peptide surface density associated with the spheroidal templates is believed to have contributed to increased nanoparticle density and the formation of spike-like features.

4.4 Conclusions

Gold nanostructures on spheroids were successfully created through various means. Wild type M13 bacteriophage retained the covalently bound 2 nm gold nanoparticles bound to the major coat protein post transformation. Gold-binding M13 spheroids were found to retain affinity for gold, demonstrating the ability to bind pre-formed colloidal gold nanoparticles as well as to direct gold synthesis. It was noted that the morphology of the synthesized gold nanostructures was dependent on the template geometry. Gold-binding M13 filaments yielded a mixture of isolated gold particle ensembles and chains composed of relatively isotropic nanoparticles while M13 spheroids produced nanostructures with anisotropic, spike-shaped features. The gold ion adsorption of spheroids was determined to be greater than that of filaments. We believe that this disparity contributed to the observed template-dependent gold morphological differences. The lower surface area of the spheroids likely increased surface packing of gold-binding peptides and lead to enhanced gold avidity. Further investigation is needed

to better understand the density and organization of gold-binding peptides on the surface of the spheroid. Nonetheless, it is interesting to consider the potential of this scaffold to control gold morphology by modifying peptide surface density through genetic display or chemical conjugation. Furthermore, the promise and utility of the spheroidal template could be extended to other inorganic material systems via simple substitution of the displayed peptide. With the confirmation of the gold binding on the spheroidal template, the Au/spheroids is ready to be studied as a photothermal bactericidal agent.

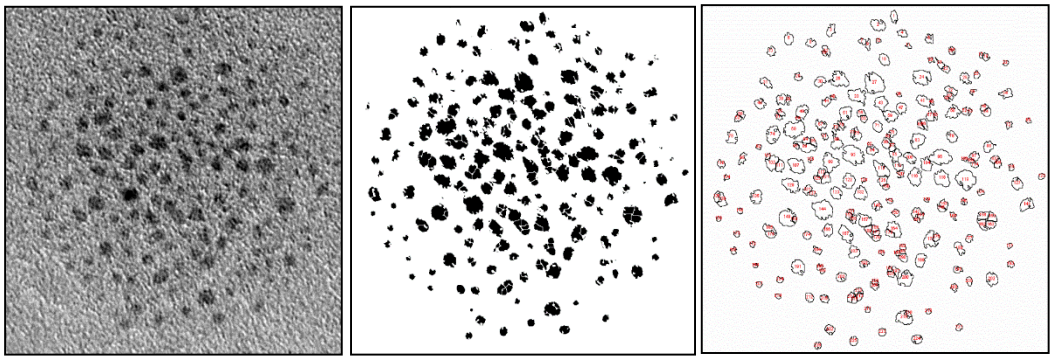

Figure 4- 1. (a) Covalently bonded gold nanoparticles (b) ImageJ watershed tool and (c) ImageJ counter and interspacing calculator

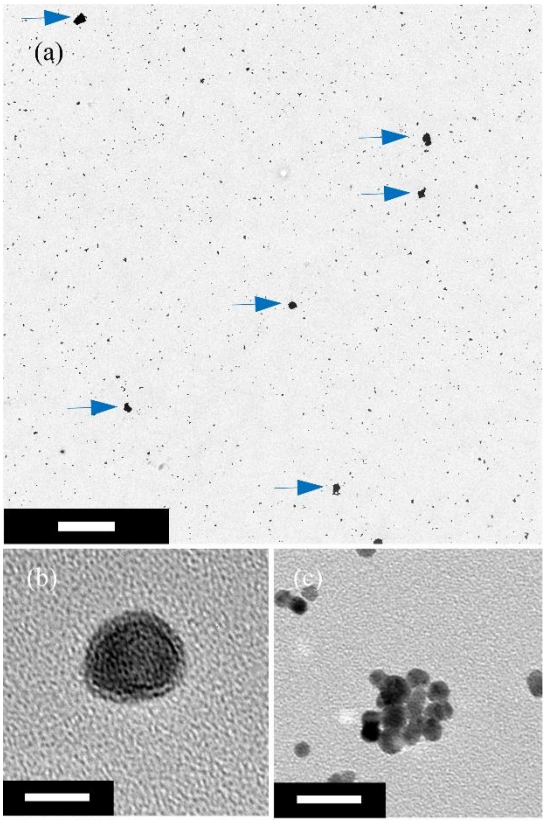

Figure 4- 2. (a) TEM image of several spheroid-templated gold colloid clusters with excess unbound colloid; scale bar: 500 nm. Templated nanostructures are indicated by arrows. An individual gold-binding spheroid (b) without and (c) with 5 nm colloidal gold nanoparticles arranged on the surface to form a cluster; scale bar: 20 nm.

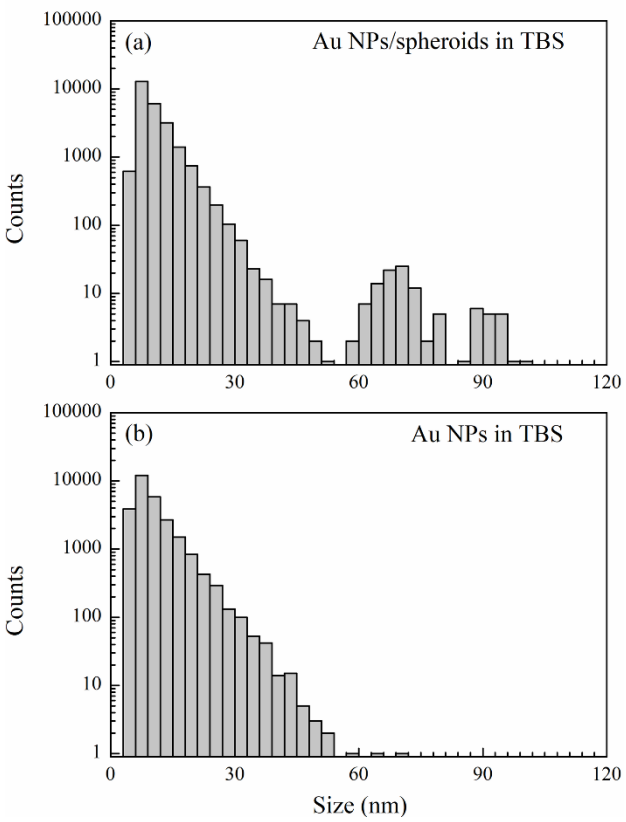

Figure 4- 3. Histograms of gold colloid assembly size when prepared in dilute TBS (a) with (N = 11600) and (b) without gold-binding M13 spheroids (N = 27900).

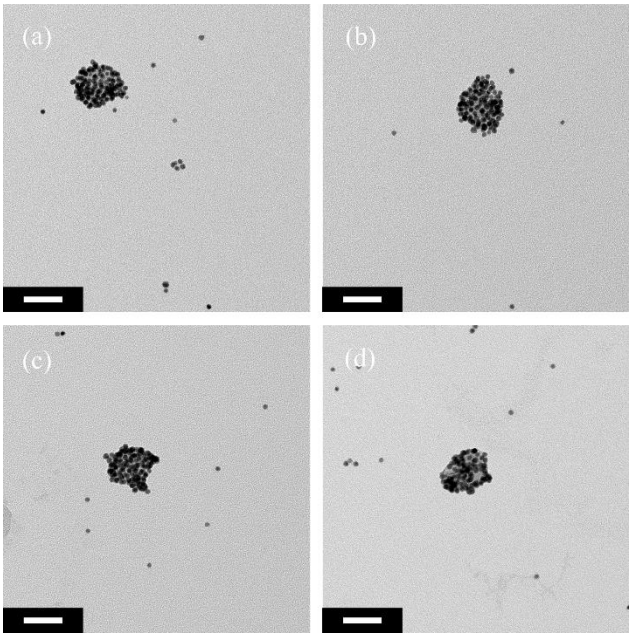

Figure 4- 4. (a-d) TEM images of 5 nm gold nanoparticles assembled on gold-binding spheroids. Samples were stained with 2% uranyl acetate to show spatial correlation between gold nanoparticle clusters and M13 spheroidal template. Scale bar: 50 nm.

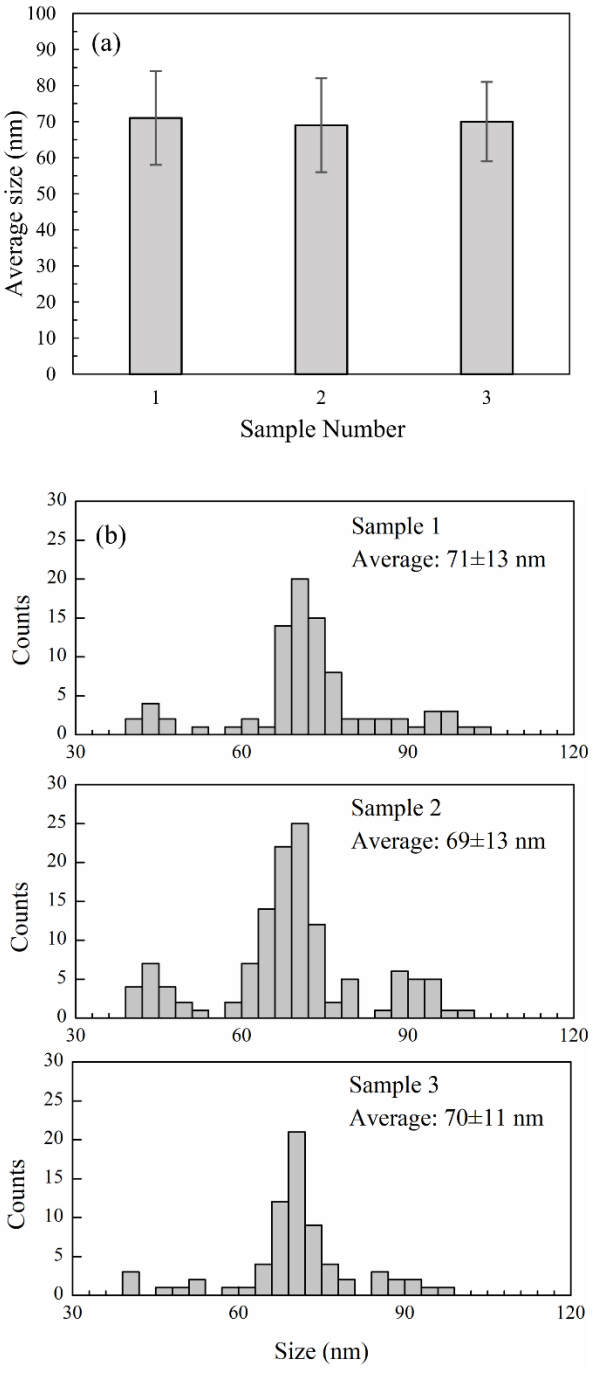

Figure 4- 5. (a) Average sizes and (b) size distributions from three samples of gold-binding spheroids decorated with gold nanoparticles ($N \geq 70$).

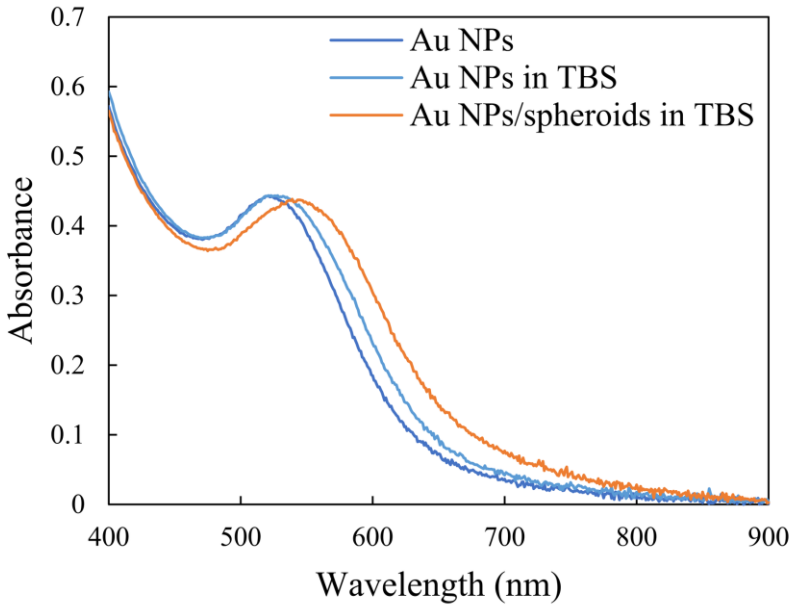

Figure 4- 6. UV-Vis absorbance spectra of as-received gold colloid, and gold colloid assemblies prepared in dilute TBS with and without gold-binding M13 spheroids.

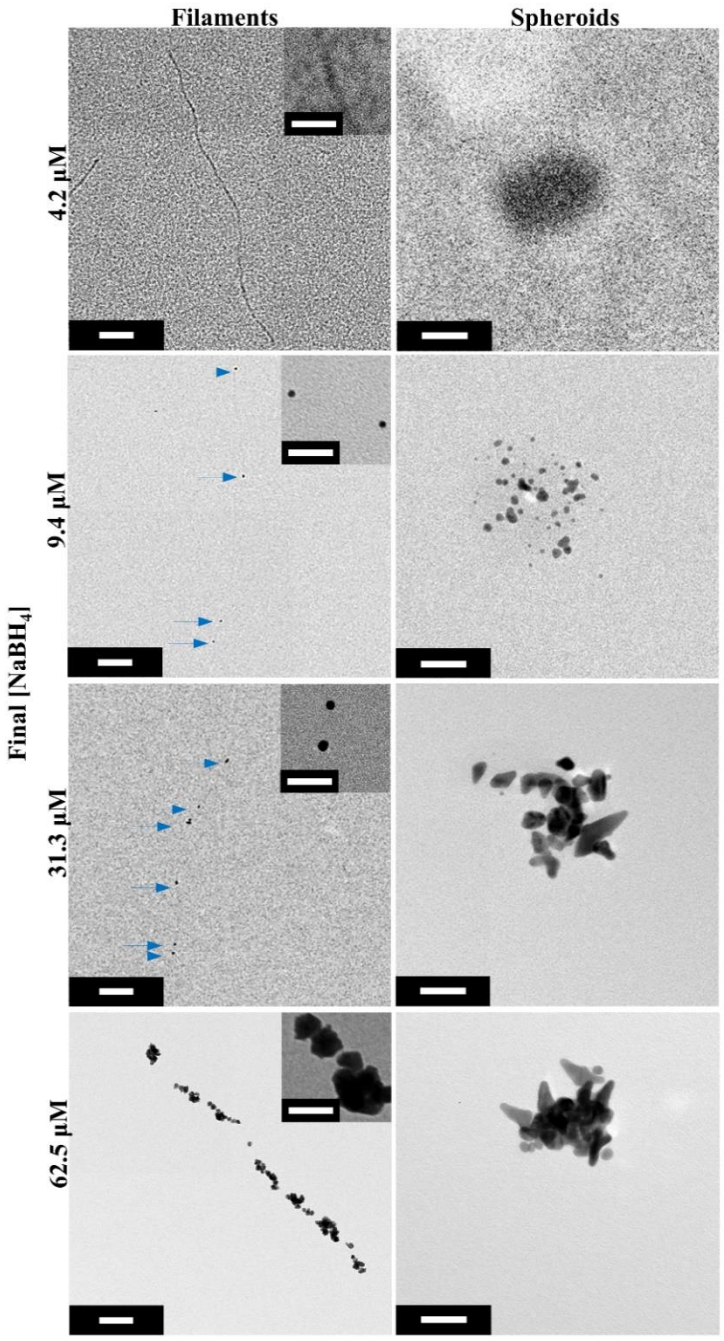

Figure 4- 7.Comparison of gold nanomaterials synthesized on filamentous (scale bar: 100 nm) and spheroidal templates (scale bar: 25 nm) following the addition of $NaBH_4$ at different concentrations. High magnification images of filament-templated materials are shown within the insets (scale bar: 25 nm).

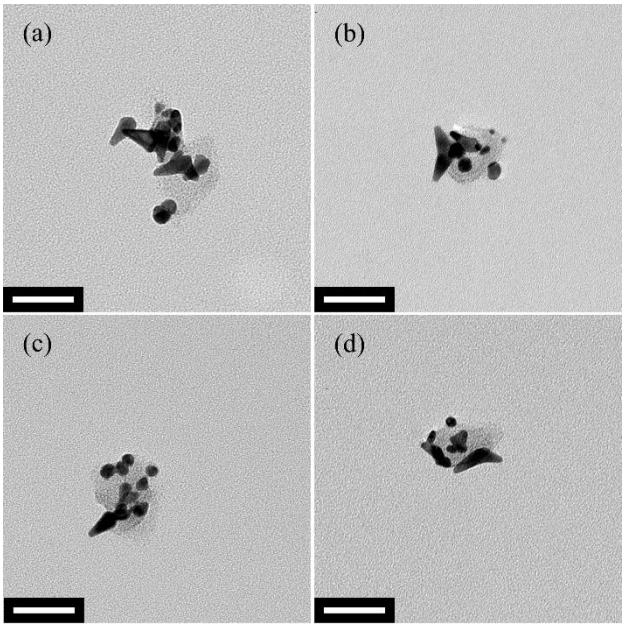

Figure 4- 8. (a-d) TEM images of gold-binding spheroid-templated gold synthesis products formed using a final $NaBH_4$ concentration of 31.3 µM. Samples were stained with 2% uranyl acetate such that viral proteins associated with the gold structures can be seen. Scale bar: 50 nm.

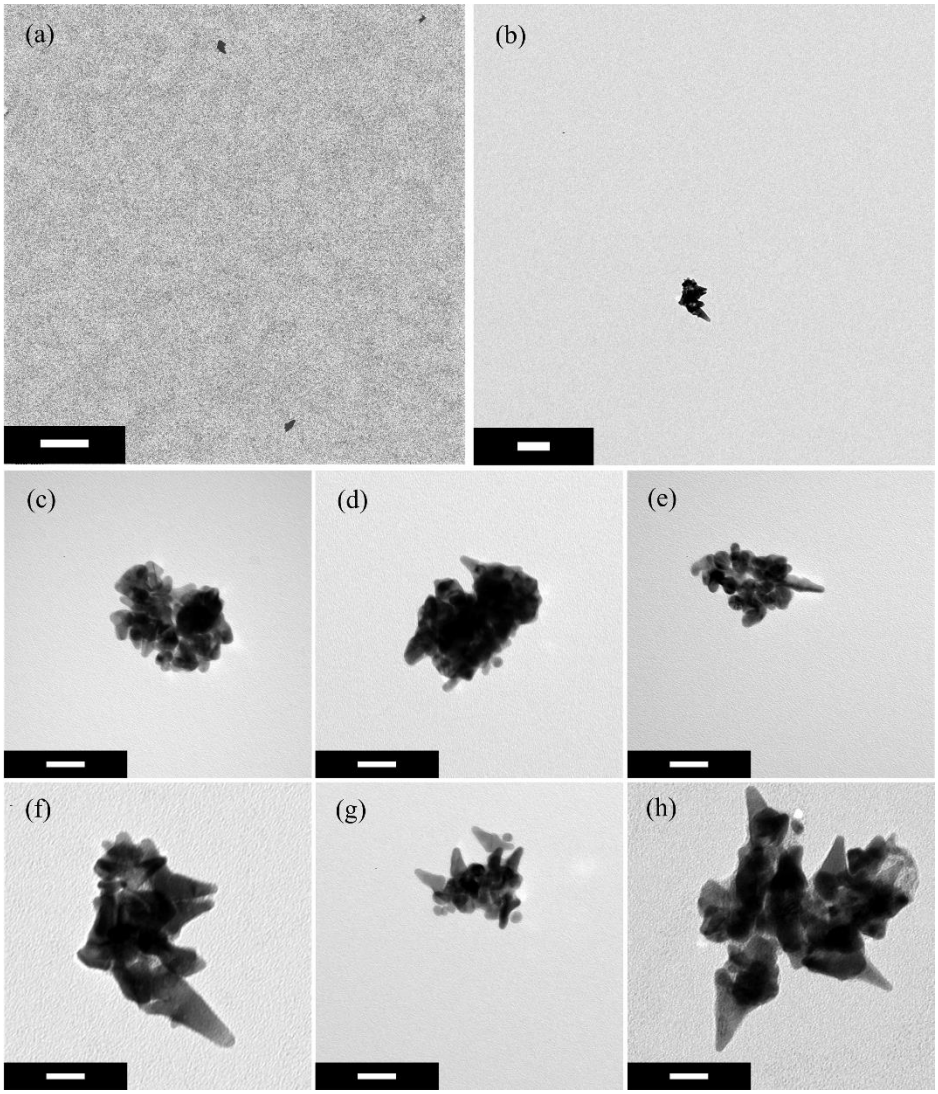

Figure 4- 9. TEM images of gold synthesis products formed in the presence of gold-binding spheroids using a final $NaBH_4$ concentration of 62.5 µM. (a) scale bar: 500 nm; (b) scale bar: 100 nm; (c-h) scale bar: 20 nm. A variety of spike-like morphologies were found on the spheroids producing a broad range of gold nanostructure sizes. Homogenous nucleation of gold unassociated with the template was not observed.

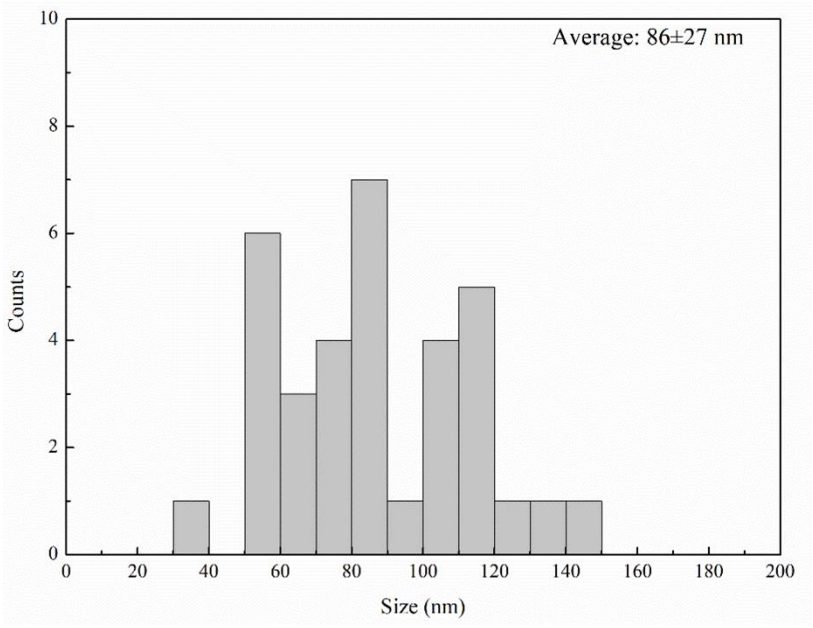

Figure 4- 10. Size distribution of the synthesized gold nanostructures on gold-binding spheroid templates using a final $NaBH_4$ concentration of 62.5 µM (N = 35).

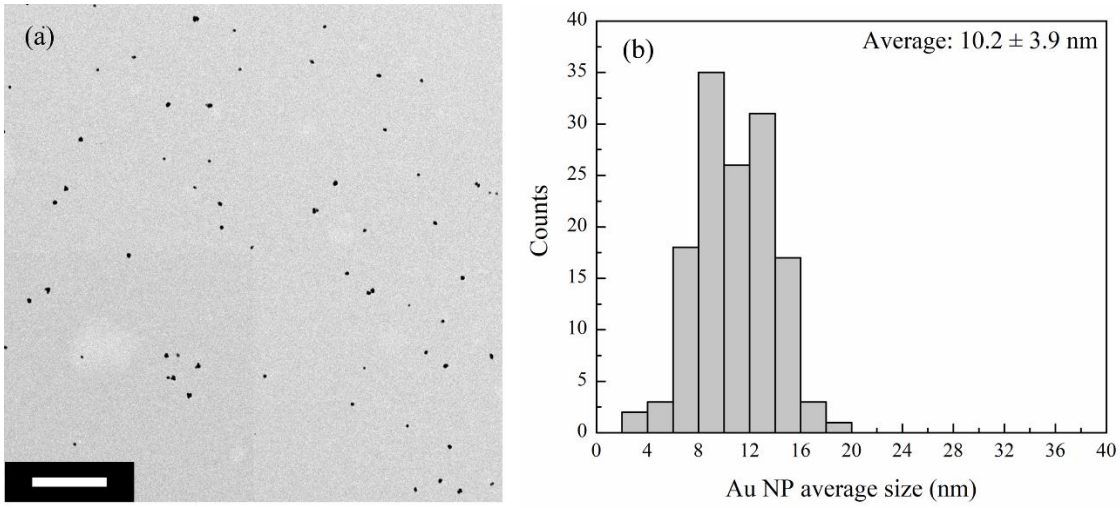

Figure 4- 11. (a) TEM image and (b) histogram of particle sizes for synthesis products formed without a gold-binding spheroidal viral template using a final $NaBH_4$ concentration of 62.5 µM (N = 136); scale bar: 200 nm.

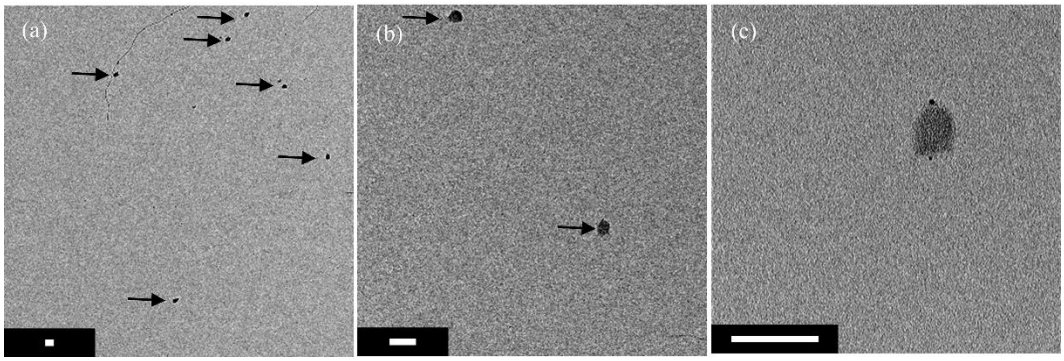

Figure 4- 12. (a-c) TEM images of gold synthesis products formed in the presence of wild-type spheroids using a final $NaBH_4$ concentration of 62.5 µM. Samples were stained with 2% uranyl acetate. Black arrows in lower magnification images indicate wild-type spheroids. Scale bar: 100 nm.

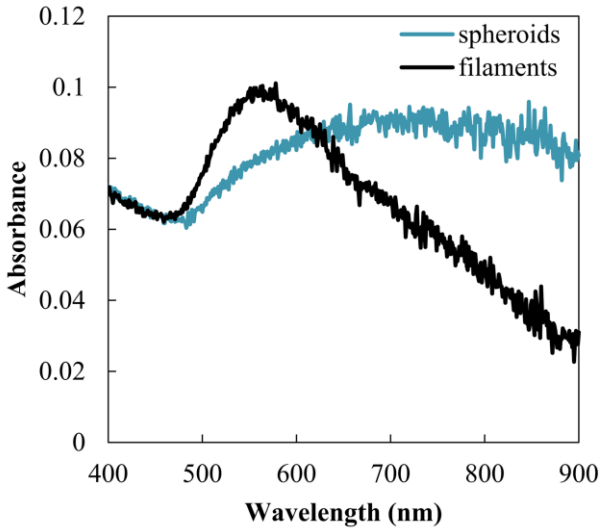

Figure 4- 13. UV-Vis absorbance spectra of gold synthesis products on filamentous and spheroidal templates using a final $NaBH_4$ concentration of 62.5 µM.

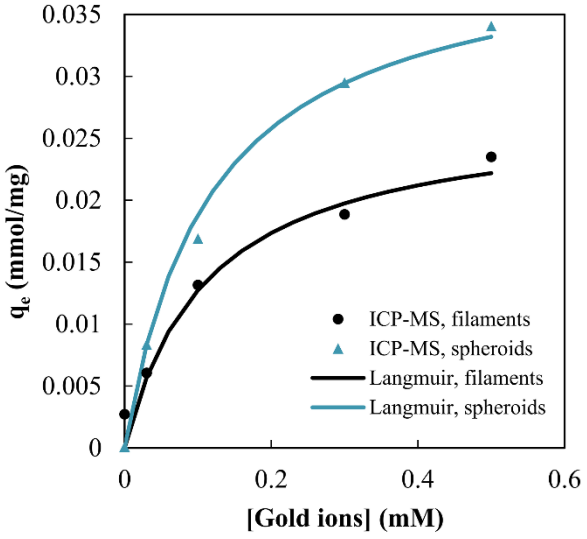

Figure 4- 14. Adsorption isotherm of gold ions onto the M13 spheroids and filaments

Chapter 5. Photothermal Effect of Au-templated Spheroids and I-forms

5.1 Introduction

With the advance of multidrug resistant (MDR) bacteria, antibiotics are losing their potency. *Staphylococcus aureus, E. coli* and *Pseudomonas aeruginosa* are a few examples of known pathogens that have developed antibiotic resistance through genetic mutations.[142–144] Therefore, development of novel long-term approaches to combat pathogenic microbial cells are necessary. Photoinduced inactivation of the bacterial infections has proven to be a promising pathway, as the method is immune to development of antibiotic resistance.[145] The light absorbing nanoparticles conjugated with antibodies are first delivered to the target and irradiated under a suitable wavelength of light. Light absorbed by the nanoparticles oscillates the free electrons in the nanoparticles and the energy is transferred to the gold nanoparticle lattice, and the heat is transferred to the surrounding pathogenic microbial cells via phonon-phonon interactions[70], which permanently damages the cells membranes. Gold nanoparticles (Au NPs) in particular have been successfully utilized as photoabsorbing agents.[76] The particles are non-toxic, chemically inert and tunable to wide wavelength range.[146,147] Mocan et al covalently linked spherical Au NPs with IgG antibody to target Methicillin-resistant *S. aureus*.[148] The killing rate of 88.2% was achieved after 30 min under 808 nm

laser exposure. Moreover, rod shaped Au NPs were covalently conjugated to antibodies to attach to Pseudomonas aeruginosa.[74] The NIR irradiation to 785 nm laser eliminated 75% of the pathogens after 10 min at 50 mW. Thermal based laser-treatment of the MDR bacteria with Au NPs is a highly potent, non-invasive method that circumvents recurrence of the pathogens. However, there are challenges presented by antibody development for targeting MDR bacteria. Production of specific antibodies requires animal models making the process cost inefficient and time-consuming[84]. Here, we present a new technique of anchoring to bacterial cells for photothermal ablation of Gram negative *E. coli* using geometrically modified M13 bacteriophage nano-scaffolds.

The rationale in utilizing M13 bacteriophage as a photothermal bactericide lies in the opportunity to leverage the exceptional capabilities of the virus, such as an innate targeting of *E. coli*, programmable major and minor coat proteins, low-cost and large-scale production ability. A major key of using the phage as a bactericidal template is its ability to target *E. coli*. In the case of the filamentous phage, the infection pathway is highly dependent on the interaction of the pIII protein and the F-pilus of the *E. coli.*[15,149–151] The F-pili are a hair-like appendage of *E.* coli, which is used for horizontal gene transfer.[152] These F-pili play a major role in the infection process of the M13 bacteriophage. The infection process is initiated when the N2 domain of the pIII comes into contact and binds with the tip of the F-pili.[14,15] Following this, the F-pili retracts, bringing the phage to the *E. coli* membrane to infect it. Binding to the F-pili also makes the pIII protein undergo a conformational change in order for the N1 domain to interact with the ToIA binding site and trigger the infection process.[16] The bacteriophage,

however, is not limited to targeting its *E. coli*: the pIII has been modified to target other bacteria such as *S. aureus* for bacterial detection and imaging.[153]

The geometry of the M13 bacteriophage is not ideal as photothermal bactericidal platform. The long, filamentous structure may only allow small numbers of gold nanoparticles situated near the pIII to come into contact with the *E. coli* membrane. To circumvent this, The unusual property of viral geometry contraction from the filamentous shape to the rod and spheroids via chloroform interaction is leveraged to create more suitable templates.[23,24,28] The chloroform environment mimics the hydrophobic nature of the *E. coli* membrane that triggers reorganization of the proteins.[24] At low-temperatures filaments are frozen at a metastable state of the contraction and protein rearrangement prior to the filament turning into a spheroid.[24] S-forms are filaments that further progressed in contraction that was accelerated by room temperature, as opposed to the temperature of 0 ℃ for i-forms.[24,106,154] These i-forms and s-forms have been shown to no longer be infectious post transformation.[23,24,106]. This property makes it useful to ensure the genes in the templates are not transferable to the targeted bacteria.

A material of interest for photothermal bactericide is gold and the M13 bacteriophage has been shown to both bind and synthesize gold on its coat protein.[44,49–54] A gold-binding phage has been successfully transformed to spheroids and shown to retain its gold binding properties post transformation.[155]

Yet, there are major caveats in using the filamentous form of the virus. The morphology of filamentous virus limits the contact area between photoactive

nanoparticles and the *E. coli*. Only the nanoparticles in proximity to the pIII proteins would be adjacent to the membrane, which template, three major criteria have to be met: a compact shape to maximize the number of particles in contact with the *E. coli*'s membrane, an inactive bacteriophage and the targeting capabilities of the pIII proteins at the end of the template. To meet these criteria, we fully utilize potentially reduces the efficacy of the system. Furthermore, the filamentous phage remains infectious. As such, to create an effective bactericidal rod-like and spheroidal morphologies of the M13 bacteriophage. These structures are significantly smaller than the filamentous form and non-infectious[23,24,106]. In this study, we investigate the two different forms of the M13 bacteriophage: rod-like (the aforementioned i-forms) and spheroids (s-forms) as an *E. coli* targeting template.

5.2 Experimental Details

5.2.1 M13 Transformation

An M13 bacteriophage with a gold-binding peptide, VSGSSPDS[53], displayed on each of approximately 2700 copies of the pVIII major coat protein found along the viral length was selected and studied as a scaffold for photothermal antibacterial agents. The gold-binding phage was transformed from its filamentous form to its spheroidal form (s-form) as previously described.[156] Briefly, the phage was dispersed in 100 µL tris-buffered saline (TBS, 5 mM Tris-HCl, 150 mM NaCl, pH 7.5) at a concentration of 108 pfu/µL and vortexed with an equal volume of chloroform (99.8%, ACROS Organics) for 5 vortex/rest (2 s /13 s) cycles at room temperature. Post transformation, 95 µL of the

chloroform was removed and air was gently blown over the sample for 15 s to ensure removal of residual chloroform. M13 filaments were transformed to rms) using a similar approach at reduced temperature. [157, 28] Prior to mixing, phage and chloroform solutions were allowed to cool to 0°C over a period of 2 min. The phage/chloroform suspension was then vortexed at 0°C for 5 vortex/rest (8 s/ 5 s) cycles at low power and chloroform was removed.

5.2.2 Gold Binding on the M13 Phage

To assemble Au/i-form and Au/s-form bactericidal nanostructures, transformed viral templates were decorated with Au nanoparticles (NPs). Equal volumes of Au colloid (5×10^{10} particles/μL, BBI Solutions) and viral templates (10^8 pfu/μL) were gently vortexed, incubated for 10 min at 4°C, and used immediately.

5.2.3 Bactericidal activity of viral-templated gold nanostructures

The effectiveness of Au/i-form and Au/s-form nanostructures as photothermal antibacterial agents was evaluated using the ER2738 strain of Escherichia coli (E. coli) K12 as a model system. ER2738 is a host strain compatible with the native filamentous form of the M13. A culture of E. coli K12 ER2738 was grown on a shaking incubator at 350 rpm in lysogeny broth (LB broth, Lennox, Fisher BioReagents) with 20 mg/mL tetracycline (TET HCl, Tetracycline hydrochloride, Genlantis) at 37°C for 5 to 6 h or to mid-log phase. The optical density was measured at 600 nm and the E. coli cell concentration was diluted to 2×10^4 cells/μL .

A 2.5 μL volume of E. coli was added to 25 μL of a viral templates (i-form or s-form) and viral-templated gold nanostructures (Au/i-form or Au/s-form) for a final volume of 27.5 μL or to a final concentration of 4.5 x 10^7 pfu/μL of the structures. Duplicate solutions were made for each viral-templated gold nanostructure. The solutions were incubated for 90 min at 4°C in the dark to allow F-pili binding to the bactericidal agents. Subsequently, one of each of the duplicate mixtures was transferred to an open polymerase chain reaction (PCR) tube and exposed to continuous wave 532 nm laser (Horiba LabRam/AIST-NT AFM) illumination. Both illuminated and unilluminated solutions were diluted to ~ 4 x 10^2 cells in LB broth, plated on agar, and incubated at 37°C for 14 h. Bacteria colonies were counted, and E. coli viability (%) for both Au/i-forms and Au/s-forms was calculated by normalizing the number of illuminated to unilluminated colonies for each nanostructure. The effect of a range of laser powers (0, 20, 40, and 60 mW) with a spot size of 0.2 cm^2 and illumination times (0, 5, 12, and 20 min) on cell viability was explored. To ensure that the viral-templated gold nanostructures and their nanoscale building blocks were not fundamentally detrimental to E. coli (irrespective of 532 nm laser exposure), viability was also determined for unilluminated control solutions of ER2738 incubated with Au/i-forms, Au/s-forms, i-forms, s-forms, and gold colloid. Experiments were repeated in triplicate.

5.2.4 Transmission Electron Microscopy

Transmission electron microscopy (TEM, Tecnai 12) was used to characterize the shape and dimensions of transformed viral templates, as well as i-form and s-form ability to bind E. coli F-pili before and after incubation with Au NPs. In addition, electron

microscopy was used to image Au/i-forms and Au/s-forms on the E. coli surface. For these studies, 5 μL of sample was pipetted onto a formvar/carbon-coated copper grid (Ted Pella, Inc.) and incubated for 5 min. The grids were then rinsed twice with deionized water, stained with 2% uranyl acetate for 30 s, and wicked dry with filter paper. TEM images of the samples were analyzed using ImageJ software. A segmented line function was used to measure the length and width of the templates. Structures with an aspect ratio between 3 and 25 with lengths between 80 and 300 nm were defined as i-forms.

5.2.5 UV-vis spectroscopy

Optical absorbance spectroscopy (Evolution 60, ThermoFisher) was used to measure M13 bacteriophage and E. coli K12 ER2738 concentrations, in addition to the absorbance spectra of the 5 nm Au NPs, Au/i-forms, and Au/s-forms. The Au colloid (5 x 10^{10} particles/μL, BBI Solutions) and tris-buffered saline (TBS, 5 mM Tris-HCl, 150 mM NaCl, pH 7.5) were diluted in 1:1 ratio to a final concentration of 2.5 x 10^{10} particles/μL for the Au NPs spectra. The viral-templated gold nanostructures were prepared as described above and measured immediately after 10 min incubation at 4^{o}C. The absorbance of Au NPs and viral-templated gold nanostructures were measured from 200 to 1100 nm using a quartz cuvette with a 10 mm optical pathlength. OD269 and OD600 were used to measure the concentrations of filamentous phage and bacteria, respectively, via a previously published procedures[158].

5.3 Results and discussion

A schematic overview of Au/i-form and Au/s-form bactericidal nanostructure assembly, *E. coli* targeting, and subsequent killing of the bacteria via photothermal lysis is shown Figure 5-1. Brief chloroform exposure was used to convert the native filamentous form of the M13 gold-binding bacteriophage to i-forms and s-forms. The transformation temperature dictated the template geometry, with low temperature (0°C) and room temperature processes yielding rods and spheroids, respectively. Due to the thousands of gold-binding peptide fusions displayed on coat proteins, viral-templated gold nanostructures were created by the simple addition of 5 nm gold nanoparticles to the transformed phage solution. These inactive, gold-decorated, morphologically-transformed phage successfully targeted *E. coli* through F-pili binding. Retraction of F-pili assisted delivery of bactericidal nanostructures to the cell surface. Once these gold clusters were adjacent to the cell membrane, 532 nm laser illumination was used to photothermally kill the *E. coli*.

Geometrically-transformed, gold-binding M13 bacteriophage were studied with transmission electron microscopy (TEM) as templates for bactericidal nanostructures. The distinctive morphologies of the M13 i-form and s-form are shown in Figure 5-2. As reported, these filamentous bacteriophage have an average length of 921 ± xxx nm.[156] Viral length is dependent on the size of the enclosed genome. M13 filaments from 50 to 2000 nm in length have been observed depending on the scope of the genetic modification.[125,159,160] Gold-binding M13 i-forms displayed a tube-like structure with one closed, rounded tip of slightly varying curvature and one open, flat or flared end.

Additional micrographs of i-forms exhibiting this same characteristic geometry are shown in Figure 5-3. This i-form morphology is consistent with other low temperature M13 transformation studies.[28,157] In these reports, the flared end was identified as the location through which DNA is extruded during infection and site of the p3 minor coat protein. The average length of the gold-binding i-forms was 161 ± 33 nm (Figure 5-4). This represents a 5.7-fold decrease in length compared to the filamentous form. The average gold-binding i-form length is significantly less than the 250 nm length measured for the wild-type i-form.[161] This difference may be a simple function of transformation conditions. Alternatively, it could be associated with differences in pVIII-pVIII interactions within gold-binding and wild-type phage attributable to the peptide fusion. Additional investigation is necessary to discern the source of disparity. Using electron microscopy, gold-binding s-forms appeared as round, but slightly deflated spheroids with an average diameter of approximately 60 nm. This is consistent with our previous studies which described the room temperature transformation of the gold-binding phage in detail.[156]

Despite these substantial morphological changes, i-forms and s-forms retain a complete set of pIII minor coat proteins with preserved affinity for anti-pIII antibodies[28]. Additionally, the general orientation of the filamentous protein capsid is maintained. The pIII is located near the fluted end of the i-form [28] and near the site of DNA release during s-form generation.[23] While the pIII protein may undergo a structural change during transformation, the *E. coli* binding only requires the N2 to be available.[149,162] Notwithstanding these persistent characteristics, the effect of transformation on minor

coat protein functions such as N2 domain F-pili adsorption is unknown, therefore the interaction of gold-binding M13 i-forms and s-forms with *E. coli* F-pili was evaluated. As such, a 25,000-fold excess of chloroform-treated phage templates was incubated with ER2738 to facilitate formation of phage-bacteria complexes. Figure 5-5 (a) and (b) portray transformed viral templates adsorbed to the tip of F-pili which appear as a hair-like appendages on the surface of the bacteria cell. Here, the F-pili structures were a few hundred nanometers in length, however F-pili as long as 20 μm have been measured.[163] Because the F-pili constantly retract and extend as new pili are produced, their length is highly variable.[164,165] Yet, upon infection via pIII N2 domain adsorption, the F-pili of the filamentous form of the M13 bacteriophage withdraw into the *E. coli* cell[164]. The observed shorter lengths may be attributable to F-pili retraction due to i-form and s-form binding. The attachment location of transformed phage supports direct interaction with the pIII, as opposed to another site on the capsid. Adsorption occurs at the flared end of the i-form and adjacent the opening associated with DNA extrusion in the s-form capsid[23]. While the F-pili adsorption has been confirmed for both the i-forms and the s-forms, the binding effect of nanoparticles on the templates has yet to be determined.

Transformed M13 bacteriophage were decorated with gold nanoparticles to serve as this photothermal antibacterial agents. Viral-templated gold nanostructures are shown in Figure 5-6 along with several unbound nanoparticles. Colloidal gold nanoparticles were bound to i-forms and s-forms in a disorganized, but tightly-packed arrangement which replicated the morphology of the underlying scaffold. Depending on size and shape, 10s to 100s of particles were visible on the transformed phage surface, yielding a

fusion peptide:nanoparticle ratio significantly larger than 1:1. Likely due to increased surface area, approximately twice as many gold nanoparticles were bound to i-forms as s-forms. Notably, gold-binding peptide affinity was independent of nanoparticle shape. As demonstrated in Figure 5-7, both the gold-binding i-form and s-form were able to template highly anisotropic particles, as readily as isotropic ones. The optical absorbance of Au colloid, Au/i-forms, and Au/s-forms is shown in Figure 5-8. The peak visible absorbance of 5 nm Au nanoparticles in tris-buffered saline at the concentration of 2.5×10^{10} particles/μL was 522 nm. The localized surface plasmon resonances (LSPRs) of Au/i-forms and Au/s-forms were redshifted 26 and 28 nm, respectively, compared to colloidal gold with notable peak broadening. The shift and broadening can be attributed to the coupling of Au NPs plasmon resonance modes.[166,167] The Au NPs assembled on the surface of the templates are in close contact to each other causing formation of the clusters. This results in electronic coupling of the particles and dipole-dipole interactions. As a result, the peak visible absorbance is a composition of both coupled plasmons from the clusters and unbound individual Au NPs from the solution.[168,169] The LSPR wavelengths of Au/i-form and Au/s-form nanostructures were well-suited for photothermal activation of bactericidal properties with 532 nm laser irradiation.

The high density of gold colloid on the capsid surface necessitated additional investigation to confirm infection via pIII adsorption was not inhibited. Viral-templated gold bactericidal nanostructures were gently mixed with a culture of *E. coli* in LB broth. Au/i-forms and Au/s-forms complexed with tip of an F-pilus or adjacent to the cell surface are depicted in Figure 5-9. Au/i-forms experienced considerable agglomeration, binding

to F-pili as aggregates of several i-forms rather than as individual nanostructures. As such, some i-form aggregates had multiple F-pili attachment points. The rather loose clusters of Au/i-forms, several hundred nanometers in size, appeared to be transported to the cell surface by F-pili retraction. As shown in Figure 5-10, the proximity of the Au/i-forms to the *E. coli* was highly variable. Some agglomerates were in intimate contact with the cell surface, while others were in an extended conformation with only a small point of contact and the bulk of the Au/i-form cluster far from the surface. In addition, several *E. coli* were observed without Au/i-forms nearby. In contrast to Au/i-forms, Au/s-forms were not particularly prone to agglomeration (Figure 5-11). Au/s-forms existed primarily as individual viral-templated gold nanostructures, or in small clusters of two or three. Drawn to the E. coli surface by F-pili, Au/s-forms were typically in close contact with the cell. In addition, more than one Au/s-form was occasionally found per cell. Irrespective of Au nanoparticle decoration, phage-bacteria complexes were created via interaction between pIII and F-pili. The results show that the gold nanoparticles on the templates do not interfere with the f-pili binding, even when the agglomerated clusters are formed.

The effectiveness of Au/i-forms and Au/s-forms as photothermal antibacterial agents was assessed using 532 nm laser illumination. The two viral-templated gold nanostructures were incubated with *E. coli* in the dark for 90 min, then irradiated with coherent light for a range of times and laser powers. As shown in Figure 5-12, dose-dependent cell viability was used to quantify photothermal bactericidal effects. While viability remained high (> 90%) for *E. coli* incubated with 5 nm gold colloid, after 20 min of 60 mW illumination over a spot size of 0.20 cm^2 (300 mW cm^{-2}), the viability of cultures

treated with Au/i-forms and Au/s-forms was 79 ± 4% and 36 ± 5%, respectively. The killing mechanism behind the Au/templates may be attributed to the heating of the nanoparticles, causing thermal damage to the *E. coli* membrane by protein denaturation and cell membrane disruption.[170] Furthermore, the closely packed gold nanoparticles on the templates form nanoparticle clusters on *E. coli* membrane. . Gold nanoparticles clusters have been shown both experimentally and theoretically to produce higher temperatures than their single particle counterparts.[171] The close proximity of the gold nanoparticles enhances the heating effect by the accumulative effect and the Coulomb interaction, where the former is attributed to the sum of individual nanoparticle heat fluxes and the latter is associated with plasmon enhanced electric fields.[172,173] There have also been reports on the photothermal formation of bubbles around the gold nanoparticles as part of the bactericidal process where the bubble irreparably damages the cell membrane[74,174] and the gold clusters enhancing said formation by decreasing the power threshold required to create these bubbles.[175] However, it is unlikely that it is bactericidal mechanism as the bubble formation require the use of short pulse lasers.[170] Considering that the i-forms had fewer gold nanoparticles on the surface of the bacteria, the plasmonic response was weaker, when compared with the spheroids. Hence, the photothermal effect is not as pronounced as on the s-form.

In the case of the Au/spheroids, an almost linear decrease in the *E. coli* survivability occurs within the first 10 minutes, going from 100% to 44.5±2.2%. However, beyond 10 minutes, the killing rate has diminishing returns, going from 44.5±2.2% to 36.1±4.9%. This drastic difference in killing rate is attributed to the way the templates are bound to the *E.*

coli. Figure 5-11 (c) shows that spheroidal templates are bound on the surface of the *E. coli*, bringing in more than 50 nanoparticles in close proximity to each other and are in direct contact with the membrane. In contrast, Figure 5-11 (d) shows that for the i-forms only a fraction of the entire structure is in contact with *E.* coli. It was previously shown that once Au/i-forms were incubated with *E. coli*, agglomerates formed and this resulted in fewer number of templates binding to the bacteria. This potentially decreases the efficacy of the system, as the number of bacteria was shown to have no Au/i-form bound to them. Additionally, the i-form only has a fraction of the gold nanoparticles in direct contact with the bacterial surface. While the i-form is significantly shorter than the filamentous phage, the overall structure of the template places the pIII protein at the tip of an elongated structure. This in turn only allows for a smaller number of nanoparticles to remain in contact with the *E. coli* membrane. This further accentuated by the structure of the agglomeration of the i-forms.

Figure 5-12 (b) shows the effect of power over a period of 20 min on the bactericidal rate of the templates. Again, the bare gold nanoparticles showed no bactericidal properties across all the powers. From 0 to 40 mW, the Au/spheroids showed steep decline in survivability the stronger the power, with 40.6±10.1% left alive. Beyond 40 mW, the % *E. coli* viability doesn't change much. The Au/i-forms on the other hand showed no distinct killing between 0 and 20 mW with 95% of *E. coli* remaining viable. The killing rate increases significantly at 40 mW achieving a 20% kill rate after 20 min. Similarly, to the Au/spheroids, the difference in killing rate between 40 and 60 mW is marginal. The assessment of the bactericidal properties of the templates and the gold/templates was

performed without laser irradiation. Figure S4 shows that in all cases, little to no bactericidal was observed (>90% viability). In terms of killing power of the Au/templates, with a kill rate of 63.9%, the Au/s-forms have achieved comparable results with the literature, density of 300 mW cm^{-2} over a period of 20 min. In those cases, in order to attain a similar kill rate, the laser power range needed was from 120 mW cm^{-2} to 2W cm^{-2} with an irradiation time ranging from 10 to 60 min[78–81,83,176]. Furthermore, to accomplish kill rates of more than 90%, the addition of antibiotics, silver and sensitizers were needed to achieve these kill rates and beyond [78–81,83,176]. In a study using both the antibiotic kanamycin and gold nanorods, a power of 120 mW cm^{-2} over a period of 20 min achieved an *E. coli* killing rate of 50%[80]. A different study using iron/gold core-shells succeeded at killing 40% of *MDRB Salmonella* and 0% in conjunction with methylene-blue sensitizer using a 2 W cm^{-2} laser over 12 min[83]. Another study using gold nanorod and silver showed a killing rate of above 50% without silver and 92% with silver at 150 mW over 1 mm spot size over 10 min[81]. This study has shown that in terms of killing power, the Au/templates can compete with antibody-based gold nanostructures.

5.4 Conclusion

In conclusion, we have studied the i-form transformation and its gold binding properties of a gold-binding M13 bacteriophage, the F-pili binding capabilities of both the i-form and the spheroids with and without gold, the photothermal bactericidal properties of Au/templates. This study looked into using transformed M13 bacteriophage as a platform for carrying and targeting photothermal bactericidal materials to *E. coli* as an alternative to antibodies. The study also showed that the F-pili binding was still

effective in both transformed form of the phage. This affinity to the F-pili was also shown to extend to the spheroidal form of the M13 bacteriophage.

Like its spheroidal counterpart, the i-forms was shown to retain its gold binding affinity. It was, however, found that the i-forms had a greater tendency to aggregate compared to the s-forms. More studies would be needed to further understand the aggregation phenomena. The N2 of the pIII of the gold decorated templates extended far enough to be available for F-pili binding. The F-pili was able to retract and bring the templates to the bacterial membrane. Unlike the s-forms, the i-forms, due to its geometry and the aggregation, were unable to maximize the high number of gold nanoparticles adjacent to the cell membrane.

As a photothermal bactericide, the Au/s-forms was able to attain a kill rate of 63.9% while its i-form counterparts only achieved a kill rate of 20.6% using a 532 nm laser. This low kill rate could be attributed to a combination of a lower count of available templates per *E. coli* due to the heavy i-form aggregation and to the lower number of gold nanoparticles in contact with the membrane. The Au/s-forms performance was comparable to other similar gold/antibodies targeting agents and the lack of additional bactericidal components such as silver or antibiotics. We have shown that the transformed phage can potentially be used as an alternative to antibodies to deliver photothermal bactericidal materials to *E. coli*. This, however, does not have to be limited to *E. coli* or to the visible spectrum. The versatility of the templates in binding a range of nanoparticle shapes was shown, enabling future tuning of the photothermal absorption wavelengths, potentially extending the platform for near infrared applications. The

templates could be further modify to target a variety of bacteria and could template materials of different shapes and composition to further enhance its photothermal killing rate.

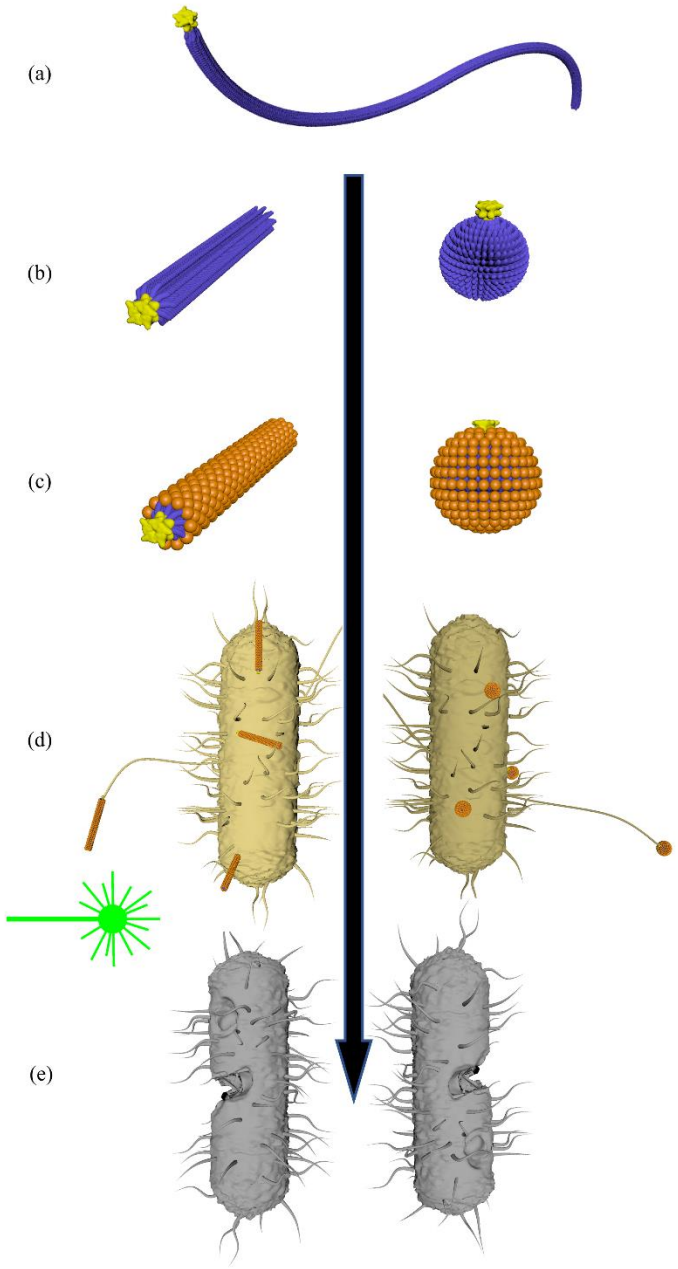

Figure 5- 1. Schematic illustration showing the following: (a) the filamentous phage, (b) The transformed phage (i-forms and s-forms), (c) The addition of Au nanoparticles to the templates, (d) Targeting of Au/template to *E. coli* and (e) Destruction of bacteria via laser

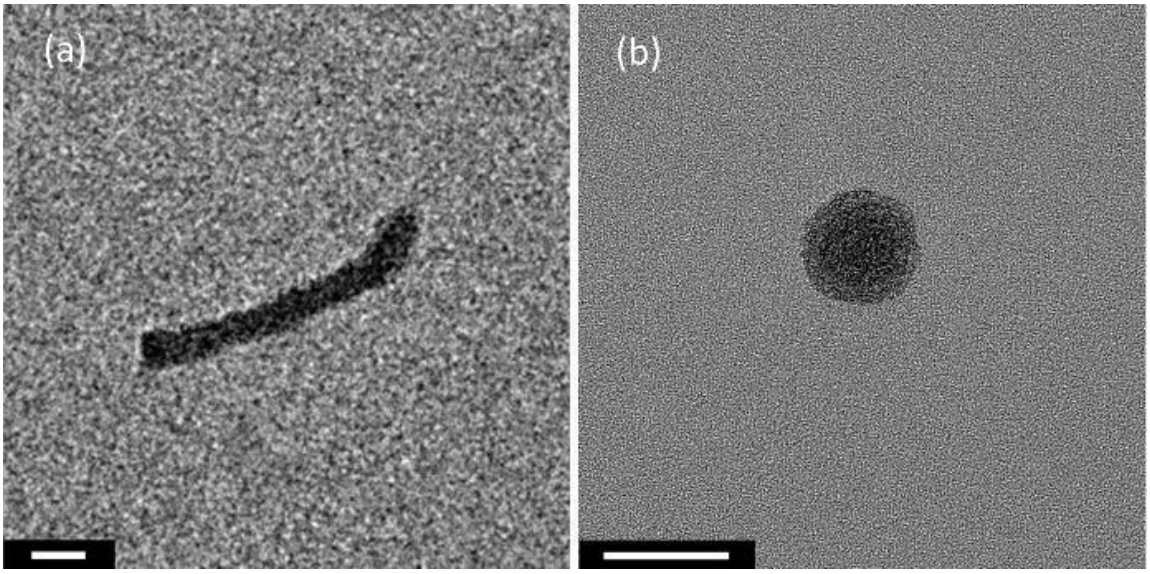

Figure 5- 2. TEM images of individual Au-binding M13 bacteriophage (a) filament (scale bar: 100 nm), (b) i-form (scale bar: 40 nm), and (c) spheroid (scale bar: 20 nm)

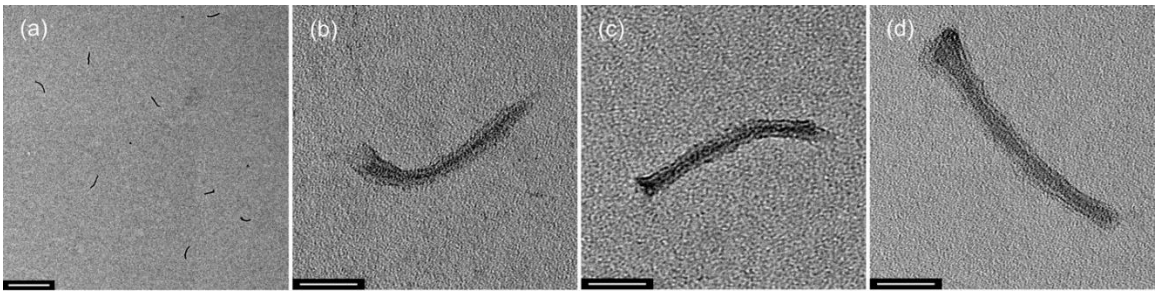

Figure 5- 3. Representative micrographs of i-forms at (a) low magnification and (b-d) high-magnification. Scale bar: (a) 500 nm, (b-d) 50 nm.

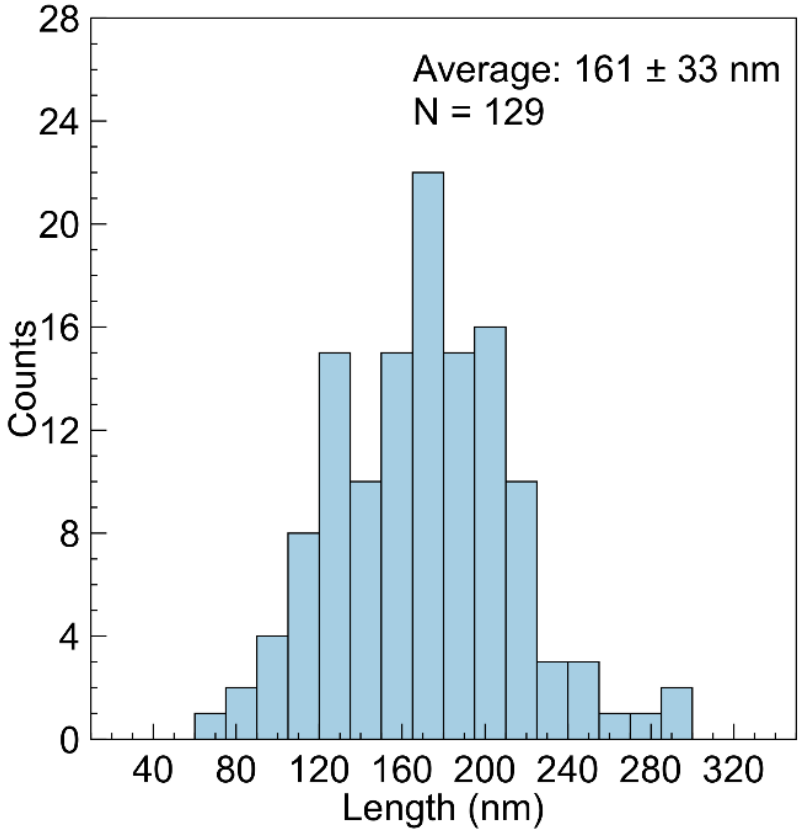

Figure 5- 4. Size distribution of i-forms

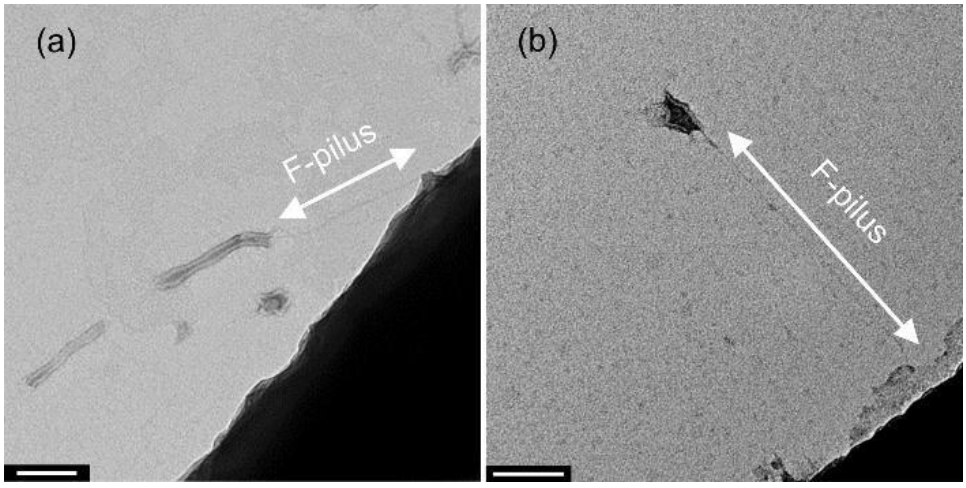

Figure 5- 5. (a) s-forms and (b) i-forms bound to *E. coli* demonstrating the availability of the pIII post transformation

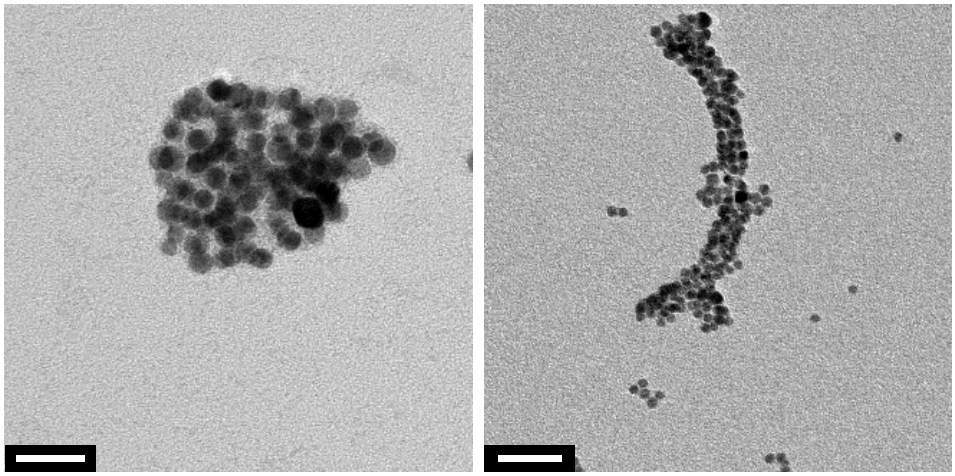

Figure 5- 6. Transmission electron microscope (TEM) image of (a) s-form and (b) i-form decorated with Au nanoparticles. Scale bar: 20 nm.

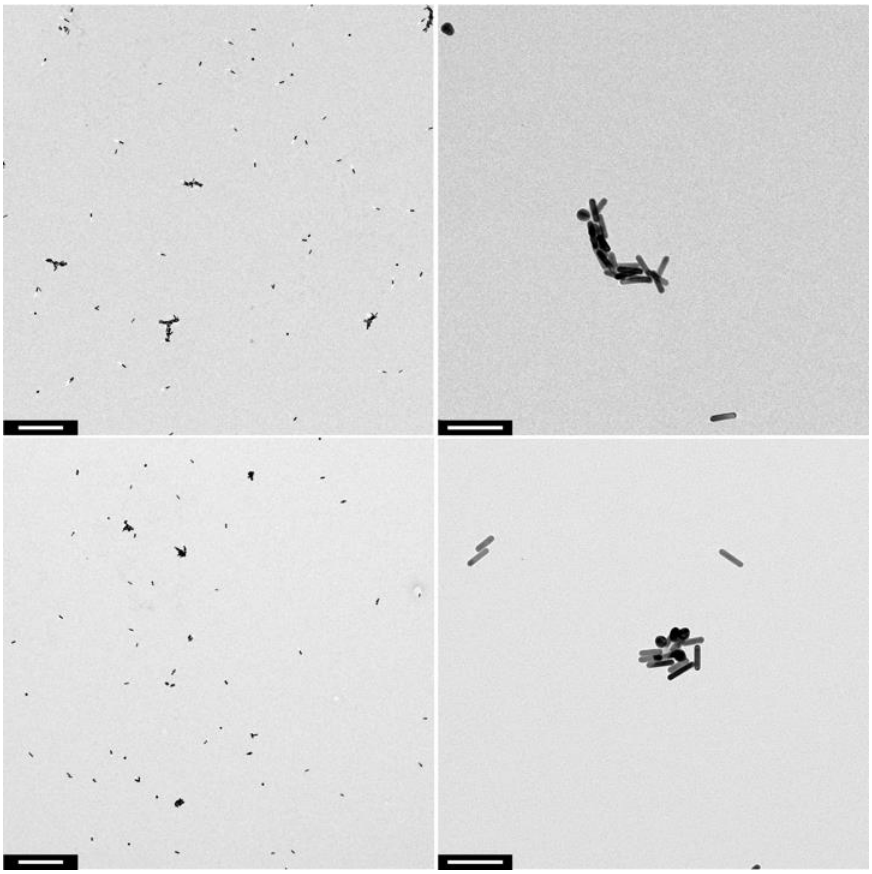

Figure 5- 7. Binding of Au nanorods (NRs) to (a, b) i-form and (c, d) s-form templates. Au NRs were 50 nm long and 8 nm in diameter, and were mixed at a ratio of 16:1 NRs:template. Scale bar: (a, c) 500 nm and (b, d) 100 nm.

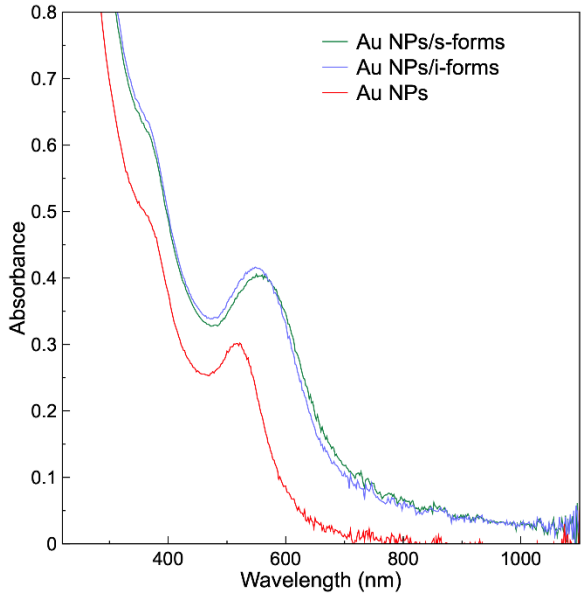

Figure 5- 8. UV-Vis absorbance spectra of Au nanoparticles assembled on Au-binding s-form and i-form M13 bacteriophage.

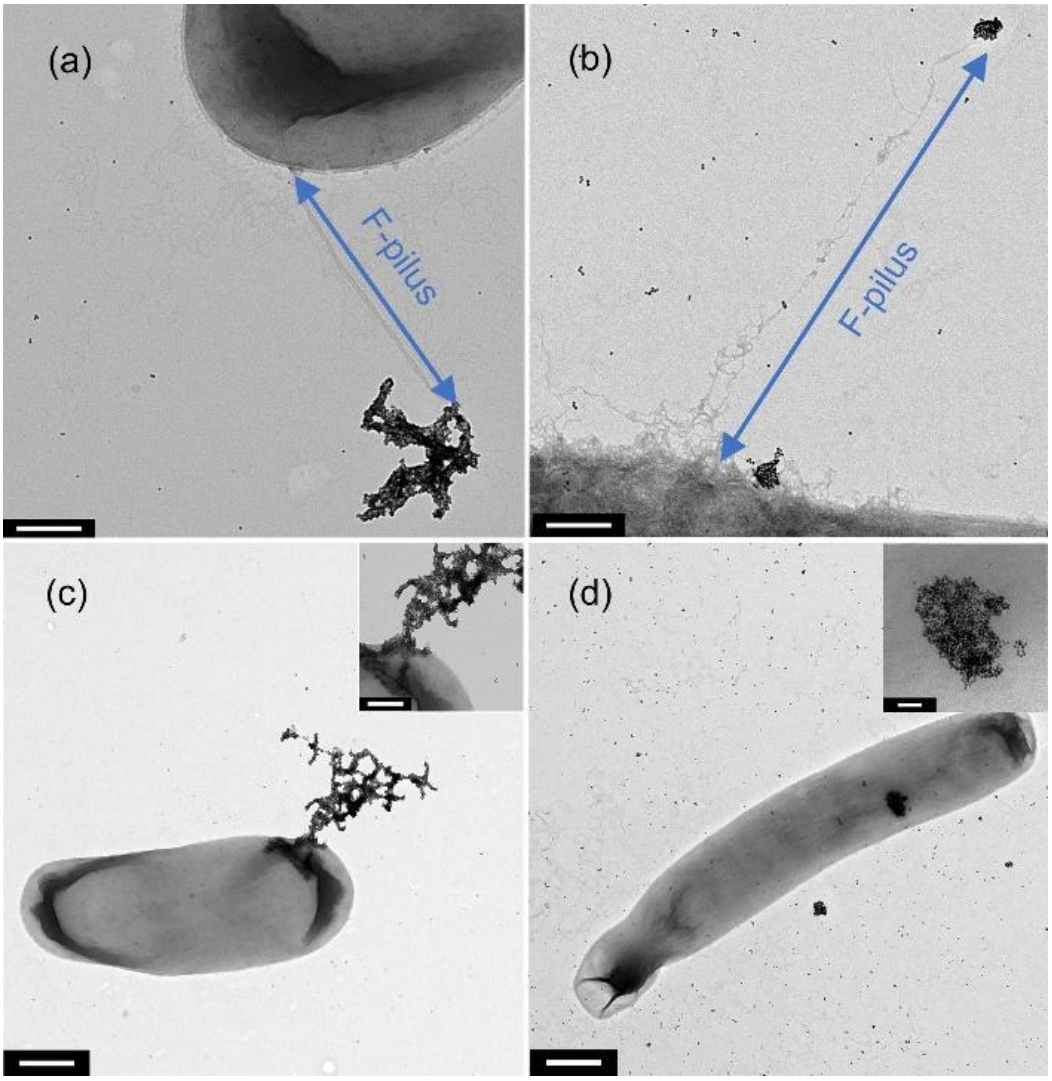

Figure 5- 9. Au/templates bound to F-pili displaying pIII availability post Au binding for (a) s-forms and (b) i-forms. (c) Au/i-forms and (d) Au/s-forms attached to the surface of *E. coli* demonstrating retraction of F-pili with Au/templates

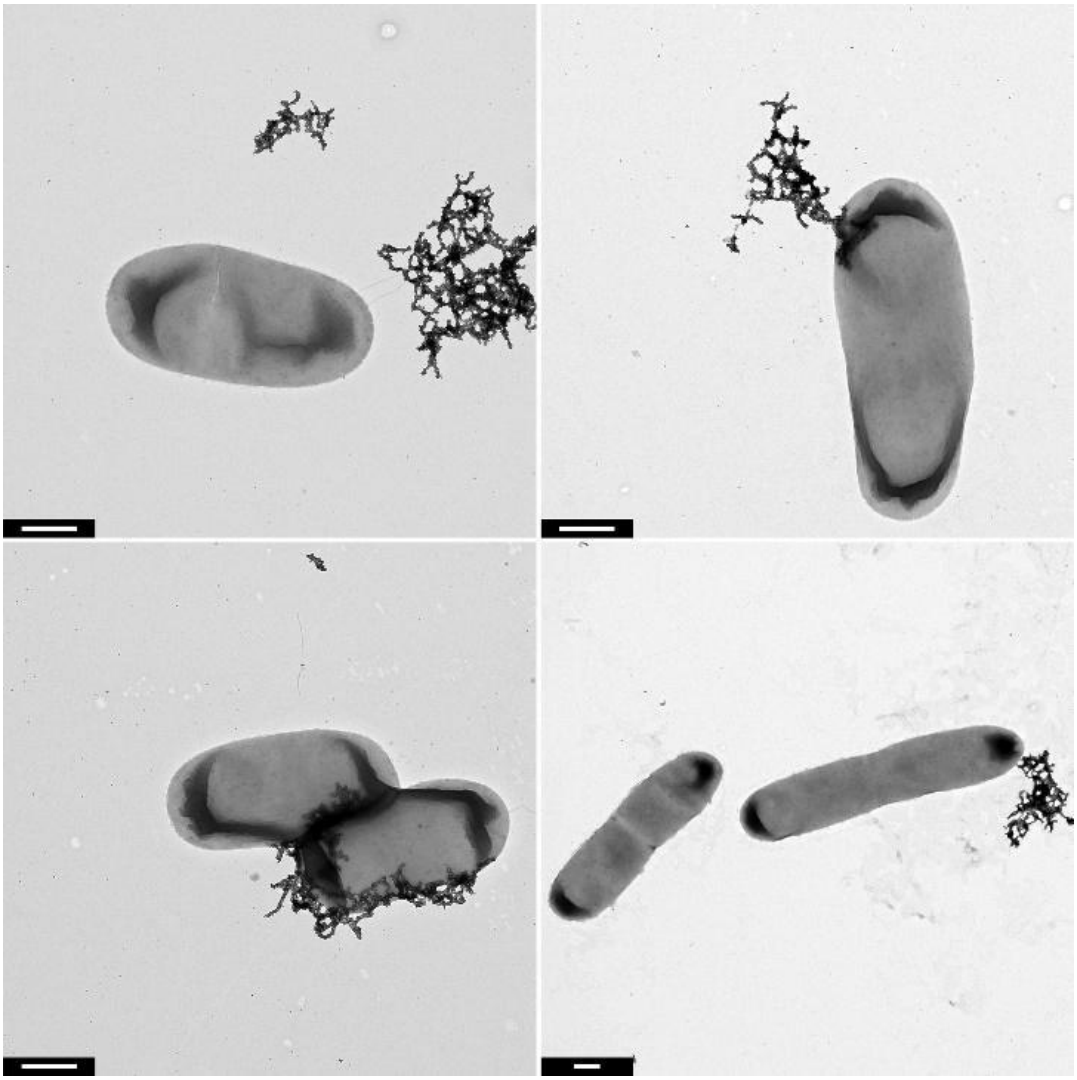

Figure 5- 10. TEM images of Au/i-forms bound to *E. coli* surface. Some *E. coli* were devoid of Au/i-forms. Scale bar: 500 nm.

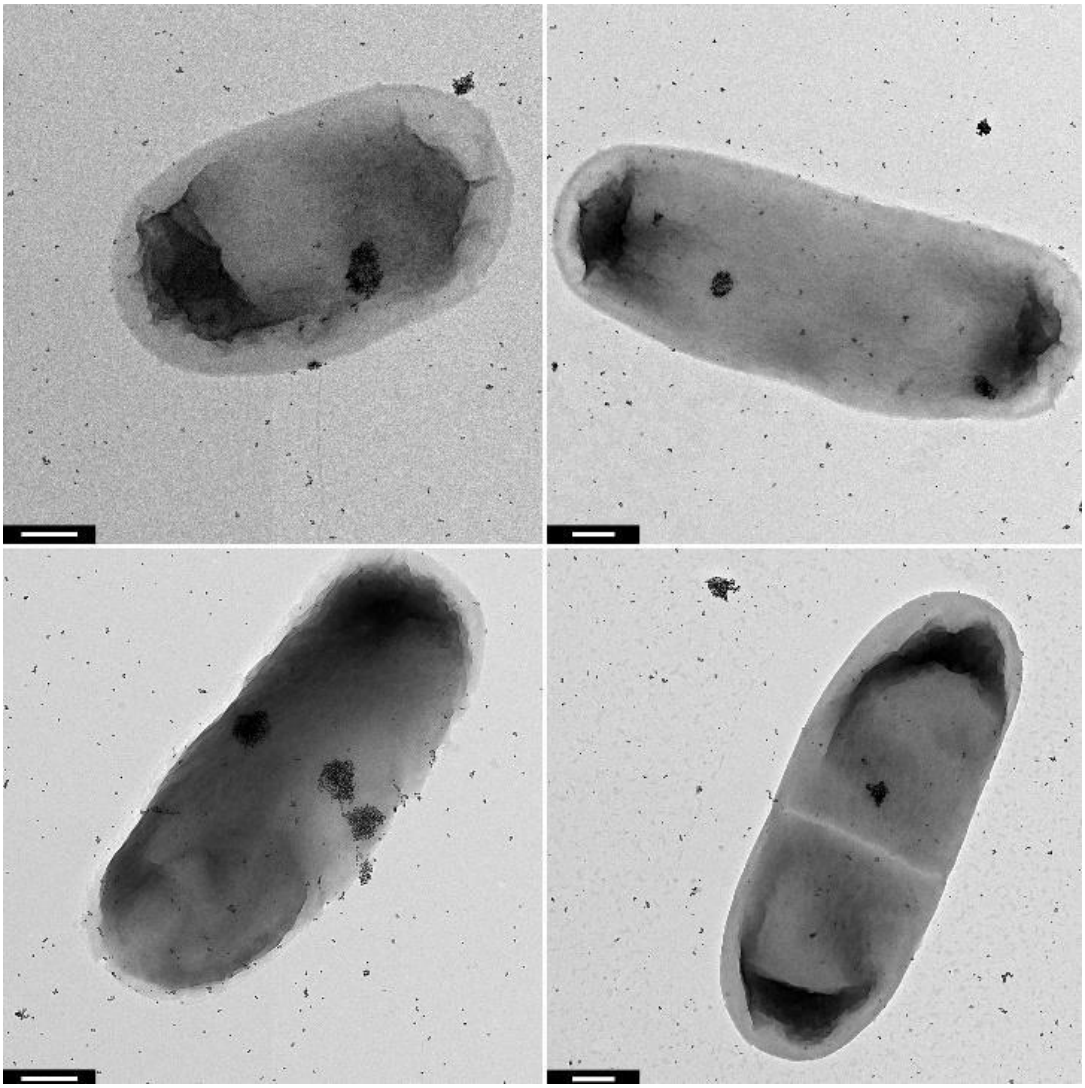

Figure 5- 11. TEM images of Au/s-forms bound to the *E. coli* surface. Scale bar: 200 nm.

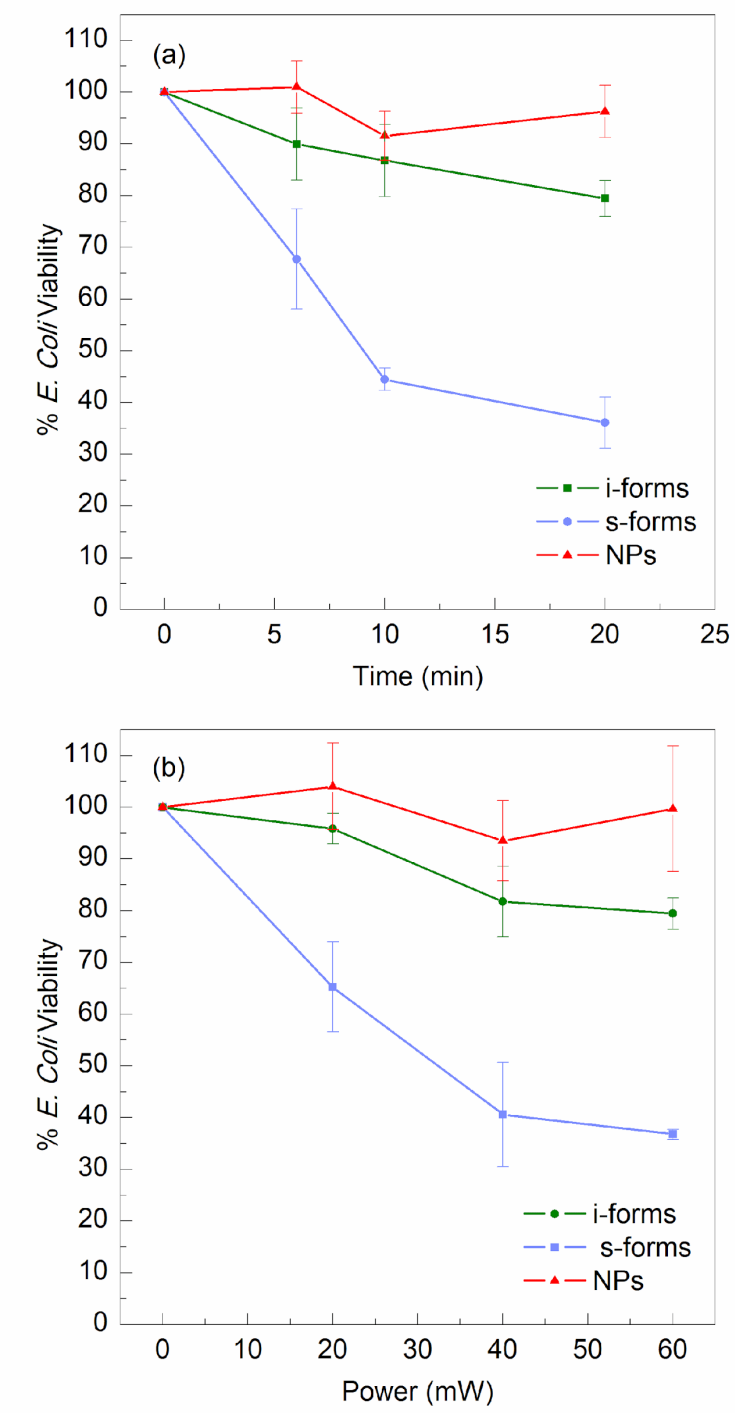

Figure 5- 12. (a) Time effect at 60 mW cm^{-2} and (b) power effect for 20 minutes of photothermal lysing using the bound Au NPs on s-forms and i-forms.

Chapter 6. Conclusion and Future Work

In this dissertation, we demonstrated biomineralization of two potential bactericidal materials, ZnO and gold on modified M13 bacteriophage, the transformation and optimization process of the filamentous form to spheroidal form of the M13 bacteriophage and a novel alternative to antibodies for targeting bacteria using the natural affinity of the M13 bacteriophage to *E. coli*. Biomineralization of ZnO on the M13 bacteriophage had mixed results. ZnO did appear to mineralize on the M13 bacteriophage, growing nanoparticles that were 41.1 ± 5.3 nm in diameter. These nanoparticles were randomly grown along the length of the filamentous phage and did not cover the entire length of the templates. Between the nanoparticles, a thin layer of materials were seen on the template. The elemental composition of the ZnO nanoparticles was confirmed by EDS. The lack of visible lattice from the TEM images and of the diffraction pattern or rings from electron diffraction indicated that the nanoparticles were amorphous. When compared to synthesis on the wild type, it was found that the length of phage was covered in a thin layer of material similar to the layer seen in the ZnO-binding phage. Unfortunately, this lack of crystallinity makes the ZnO/phage template unsuitable as a bactericidal agent.

The transformation and optimization process of the gold binding M13 bacteriophage into spheroids was demonstrated here. Early development process using agarose gel electrophoresis showed that low vortex time and rest time of 5s and 10s respectively over a total of 5 cycles were required to attain full conversion of the spheroids. The major limitation of using agarose gel electrophoresis was the minimum phage concentration required (5.67×10^9 pfu/µL), and hence the band, to be visible under UV illumination. While all the filamentous phage were converted into spheroids, these spheroids were more than twice as large as those found in the literature and had a broad size distribution. The spheroids created in this process were 96 ± 46 nm. Furthermore, significant aggregation of the spheroids were observed. Moving away from agarose gel electrophoresis, TEM became the primary tool for characterizing the spheroids.

Keeping with the vortex and rest time developed during the agarose gel electrophoresis, experiments with a lower concentration of 5×10^8 pfu/µL, power and sideways microcentrifuge orientation improved the spheroid stability, avoiding the formation of agglomerates and created smaller spheroids. This, however, was to the detriment to the conversion efficiency. To better understand the spheroidal transformation, two different design of experiments were conducted with size, % conversion and sub 100 nm spheroids as the outputs to be analyzed. The first looked into the effect of power and cycle number. Here, it was shown that the number of cycles had the greatest effect. Power had a lesser effect but nonetheless, the lowest power yielded the smallest spheroids. At 4 cycles and power 1, the size was found to be 81 ± 54 nm with 82% of spheroid being sub 100 nm and 79% of the spheroids converted. The

interaction of power and the number of cycles were found to be negligible. Based on these experiments, it was postulated that a higher number of cycles would have yielded most spheroids at the lowest power.

The second design of experiments looked into vortex time and concentration with the same outputs from the first design of experiments. Here we see that the spheroids were most affected by concentration except for the conversion yield. Vortex time, on the other hand, had a lesser effect on the outputs. However, it was still significant in its effect on the output. Again, the interaction between the two factors were comparatively negligible. Ultimately, the low vortex time and concentration yielded spheroids that were 53 ± 22 nm in diameter with 97% of spheroids smaller than 100 nm and 52% spheroids converted. As a result of the design of experiments, a power of 1, vortex time of 2 s/13 s and a concentration of 10^8 pfu/μL were chosen for further experiments.

To increase the yield, the effect of a number of cycles ranging from 1 to 16 cycles were studied with the aforementioned parameters. Through serendipity, it was found that a burst of vortex power at 10 for the first cycle followed by power 1 for all subsequent cycles narrowed the size distribution. Both TEM and circular dichroism was also used as a tool to analyze the effect of the number of cycles. Based on the results, 5 cycles was chosen as the optimal number of cycles. Spheroids transformed under these conditions were 59 ± 16 nm in diameter with 100% of the filaments converted.

It was demonstrated that the transformed phage was able to retain its affinity for premade gold nanoparticles and to biomineralize gold to form a spike gold nanostructure.

It was, furthermore, demonstrated that the synthesized gold morphology was highly dependent on the template geometry. Spheroids formed spiky structure alongside with fused gold nanoparticles of varying size while the filaments formed scattered gold nanoparticles along the length of the phage. This was the results of the higher gold ion density on the spheroids due to the higher surface packing of pVIII protein.

Au/transformed templates were shown to have photothermal bactericidal properties. It was found both i-forms and s-forms retained their affinity to the F-pilus of the targeted *E. coli*. Furthermore, the i-forms were also able to retain their gold binding properties, where the template was decorated with either gold nanoparticles or nanorods. However, the Au/i-forms were found to be more likely to form aggregates. When decorated with gold nanostructures, both templates still retained their F-pilus affinity and hence were able to target the bacterial host. The *E. coli*, by retracting the F-pilus, brought the Au/templates to the surface. However, the i-forms showed further aggregation and as such, alongside with its geometry, were unable to bring most of the gold nanoparticles to the bacterial surface. Photothermally, the spheroids showed a killing rate of 63.9% while the i-forms only achieved a kill rate of 20.6% using a 532 nm laser. The discrepancy in killing rate is due to the heavy aggregation and lower number of gold nanoparticles in contact with *E. coli*.

This dissertation has shown that the M13 bacteriophage has great promise to be a scaffold for bactericidal materials and targeting agent to bacteria. Since the virus can modified with affinities to different materials, the phage can be expended to bind and synthesize other bactericidal materials such as CuO or Fe_3O_4. The synthesis of crystalline

ZnO may be possible on the spheroids. The higher packing of peptides may results in the formation of crystalline material. However, due to the lengthy incubation process, further studies on the stability of spheroids over time should be looked into. Other experimental procedures could also help with the synthesis of crystalline ZnO.

In terms of gold synthesis, the stability over time of the gold/spheroids have not been studied. Agglomeration is a common occurrence with gold nanoparticles. In order for the gold nanostructures to be useful in applications such as photocatalysis and photothermal bactericide, the stability and dispersity of these structures is imperative. Using gold/templates as a photothermal bactericide can be further expanded upon. The addition of gold nanorods would allow for the Au/templates for the photothermal effect to be applied in the NIR, greatly expanding on the usability of the templates *in vivo* due to the deep tissue penetration of the NIR. The templates could also be used to target other bacterial organism or even cancer cells. The pIII could potentially be modified to target a variety of subjects.

References

1 P. V Baptista, M. P. McCusker, A. Carvalho, D. A. Ferreira, N. M. Mohan, M. Martins and A. R. Fernandes, *Front. Microbiol.*, 2018, **9**, 1441.

2 H. Nikaido, *Annu. Rev. Biochem.*, 2009, **78**, 119–46.

3 L. Wang, C. Hu and L. Shao, *Int. J. Nanomedicine*, 2017, **12**, 1227–1249.

4 J. T. Seil and T. J. Webster, *Int. J. Nanomedicine*, 2012, **7**, 2767–81.

5 Z. Golkar, O. Bagasra and D. G. Pace, *J. Infect. Dev. Ctries.*, 2014, **8**, 129–136.

6 R. Guntupalli, I. Sorokulova, E. Olsen, L. Globa, O. Pustovyy and V. Vodyanoy, *J. Vis. Exp*, 2013, 50474.

7 C. F. Barbas, D. R. Burton, J. K. Scott and G. J. Silverman, *Phage Display: A Laboratory Manual*, CSHL Press, 2004.

8 M. B. Dickerson, K. H. Sandhage and R. R. Naik, *Chem. Rev.*, 2008, **108**, 4935–4978.

9 C. Tamerler, D. Khatayevich, M. Gungormus, T. Kacar, E. E. Oren, M. Hnilova and M. Sarikaya, *Biopolymers*, 2010, **94**, 78–94.

10 C. Mao, D. J. Solis, B. D. Reiss, S. T. Kottmann, R. Y. Sweeney, A. Hayhurst, G. Georgiou, B. Iverson and A. M. Belcher, *Science*, 2004, **303**, 213–217.

11 S. W. Lee, C. Mao, C. E. Flynn and A. M. Belcher, *Science*, 2002, **296**, 892–895.

12 C. E. Flynn, C. Mao, A. Hayhurst, J. L. Williams, G. Georgiou, B. Iverson and A. M. Belcher, *J. Mater. Chem.*, 2003, **13**, 2414–2421.

13 S. H. Yang, W.-J. Chung, S. McFarland and S.-W. Lee, *Chem. Rec.*, 2013, **13**, 43–59.

14 C. W. Gray, R. S. Brown and D. A. Marvin, *J. Mol. Biol.*, 1981, **146**, 621–627.

15 L.-W. Deng and R. N. Perham, *J. Mol. Biol.*, 2002, **319**, 603–614.

16 J. Lubkowski, F. Hennecke, A. Plückthun and A. Wlodawer, *Structure*, 1999, **7**, 711–22.

17 R. Zandi and D. Reguera, *Phys. Rev. E- Stat. Nonlinear, Soft Matter Phys.*, 2005, **72**, 21917.

18 J. Atabekov, N. Nikitin, M. Arkhipenko, S. Chirkov and O. Karpova, *J. Gen. Virol.*, 2011, **92**, 453–456.

19 M. A. Bruckman, S. Hern, K. Jiang, C. A. Flask, X. Yu and N. F. Steinmetz, *J. Mater. Chem. B*, 2013, **1**, 1482–1490.

20 N. Nikitin, A. Ksenofontov, E. Trifonova, M. Arkhipenko, E. Petrova, O. Kondakova, M. Kirpichnikov, J. Atabekov, E. Dobrov and O. Karpova, *FEBS Lett.*, 2016, **590**, 1543–1551.

21 M. A. Bruckman, L. N. Randolph, A. VanMeter, S. Hern, A. J. Shoffstall, R. E. Taurog and N. F. Steinmetz, *Virology*, 2014, **449**, 163–173.

22 M. A. Bruckman, A. VanMeter and N. F. Steinmetz, *ACS Biomater. Sci. Eng.*, 2015, **1**, 13–18.

23 J. Griffith, M. Manning and K. Dunn, *Cell*, 1981, **23**, 747–753.

24 M. Manning, S. Chrysogelos and J. Griffith, *J. Virol.*, 1981, **40**, 912–919.

25 A. K. Dunker, L. D. Ensign, G. E. Arnold and L. M. Roberts, *FEBS Lett.*, 1991, **292**, 271–274.

26 L. M. Roberts and A. K. Dunker, *Biochemistry*, 1993, **32**, 10479–10488.

27 D. Stopar, R. B. Spruijt, C. J. A. M. Wolfs and M. A. Hemminga, *Biochemistry*, 1998, **37**, 10181–10187.

28 J. Lopez and R. E. Webster, *J Virol*, 1982, **42**, 1099–1107.

29 S. Sotiropoulou, Y. Sierra-Sastre, S. S. Mark and C. A. Batt, *Chem. Mater.*, 2008, **20**, 821–834.

30 F. Li and Q. Wang, *Small*, 2014, **10**, 230–245.

31 Z. Zhou, G. J. Bedwell, R. Li, N. Bao, P. E. Prevelige and A. Gupta, *Chem. Commun.*, 2015, **51**, 1062–1065.

32 A. Kadri, E. Maiß, N. Amsharov, A. M. Bittner, S. Balci, K. Kern, H. Jeske and C. Wege, *Virus Res.*, 2011, **157**, 35–46.

33 S. Balci, A. M. Bittner, K. Hahn, C. Scheu, M. Knez, A. Kadri, C. Wege, H. Jeske and K. Kern, *Electrochim. Acta*, 2006, **51**, 6251–6257.

34 D. Rothenstein, S. J. Facey, M. Ploss, P. Hans, M. Melcher, V. Srot, P. A. van Aken, B. Hauer and J. Bill, *Bioinspired Biomim. Nanobiomaterials*, 2013, **2**, 173–185.

35 Y. Li, B. Cao, M. Yang, Y. Zhu, J. Suh and C. Mao, *ACS Appl. Mater. Interfaces*, 2016, **8**, 30714–30721.

36 C. E. Flynn, S. W. Lee, B. R. Peelle and A. M. Belcher, *Acta Mater.*, 2003, **51**, 5867–5880.

37 K. M. Bromley, A. J. Patil, A. W. Perriman, G. Stubbs and S. Mann, *J. Mater. Chem.*, 2008, **18**, 4796–4801.

38 C. Jolley, M. Klem, R. Harrington, J. Parise and T. Douglas, *Nanoscale*, 2011, **3**, 1004–1007.

39 A. A. A. Aljabali, J. E. Barclay, G. P. Lomonossoff and D. J. Evans, *Nanoscale*, 2010, **2**, 2596–2600.

40 A. S. Blum, C. M. Soto, C. D. Wilson, J. D. Cole, M. Kim, B. Gnade, A. Chatterji, W. F. Ochoa, T. Lin, J. E. Johnson and B. R. Ratna, *Nano Lett.*, 2004, **4**, 867–870.

41 K. T. Nam, D.-W. Kim, P. J. Yoo, C.-Y. Chiang, N. Meethong, P. T. Hammond, Y.-M. Chiang and A. M. Belcher, *Science*, 2006, **312**, 885–888.

42 E. Royston, A. Ghosh, P. Kofinas, M. T. Harris and J. N. Culver, *Langmuir*, 2008, **24**, 906–912.

43 M. Gnerlich, E. Pomerantseva, K. Gregorczyk, D. Ketchum, G. Rubloff and R.

Ghodssi, *J. Micromechanics Microengineering*, 2013, **23**, 114014.

44 C. H. Moon, M. Zhang, N. V Myung and E. D. Haberer, *Nanotechnology*, 2014, **25**, 135205.

45 L. Chen, Y. Wu, Y. Lin and Q. Wang, *Chem. Commun.*, 2015, **51**, 10190–10193.

46 B. Schwarz and T. Douglas, *Wiley Interdiscip. Rev. Nanomedicine Nanobiotechnology*, 2015, **7**, 722–735.

47 S. L. Capehart, M. P. Coyle, J. E. Glasgow and M. B. Francis, *J. Am. Chem. Soc.*, 2013, **135**, 3011–3016.

48 P.-Y. Chen, R. Ladewski, R. Miller, X. Dang, J. Qi, F. Liau, A. M. Belcher and P. T. Hammond, *J. Mater. Chem. A*, 2013, **1**, 2217–2224.

49 R. A. Blaik, E. Lan, Y. Huang and B. Dunn, *ACS Nano*, 2016, **10**, 324–332.

50 H. E. Lee, H. K. Lee, H. Chang, H. Y. Ahn, N. Erdene, H. Y. Lee, Y. S. Lee, D. H. Jeong, J. Chung and K. T. Nam, *Small*, 2014, **10**, 3007–3011.

51 L. I. Vera-Robles, G. Van Tran Nhieu, C. Laberty-Robert, J. Livage and C. Sanchez, *Adv. Eng. Mater.*, 2013, **15**, 954–961.

52 D. Montalvan-Sorrosa, J. L. González-Solis, J. Mas-Oliva and R. Castillo, *RSC Adv.*, 2014, **4**, 57329–57336.

53 Y. Huang, C. Y. Chiang, S. K. Lee, Y. Gao, E. L. Hu, J. De Yoreo and A. M. Belcher, *Nano Lett.*, 2005, **5**, 1429–1434.

54 N. Korkmaz, *Colloids Surfaces B Biointerfaces*, 2013, **112**, 219–228.

55 M. S. Zaman, C. H. Moon, K. N. Bozhilov and E. D. Haberer, *Nanotechnology*, 2013, **24**, 325602.

56 K. Cung, B. J. Han, T. D. Nguyen, S. Mao, Y.-W. Yeh, S. Xu, R. R. Naik, G. Poirier, N. Yao, P. K. Purohit and M. C. McAlpine, *Nano Lett.*, 2013, **13**, 6197–6202.

57 K. N. Avery, J. E. Schaak and R. E. Schaak, *Chem. Mater.*, 2009, **21**, 2176–2178.

58 P. Y. Chen, X. Dang, M. T. Klug, J. Qi, N. M. Dorval Courchesne, F. J. Burpo, N. Fang, P. T. Hammond and A. M. Belcher, *ACS Nano*, 2013, **7**, 6563–6574.

59 C.-W. Chen, C.-Y. Hsu, S.-M. Lai, W.-J. Syu, T.-Y. Wang and P.-S. Lai, *Adv. Drug Deliv. Rev.*, 2014, **78**, 88–104.

60 J. R. Morones, J. L. Elechiguerra, A. Camacho, K. Holt, J. B. Kouri, J. T. Ramírez and M. J. Yacaman, *Nanotechnology*, 2005, **16**, 2346–2353.

61 W. Jiang, H. Mashayekhi and B. Xing, *Environ. Pollut.*, 2009, **157**, 1619–1625.

62 R. Vittal and K.-C. Ho, *Renew. Sustain. Energy Rev.*, 2017, **70**, 920–935.

63 Z. L. Wang, *Science (80-.).*, 2006, **312**, 242–246.

64 N. Padmavathy and R. Vijayaraghavan, *Sci. Technol. Adv. Mater.*, 2008, **9**, 35004.

65 V. Lakshmi Prasanna and R. Vijayaraghavan, *Langmuir*, 2015, **31**, 9155–9162.

66 I. Perelshtein, A. Lipovsky, N. Perkas, A. Gedanken, E. Moschini and P.

Mantecca, *Nano Res.*, 2015, **8**, 695–707.

67 † Prashant K. Jain, † Kyeong Seok Lee, *,‡ and Ivan H. El-Sayed and † Mostafa A. El-Sayed*, , DOI:10.1021/JP057170O.

68 M. A. Garcia, *J. Phys. D. Appl. Phys.*, 2011, **44**, 283001.

69 J. Pérez-Juste, I. Pastoriza-Santos, L. M. Liz-Marzán and P. Mulvaney, *Coord. Chem. Rev.*, 2005, **249**, 1870–1901.

70 S. Link and M. A. El-Sayed, *Int. Rev. Phys. Chem.*, 2000, **19**, 409–453.

71 B. G. Prevo, S. A. Esakoff, A. Mikhailovsky and J. A. Zasadzinski, *Small*, 2008, **4**, 1183–1195.

72 M. Gordel, J. Olesiak-Banska, R. Kolkowski, K. Matczyszyn, M. Buckle and M. Samoc, *J. Mater. Chem. C*, 2014, **2**, 7239.

73 R. Brayner, R. Ferrari-Iliou, N. Brivois, S. Djediat, M. F. Benedetti and F. Fiévet, *Nano Lett.*, 2006, **6**, 866–870.

74 † R. Sean Norman, ‡ John W. Stone, ‡ Anand Gole, ‡ and Catherine J. Murphy and † Tara L. Sabo-Attwood*, , DOI:10.1021/NL0727056.

75 M. Ramasamy, S. S. Lee, D. K. Yi and K. Kim, *J. Mater. Chem. B*, 2014, **2**, 981–988.

76 V. P. Zharov, K. E. Mercer, E. N. Galitovskaya and M. S. Smeltzer, *Biophys. J.*, 2006, **90**, 619–627.

77 N. J. Millenbaugh, J. B. Baskin, M. N. DeSilva, W. R. Elliott and R. D. Glickman, *Int. J. Nanomedicine*, 2015, **10**, 1953–1960.

78 Z. Fan, D. Senapati, S. A. Khan, A. K. Singh, A. Hamme, B. Yust, D. Sardar and P. C. Ray, *Chem. - A Eur. J.*, 2013, **19**, 2839–2847.

79 B. Khlebtsov, E. Tuchina, V. Tuchin and N. Khlebtsov, *RSC Adv.*, 2015, **5**, 61639–61649.

80 B. Hu, L. P. Zhang, X. W. Chen and J. H. Wang, *Nanoscale*, , DOI:10.1039/c2nr32457a.

81 K. C. L. Black, T. S. Sileika, J. Yi, R. Zhang, J. G. Rivera and P. B. Messersmith, *Small*, , DOI:10.1002/smll.201301283.

82 W.-C. Huang, P.-J. Tsai and Y.-C. Chen, *Small*, 2009, **5**, 51–56.

83 X. Dai, Z. Fan, Y. Lu and P. C. Ray, *ACS Appl. Mater. Interfaces*, 2013, **5**, 11348–11354.

84 V. J. B. Ruigrok, M. Levisson, M. H. M. Eppink, H. Smidt and J. van der Oost, *Biochem. J.*, 2011, **436**, 1–13.

85 A. Kolodziejczak-Radzimska and T. Jesionowski, *Materials (Basel).*, 2014, 7, 2833–2881.

86 P. K. Stoimenov, R. L. Klinger, G. L. Marchin and K. J. Klabunde, *Langmuir*, 2002, **18**, 6679–6686.

87 S. Nair, A. Sasidharan, V. V. Divya Rani, D. Menon, S. Nair, K. Manzoor and S. Raina, *J. Mater. Sci. Mater. Med.*, 2009, **20**, 235–241.

88 M. Fiedot, I. Maliszewska, O. Rac-Rumijowska, P. Suchorska-Woźniak, A. Lewińska and H. Teterycz, *Mater. (Basel, Switzerland)*, , DOI:10.3390/ma10040353.

89 A. Azam, A. S. Ahmed, M. Oves, M. S. Khan, S. S. Habib and A. Memic, *Int. J. Nanomedicine*, 2012, **7**, 6003–9.

90 K. Hirota, M. Sugimoto, M. Kato, K. Tsukagoshi, T. Tanigawa and H. Sugimoto, *Ceram. Int.*, 2010, **36**, 497–506.

91 K. Hirota, M. Sugimoto, M. Kato, K. Tsukagoshi, T. Tanigawa and H. Sugimoto, *Ceram. Int.*, 2010, **36**, 497–506.

92 N. Padmavathy and R. Vijayaraghavan, *Sci. Technol. Adv. Mater.*, 2008, **9**, 35004.

93 D. M. Blake, P.-C. Maness, Z. Huang, E. J. Wolfrum, J. Huang and W. A. Jacoby, *Sep. Purif. Methods*, 1999, **28**, 1–50.

94 A. Sirelkhatim, S. Mahmud, A. Seeni, N. H. M. Kaus, L. C. Ann, S. K. M. Bakhori, H. Hasan and D. Mohamad, *Nano-Micro Lett.*, 2015, **7**, 219–242.

95 M. M. Tomczak, M. K. Gupta, L. F. Drummy, S. M. Rozenzhak and R. R. Naik, *Acta Biomater.*, 2009, **5**, 876–882.

96 M. Umetsu, M. Mizuta, K. Tsumoto, S. Ohara, S. Takami, H. Watanabe, I. Kumagai and T. Adschiri, *Adv. Mater.*, 2005, **17**, 2571–2575.

97 M.-K. Liang, O. Deschaume, S. V. Patwardhan and C. C. Perry, *J. Mater. Chem.*, 2011, **21**, 80.

98 C. H. Moon and E. D. Haberer, *MRS Proc.*, 2012, **1461**, mrss12-1461-oo03-19.

99 C. H. Moon, M. Tousi, J. Cheeney, T.-T. Ngo-Duc, Z. Zuo, J. Liu and E. D. Haberer, *Appl. Phys. A Mater. Sci. Process.*, , DOI:10.1007/s00339-015-9475-7.

100 K. Zelechowska, J. Karczewska-Golec, J. Karczewski, M. Łoś, A. M. Kłonkowski, G. Węgrzyn and P. Golec, *Bioconjug. Chem.*, 2016, **27**, 1999–2006.

101 C. H. Moon, M. Tousi, J. Cheeney, T.-T. Ngo-Duc, Z. Zuo, J. Liu and E. D. Haberer, *Appl. Phys. A*, 2015, **121**, 757–763.

102 D. Rothenstein, B. Claasen, B. Omiecienski, P. Lammel and J. Bill, *J. Am. Chem. Soc.*, 2012, **134**, 12547–12556.

103 † Peter Gerstel, *,† Rudolf C. Hoffmann, † Peter Lipowsky, ‡ Lars P. H. Jeurgens, † and Joachim Bill and F. Aldinger†, , DOI:10.1021/CM051542O.

104 Q. Wu, X. Chen, P. Zhang, Y. Han, X. Chen, Y. Yan and S. Li, *Cryst. Growth Des.*, 2008, **8**, 3010–3018.

105 Z. Huang, X. Zheng, D. Yan, G. Yin, X. Liao, Y. Kang, Y. Yao, D. Huang and B. Hao, *Langmuir*, 2008, **24**, 4140–4144.

106 M. Manning, M. Moore, L. Spremulli and J. Griffith, *Biochem. Biophys. Res. Commun.*, 1983, **112**, 349–355.

107 L. M. Roberts and A. K. Dunker, *Biochemistry*, 1993, **32**, 10479–10488.

108 ‡ David Stopar, Ruud B. Spruijt, and Cor J. A. M. Wolfs and M. A. Hemminga*, , DOI:10.1021/BI9718144.

109 V. a Petrenko and G. P. Smith, *Protein Eng.*, 2000, **13**, 589–592.

110 E. V. Olsen, J. C. Sykora, I. B. Sorokulova, I.-H. Chen, W. C. Neely, J. M. Barbaree, V. A. Petrenko and V. J. Vodyanoy, *ECS Trans.*, 2007, **2**, 9–25.

111 B. Cao, H. Xu and C. Mao, *Microsc. Res. Tech.*, 2011, **74**, 627–635.

112 J. Z. Porterfield and A. Zlotnick, *Virology*, 2010, **407**, 281–288.

113 D. A. Marvin, R. D. Hale, C. Nave and M. H. Citterich, *J. Mol. Biol.*, 1994, **235**, 260–286.

114 D. Marvin, *Curr. Opin. Struct. Biol.*, 1998, 8, 150–158.

115 D. Stopar, R. B. Spruijt, C. J. A. M. Wolfs and M. A. Hemminga, *Biochim. Biophys. Acta - Biomembr.*, 2003, 1611, 5–15.

116 R. B. Spruijt, C. J. A. M. Wolfs and M. A. Hemminga, *Biochemistry*, 2004, **43**, 13972–13980.

117 K. A. Williams and C. M. Deber, *Biochemistry*, 1996, **35**, 10472–10483.

118 G. E. Arnold, L. a Day and a K. Dunker, *Biochemistry*, 1992, **31**, 7948–7956.

119 G. J. Hunter, D. H. Rowitch and R. N. Perham, *Nature*, 1987, **327**, 252–254.

120 H. Endemann and P. Model, *J. Mol. Biol.*, 1995, **250**, 496–506.

121 N. J. Greenfield, *Nat. Protoc.*, 2006, **1**, 2876–2890.

122 C. T. K. Yuen, A. R. Davidson and C. M. Deber, *Biochemistry*, 2000, **39**, 16155–16162.

123 D. Stopar, R. B. Spruijt, C. J. A. M. Wolfs and M. A. Hemminga, *Biochim. Biophys. Acta - Protein Struct. Mol. Enzymol.*, 2002, **1594**, 54–63.

124 J. Beaudoin, T. J. Henry and D. Pratt, *J. Virol.*, 1974, **13**, 470–477.

125 L. Specthrie, E. Bullitt, K. Horiuchi, P. Model, M. Russel and L. Makowski, *J. Mol. Biol.*, 1992, **228**, 720–724.

126 S. Sattar, N. J. Bennett, W. X. Wen, J. M. Guthrie, L. F. Blackwell, J. F. Conway and J. Rakonjac, *Front. Microbiol.*, 2015, **6**, 316.

127 V. a Petrenko and G. P. Smith, *Protein Eng.*, 2000, **13**, 589–92.

128 J. S. Lim, S. M. Kim, S. Y. Lee, E. A. Stach, J. N. Culver and M. T. Harris, *J. Colloid Interface Sci.*, 2010, **342**, 455–461.

129 Z. Reddad, C. Gerente, Y. Andres and P. Le Cloirec, *Environ. Sci. Technol.*, 2002, **36**, 2067–2073.

130 G. Limousin, J. P. Gaudet, L. Charlet, S. Szenknect, V. Barthès and M. Krimissa, *Appl. Geochemistry*, 2007, 22, 249–275.

131 M. R. Rasch, K. V. Sokolov and B. A. Korgel, *Langmuir*, 2009, **25**, 11777–11785.

132 E. Hao, S. Y. Li, R. C. Bailey, S. L. Zou, G. C. Schatz and J. T. Hupp, *J. Phys. Chem. B*, 2004, **108**, 1224–1229.

133 S. N. Abdollahi, M. Naderi and G. Amoabediny, *Colloids Surfaces A Physicochem. Eng. Asp.*, 2013, **436**, 1069–1075.

134 A. Albanese and W. C. W. Chan, *ACS Nano*, 2011, **5**, 5478–5489.

135 Y. Yang, S. Matsubara, M. Nogami, J. Shi and W. Huang, *Nanotechnology*, 2006, **17**, 2821–2827.

136 N. G. Khlebtsov, A. G. Melnikov, L. A. Dykman and V. A. Bogatyrev, in *Photopolarimetry in Remote Sensing*, eds. G. Videen, Y. Yatskiv and M. Mishchenko, Springer Netherlands, Dordrecht, 2005, pp. 265–308.

137 S. J. Barrow, A. M. Funston, D. E. Gómez, T. J. Davis and P. Mulvaney, *Nano Lett.*, 2011, **11**, 4180–4187.

138 A. A. Lazarides and G. C. Schatz, *J. Phys. Chem. B*, 2000, **104**, 460–467.

139 M. Shi, W. Su and H. Matsui, *Nanoscale*, 2010, **2**, 2373–2376.

140 I. A. Banerjee, L. Yu and H. Matsui, *Proc. Natl. Acad. Sci.*, 2003, **100**, 14678–14682.

141 L. Leon, W. Su, H. Matsui and R. Tu, *Soft Matter*, 2011, **7**, 10285–10290.

142 H. C. Neu, *Science (80-.).*, 1992, **257**, 1064–1073.

143 M. A. Fischbach and C. T. Walsh, *Science (80-.).*, 2009, **325**, 1089–1093.

144 S. B. Levy and M. Bonnie, *Nat. Med.*, 2004, **10**, S122–S129.

145 Y. Feng, L. Liu, J. Zhang, H. Aslan and M. Dong, *J. Mater. Chem. B*, 2017, **5**, 8631–8652.

146 L. M. Liz-Marzán, *Langmuir*, 2006, **22**, 32–41.

147 E. Boisselier and D. Astruc, *Chem. Soc. Rev.*, 2009, **38**, 1759–1782.

148 L. Mocan, C. Matea, F. A. Tabaran, O. Mosteanu, T. Pop, C. Puia, L. Agoston-Coldea, D. Gonciar, E. Kalman, G. Zaharie, C. Iancu and T. Mocan, *Sci. Rep.*, 2016, **6**, 1–9.

149 L.-W. Deng, P. Malik and R. N. Perham, *Infection*, 1999, **277**, 271–277.

150 P. Holliger and L. Riechmann, *Structure*, 1997, **5**, 265–275.

151 R. O'Callaghan, R. Bradley and W. Paranchych, *Virology*, , DOI:10.1016/0042-6822(73)90131-1.

152 P. M. Silverman and M. B. Clarke, *Integr. Biol.*, 2010, **2**, 25–31.

153 N. M. Bardhan, D. Ghosh and A. M. Belcher, *J Biophotonics*, 2014, **7**, 617–623.

154 T.-T. Ngo-Duc, J. M. Plank, G. Chen, R. E. S. Harrison, D. Morikis, H. Liu and E. D. Haberer, *Nanoscale*, 2018, **10**, 13055–13063.

155 T.-T. Ngo-Duc, J. M. Plank, G. Chen, R. E. S. Harrison, D. Morikis, H. Liu and E. D. Haberer, *Nanoscale*, , DOI:10.1039/c8nr03229g.

156 T.-T. Ngo-Duc, J. M. Plank, G. Chen, R. E. S. Harrison, D. Morikis, H. Liu and E.

D. Haberer, *Nanoscale*, 2018, **10**, 13055–13063.

157 M. Manning, S. Chrysogelos and J. Griffith, *J. Virol.*, 1981, **40**, 912–919.

158 G. J. Barbas, C.F., Burton, D.R., Scott, J. K., Silverman, *Phage Display: A Laboratory Manual*, CSHL Press, 2004.

159 J. Beaudoin ', T. J. Henry ' and D. Pratt3, *J. Virol.*, 1974, **13**, 470–477.

160 J. Rakonjac and N. J. Bennett, *Curr. Issues Mol. Biol.*, 2009, **13**, 51–76.

161 J. Griffith and M. Manning, *Arch. Biochem. Biophys.*, 1985, **236**, 297–303.

162 C. Krebber, S. Spada, D. Desplancq, A. Krebber, L. Ge, A. Plu and È. Ckthun, *Selectively-infective Phage (SIP): A Mechanistic Dissection of a Novel in vivo Selection for Protein-ligand Interactions*, .

163 L. C. Harringtont and A. C. Rogerson, *The F Pilus of Escherichia coli Appears To Support Stable DNA Transfer in the Absence of Wall-to-Wall Contact between Cells*, 1990, vol. 172.

164 A. Jacobson, *J. Virol.*, 1972, **10**, 835–43.

165 M. Clarke, L. Maddera, R. L. Harris and P. M. Silverman, *Proc. Natl. Acad. Sci.*, 2008, **105**, 17978–17981.

166 A. N. Shipway, M. Lahav, R. Gabai and I. Willner, *Langmuir*, 2000, **16**, 8789–8795.

167 S. K. Ghosh and T. Pal, *Chem. Rev.*, 2007, 107, 4797–4862.

168 K. S. Mayya, V. Patil and M. Sastry, *Langmuir*, 1997, **13**, 3944–3947.

169 G. C. Schatz, *J. Mol. Struct. THEOCHEM*, 2001, **573**, 73–80.

170 X. Huang, P. K. Jain, I. H. El-Sayed and M. A. El-Sayed, *Lasers Med. Sci.*, 2008, **23**, 217–228.

171 *,† Hugh H. Richardson, † Zackary N. Hickman, ‡ Alexander O. Govorov, † Alyssa C. Thomas, ‡ and Wei Zhang and M. E. Kordesch‡, , DOI:10.1021/NL060105L.

172 A. O. Govorov and H. H. Richardson, *Generating heat with metal nanoparticles*, 2007, vol. 2.

173 A. O. Govorov, A. W. Zhang, A. T. Skeini, A. H. Richardson, J. Lee, A. N. A. Kotov, A. O. Govorov, W. Zhang, A. E. Timur, S. Ae, H. Richardson, A. E. Jaebeom, L. Ae and N. A. Kotov, *Nanoscale Res Lett*, 2006, **1**, 84–90.

174 R. R. Letfullin, C. Joenathan, T. F. George and V. P. Zharov, *Nanomedicine*, 2006, **1**, 473–480.

175 D. Lapotko, *Nanomedicine (Lond).*, 2009, **4**, 813–45.

176 W.-C. Huang, P.-J. Tsai and Y.-C. Chen, *Small*, 2009, **5**, 51–56.